INSIGHTS INTO THE PROCESSES AND LIMITING FACTORS OF BEDROCK RIVER EROSION USING FLUME EXPERIMENTS, TOPOGRAPHIC ANALYSES, AND DAMAGE CONTINUUM CONCEPTS

A Dissertation

Presented in Partial Fulfillment of the Requirements for the

Degree of Doctor of Philosophy

with a

Major in Geological Sciences

in the

College of Graduate Studies

University of Idaho

by

Jeffrey E. Larimer

Co-Major Professor: Elowyn Yager, Ph.D.

Co-Major Professor: Brian Yanites, Ph.D.;

Committee Members: Timothy Bartholomaus, Ph.D.; S.J. Jung, Ph.D.; Jessica Stanley, Ph.D.

Department Administrator: Leslie Baker, Ph.D.

December 2019

AUTHORIZATION TO SUBMIT

This dissertation of Jeffrey E. Larimer, submitted for the degree of Doctor of Philosophy with a Major in Geological Sciences and titled "Insights into the Processes and Limiting Factors of Bedrock River Erosion Using Flume Experiments, Topographic Analyses, and Damage Continuum Concepts" has been reviewed in final form. Permission, as indicated by the signatures and dates below, is now granted to submit final copies to the College of Graduate Studies for approval.

Co-Major Professor: _____ Date: _____

Elowyn Yager, Ph.D.

Co-Major Professor: _____ Date: _____

Brian Yanites, Ph.D.

Committee Members: _____ Date: _____

Timothy Bartholomaus, Ph.D.

_____ Date: _____

S.J. Jung, Ph.D.

_____ Date: _____

Jessica Stanley, Ph.D.

Department

Administrator: _____ Date: _____

Leslie Baker, Ph.D.

ABSTRACT

Many important understandings of the dynamic coupling between climate tectonics and erosion are based on models of bedrock erosion. However, many questions concerning incision process and the bedrock resistance to incision remain unanswered. Mechanistic based models of erosion provide the best opportunity to model landscape evolution with the most nuanced approaches to consider the erosive energy of a stream and the properties of rock that govern the transfer of that energy into erosion. The purpose of this dissertation is to experimentally test specific mechanistic erosion equations and use fieldwork in bedrock channels of central Arizona to investigate the controls on resistance to erosion. In chapter two, flume experiments of sediment transport show that adding non-planar topography to the channel floor generates heavy tail distributions of impact energies and causes the energy delivered to the bed to shift from a decreasing to an increasing relation with the shear stress of the flow. In chapter three the morphology of lithologically variant bedrock channels in central Arizona shows strong correlations with resistance factors to processes of erosion and suggests that channel slope is sensitive to the resistance to abrasion and the size of sediment in the channel while channel width is sensitive to the bedrock joint spacing and the size of sediment in the channel. Chapter four uses fieldwork to investigate the accumulation of damage in channel surfaces through sub-aerial weathering processes and sediment impacts to show that mineralogy and crystalline grain size play an important role the evolution rock erodibility in a natural setting.

ACKNOWLEDGEMENTS

I would first like to acknowledge my advisor, Brian Yanites for his mentorship throughout my dissertation, providing immense amounts of critical feedback and time discussing all aspects of the scientific process with me, as well as facilitating all of the research that I have done throughout my time as an MS and PhD student. I would like to thank Elowyn Yager for her mentorship, especially that related to the experimental work within this dissertation and my time spent at the Center for Ecohydraulics Research facilities in Boise, Idaho. I would like to thank S.J. Jung for his mentorship and insightful discussions in all things related to rock mechanics as well as training me in the tools and techniques of testing mechanical properties of rock. I am grateful to my other committee members including Timothy Bartholomaus and Jessica Stanley for their guidance and critical feedback on all subjects within this dissertation. I am grateful to Bob Basham and Ralph Budwig at the Center Ecohydraulics Research in Boise, Idaho. I thank Alex Miller for his help with particle tracking within the flume experiments. I thank all who have aided in the extensive fieldwork in Arizona collecting drill core samples of rock and surveying river channels. This includes Brian Yanites, Nate Mitchell, Cody Parker, Hayley Rambur, Mike Larimer, and Margot Gildner. I have many academic colleagues to thank for long discussions regarding the work herein and moral support throughout the process. In chronological order I thank Clay Sorensen, Darin Schwartz, Alex Moody, Matt Pendelton, James Muirhead, Thomas Morrow, Brigid Lynch, Nate Mitchell, Zachary Foster-Barril, Cody Stevens, Phillip Greene, Clarke Delisle, and Sarah Schanz. This work has been conducted with financial support from the Army Research Laboratory under grant W911NF-17-1-0248.

DEDICATION

This is dedicated to my family and friends.

TABLE OF CONTENTS

LIST OF TABLES

LIST OF FIGURES

CHAPTER 1: INTRODUCTION

Landscapes evolve over long timescales in response tectonics forces that provide the potential energy for rivers and glaciers to erode the surface. Incision into bedrock by river erosion sets the lower boundary of a landscape and drives the gradient of local hillslopes. Correlations between topographic relief and erosion rate (Ahnert, 1970) suggest that landscape relief adjusts so that erosion rates attain equilibrium with tectonic uplift. It is now widely accepted that landscape relief is set by the longitudinal river profile (Whipple et al., 1999) of which rock strength plays an important role. Harder rock requires more erosive energy to erode at the rate of rock-uplift and thus river channels self-adjust their morphology (channel slope, channel width, and bed roughness) to provide the energy necessary to sustain dynamic equilibrium between uplift and erosion. However, understanding the links between the properties of rock that resist erosion and river morphology remains a key challenge in fluvial geomorphology and studies of landscape evolution. The separate studies within this dissertation attempt to unravel some of the complex relations between bedrock properties, erosion rate, and channel morphology.

While the morphology of a river channel is shown to change with rock type (Wohl and Merritt, 2001), functional relationships between rock properties and channel morphology remain unclear. Quantitative studies on erosion processes are made difficult partly due to the long timescales (10,000 yr to 1 Myr) over which channel morphology adjusts. The influence of rock type on channel morphology is also complicated by local variations in rock strength due to the anisotropic nature of rock and weathering history. It is also unclear which rock properties dictate the resistance to erosion when there are multiple erosion processes to consider. For example, the strength of the rock mass likely dictates the resistance to abrasion by sediment

impacts, but the spacing of fractures or joints along the bedrock surface likely dictates the resistance to entrainment of jointed blocks of bedrock. Furthermore, the influence of rock strength on channel morphology can be obscured by local variations in the size and rate of sediment supplied to a channel. Sediment provides the tools for bedrock abrasion, but too much sediment can cover the bed and armor it from erosion. The size of individual grains controls the resistance to motion, where a stationary grain protects the bed from erosion and a grain in motion becomes an agent of erosion. If the supply of sediment to a particular reach is greater than the capacity of the stream to transport sediment out of the reach then bed cover will occur. On the other hand if the stream is able to effectively transport material in excess of what is supplied then the bed is exposed to erosive processes. Due to the complex interactions between the processes described above, determining the relative importance of the processes that detach rock and the effects of sediment mobility on channel morphology remains a challenge. In chapter three, I use regression analyses to investigate the relative importance of detachment processes and sediment effects on the slope and width of bedrock channels in central Arizona.

Landscape evolution models often use topographic signatures to interpret the signals of climate and tectonic histories. While these types of models have proven to be useful (Kirby and Whipple, 2012) they are incomplete because they lack explicit considerations of rock properties and sediment transport. Instead, these models indirectly solve for the rock's resistance to erosion, but is based on timing constraints of river evolution and the choice of the specific erosion law (Stock and Montgomery, 1999; Kirby and Whipple, 2001). However, mechanistic based models of river erosion are able to apply the physical laws of sediment transport and the

resistance of rock to fracturing (Foley, 1980; Sklar and Dietrich, 2004; Chatanantavet and Parker, 2009). While mechanistic models provide a deeper understanding of the processes and limitations of river incision processes, challenges remain in quantifying how rock properties influence both the erosive energy of a stream as well as the erosive energy required to remove a unit volume of rock. For example, the roughness of the channel bed surface, which is strongly controlled by rock properties (Whipple et al., 2000; Richardson and Carling, 2005), should have an effect on both the velocity of flowing water and the sediment impact dynamics; and thus, the erosivity of the stream. While few studies have focused on the effects of bed topography on the erosive energy of sediment impacts, Huda and Small (2014) used a mechanistic model to show that the erosion rate could vary over four orders of magnitude due to the affect of bed topography on sediment impact trajectories. However, their model did not include a representation of how the interaction between flow and bed topography would affect sediment motions. In chapter two I use laboratory experiments of river sediment transport to investigate how sediment impact trajectories differ for planar and non-planar beds.

Previous efforts to consider the influence of rock type on bedrock incision have typically relied on laboratory rock strength tests (e.g. Sklar and Dietrich, 2001) and in-situ rock strength tests using a Schmidt hammer (Wohl and Merritt, 2001; Duvall et al., 2004; Bursztyn et al., 2015). These approaches are based on the assumption that the failure stress of rock dictates the resistance to erosion. However, the sensitivity of these techniques is not focused on the state of the upper few millimeters of the rock surface that is exposed to abrasion processes. Furthermore, the strength of rock has been shown to vary significantly with the degree of weathering processes active throughout the channel cross-section (Small et al., 2015; Shobe et

al., 2017; Murphy et al., 2018). These issues described above are some of the weaknesses of the current models of bedrock incision. In chapter four I incorporate a novel techniques of measuring rock strength using the speed that acoustic waves travel through the upper few millimeters of the surface. I then consider the degradation of the channel surface through damage inducing processes and the granular scale properties of the bedrock influence the accumulation of damage.

CHAPTER 2: EXPERIMENTAL STUDY ON THE EROSIVE ENERGY OF BED LOAD IMPACTS

ABSTRACT

Understanding bed load impact dynamics on exposed bedrock in rivers is crucial to quantifying the erosive energy of a stream. Sklar and Dietrich (2004) introduced the saltation-abrasion model in which the erosion rate of a planar bed is a decreasing function of transport stage (the boundary shear stress relative to the threshold shear stress for particle motion). The model was based on particle trajectories with out measurements of instantaneous impact velocities. Observations of the bed load saltation trajectory components relevant to the energy of impacts are lacking, particularly in channels with non-planar bed topography. In this study, we performed four flume experiments of saltating gravel to offer new insights on the dependence of particle impact dynamics on transport stage and bed topography. Our experiments used two different bed shear stresses (τ_b= 36.5 and 25.4 Pa) and two different bed configurations (planar with a standard deviation of elevation= 0.5 mm and non-planar with a standard deviation of elevation= 4.7 mm). Using high-speed video imaging we record the trajectories of saltating bed load particles to indirectly measure the impact energies in each experiment. Our results indicate a distinct change from a negative relation between the energy delivered to the bed and transport stage for a planar bed to a weakly positive to constant relation between the energy delivered to the bed and transport stage for a non-planar bed. The non-planar bed appeared to affect the impact energy by increasing the number of high-energy impacts that was evidenced by a heavy-tailed distribution of the ratio between impact velocity and hop length that was not characteristic of the planar bed. These findings suggest that non-planar bed topography generates a higher probability of extreme impact events and that bedrock erosion models should consider a distribution of possible bed load impact energies particularly for natural river channels that have rough undulating surfaces.

INTRODUCTION

In many actively eroding rivers the dominant process of incision is thought to be driven by solid particle abrasion (Whipple et al., 2000; Sklar and Dietrich, 2004) where the transport of bed load sediment imparts kinetic energy to the channel boundary through rolling, sliding, or saltating ('hopping'). Current understanding of the erosive energy delivered to the bed by sediment is based on particle hop lengths and downstream-averaged particle velocities in experiments conducted over planar bed and alluvial channels (Sklar and Dietrich, 2004). The saltation-abrasion model is a commonly used mechanistic based bedrock erosion model that applies experimentally determined relations between saltation trajectory components and transport stage (the shear stress of water flowing over the bed relative to the threshold shear stress for particle motion) to predict the erosion of a planar bed by saltating bed load particles (Sklar and Dietrich, 2004). The components of saltation are the key to understanding bedrock abrasion, assuming that the energy delivered to the bed via rolling and sliding is negligible in relation to saltation. The hop length, hop height, and downstream-averaged velocity have been studied extensively in regards to downstream sediment transport (Francis, 1973; Fernandez Luque and Van Beek, 1976; Abbott and Francis, 1977; Sekine and Kikkawa, 1992; Lee and Hsu, 1994; Niño et al., 1994; Hu and Hui, 1996). Overall, the experiments from these studies, performed with a variety of mobile and fixed alluvial beds, indicate that hop length, hop height, and downstream velocity all increase as transport stage increases (Sklar and Dietrich, 2004). Lacking information on the velocity of the particles upon impact, Sklar and Dietrich (2004) derived the vertical component of velocity based on the hop length, hop height, downstream velocity, and an assumption on the parabolic shape of the particle path between impacts. Auel et al. (2017b, 2017a) revised the saltation-abrasion model using calculated impact velocities from video imaging and showed similar but slightly different relations between saltation components and

transport stage. Their study is the only one we are aware of that observed instantaneous impact velocities and their results suggest that the energy delivered to a planar bed is independent of the transport stage and is primarily a function of sediment transport rate. Field measurements made with impact plate geophones found that the saltation-abrasion model over-estimated the energy delivered to a planar bed by up to a factor of 32 (Turowski et al., 2013).

If a mechanistic understanding of bed load impact erosion is to advance, a more complete understanding of impact energy by saltating bed load particles over a non-planar bed is required. Non-planar bed topography introduces roughness elements to the channel boundary that may increase near-bed turbulence . We know that natural bedrock rivers have non-planar bed topography and that in theory hop trajectories should be variable over non-planar surfaces. Huda and Small (2014) modeled the effects of a non-planar bed on bedrock erosion and showed that the erosion rate can increase by up to three orders of magnitude relative to the erosion rate of a planar bed. The increase in erosion rate occurred due to higher angle impacts with the surface and more occurrences of saltation trajectories being intercepted by the bed topography.

The instantaneous velocity of bed load particles upon impact has yet to be rigorously examined in flume experiments and further consideration of non-planar bed topography is needed. In this study, we use experiments of bed load saltation in a flume to revisit theoretical predictions of bed load impact energy. Our goals are to calculate the energy delivered to the bed during flume experiments using high-speed video imaging and explore the effects of non-planar beds on particle hop trajectories. We examine the effects of transport stage on particle motions over a

non-planar bed using statistical comparison with particle motions over a planar bed. Finally, using our results we consider the probabilistic nature of energy delivered to the bed in response to changes in transport stage and bed roughness.

BACKGROUND

Mechanistic models of solid particle abrasion were first developed for industrial applications (Finnie, 1960; Bitter, 1963b, 1963a). Brittle materials erode through 'deformation wear', repeated cracking of the surface that eventually breaks loose a piece of material. These models were later applied to fluvial abrasion in natural rivers (Foley, 1980; Ishibashi, 1983; Sklar and Dietrich, 2004; Lamb et al., 2008). The saltation-abrasion model of Sklar and Dietrich (2004) equates erosion rate to the product of the volume of material removed per impact (V_i), the impact rate (I_r), and the fractional area of exposed bedrock (F_e)

$$E = V_i I_r F_e. \quad (1)$$

The volume of material removed per impact (V_i) is borrowed from Bitter (1963), which equates the average volume of material removed by impacts to the kinetic energy of the impacting particle (ε_k) greater than a threshold energy (ε_t) divided by a wear resistance factor (ε_v) related to the energy required to erode a unit volume of rock

$$V_i = \frac{\varepsilon_k - \varepsilon_t}{\varepsilon_v} \quad (2)$$

where ε_t is assumed negligible at the typical energy of bed load impacts (Sklar and Dietrich, 2001) and the wear resistance factor depends on the capacity of the target material to store elastic strain energy (Engel, 1978). The kinetic energy of a single impact is a function of the

diagonal impact velocity (v_{si}), impingement angle relative to the horizontal (θ), and the bed surface angle (ϕ)

$$\varepsilon_k = \frac{\pi}{12}\rho_s D_s^3 (\sin(\theta - \varphi)\, v_{si})^2 \quad (3)$$

where ρ_s is particle density, D_s is the diameter of a characteristic grain size, $\pi/12\,\rho_s D_s^3$ is half of the mass of the particle assuming a spherical shape, ϑ is always positive, and φ is negative for upstream facing surfaces and positive for downstream facing surfaces (Figure 1.1). Note that in this setup of equation 3, impact energy increases for negative φ and decreases for positive φ. Sklar and Dietrich (2004) assumed a planar bed and thus quantified the kinetic energy per impact as

$$\varepsilon_k = \frac{\pi}{12}\rho_s D_s^3 w_{si}^2, \quad (4)$$

where w_{si} is the vertical component of impact velocity, which would be normal to a planar bed (Figure 1.1). The impact rate per unit area (I_r) is the mass flux of sediment per unit width (q_s) divided by the mass of a particle with diameter D_s and the hop length (l_s)

$$I_r = \frac{6q_s}{\pi\rho_s D_s^3 l_s}, \quad (5)$$

Note that as hop length increases the impact rate and thus the erosion rate decreases. The fraction of exposed bedrock (F_e) depends on the ratio of sediment flux (q_s) to transport capacity (q_t). F_e is not considered beyond this general introduction as the transport capacity far exceeded the sediment flux throughout all of our experiments. Thus, for the purposes of this paper the total erosional energy delivered to the bed (ε_{kt}) per unit bed area and time is expressed as the product of the kinetic energy per impact (ε_k) (Equation 4) and the impact rate (I_r) (Equation 5) characteristic of particle size D_s

$$\varepsilon_{kt} = \varepsilon_k I_r = \frac{q_s w_{si}^2}{2 l_s}, \quad (6)$$

and the efficiency of a saltating particle (ε_{ki}) depends on the the impact velocity and the hop length

$$\varepsilon_{ki} = \frac{w_{si}^2}{2 l_s}. \quad (7)$$

Note that when an impact occurs on non-planar topography the velocity normal to the surface ($\sin(\theta - \varphi)\, v_{si}$) must replace w_{si} in any of the equations that include impact velocity.

The trajectory of an individual grain depends on a multitude of factors including the hydrodynamic drag and lift forces, particle weight, fluid motions relative to the particle, particle rotation, and particle collisions with the bed and other grains (Wiberg and Smith, 1985). The saltation-abrasion model takes a simplified approach of these factors and predicts particle trajectories as a function of transport stage (T^*)

$$T^* = \left(\frac{\tau^*}{\tau_c^*} - 1\right) = \frac{\rho_w g R S}{[(\rho_s - \rho_w) g D_s^3] \tau_c^*} - 1, \quad (8)$$

where τ^* is the nondimensional Shield's stress $\tau_b/(\rho_s - \rho_w) g D$ ($\tau_b = \rho_w g R S$), τ_c^* is the value of τ^* at the threshold of sediment motion, ρ_w is water density, *g* is gravitational acceleration, *R* is the hydraulic radius, and *S* is slope. As transport stage increases so does the shear stress on a particle. This results in higher particle velocities, which alone would increase the energy delivered to the bed; but longer hop lengths, which alone would reduce the energy delivered to the bed. The relation between transport stage and both hop length and impact velocity determines how the erosion rate scales with hydraulic forcing. Thus, a negative relation would

imply that river incision is more efficient during low runoff than during high magnitude storms and a positive relation would suggest the opposite.

EXPERIMENTAL SETUP

Our experiments were conducted in a large-scale sediment flume at the University of Idaho, Center for Ecohydraulics Research, Mountain StreamLab (Budwig and Goodwin, 2012). Water and rounded granitic gravel were continuously fed through the flume while saltation trajectories were observed along a viewing window 10 m downstream of the gravel entry point (Figure 1.2). Sediment was caught at the bottom of the flume in a sediment trap and then manually returned to the feeders. A sediment feed rate of 0.15 kg/sec was chosen for all runs to avoid significant effects from particle-particle collisions and reduce the likelihood of clogs in the sediment trap. Along the viewing window, two rows of 13 disc shaped bedrock samples were attached to the flume floor (Figure 1.2). The discs were laid flat for planar bed experiments and were tilted upstream for the non-planar bed experiments. The two longitudinal rows were spaced 5 cm apart in the cross-stream direction and within each row discs were spaced 4 cm apart. The samples in the left-hand row (in the direction of flow) had smooth cut surfaces and the samples in the right-hand row were comprised of weathered channel bed samples with local roughness features. For the purposes of this study, only the particle trajectories over the smooth surface samples were recorded. We did not observe any lateral (perpendicular to the direction flow) movements in particle paths caused by local roughness features of the weathered samples and we therefore neglected any influence of the weathered samples surface topography on the trajectories of particles that were recorded.

We performed 4 runs in total. In the first two runs bedrock samples were set flush with the flume floor to maintain a planar bed by cutting a hole into the flume floor that was the same dimensions as the sample. The flow conditions for run 1 and run 2 were chosen based on the criteria that (1) bed slopes should be representative of river channels from which the bedrock samples were extracted (channel slopes of field sites range between 0.01 and 0.05), (2) the shear stress must be significantly greater than the threshold for motion shear stress to avoid deposition or sediment cover effects, and (3) differences in saltation hops between runs would be visually distinct (i.e. more vigorous but less frequent impacts for the high shear stress and weaker but more frequent impacts for the low shear stress). The slopes, discharges, shear stresses, and hydraulic scaling Froude number of the conditions to satisfy these criteria are listed in Table 1.1. Between runs 1 and 2 we decreased the bed shear stress by lowering the flume slope and water discharge. Runs 3 and 4 had the same flow conditions as runs 1 and 2 respectively, however the bedrock samples were inclined to an upstream facing angle of -10° thereby increasing both the impact angle of saltating particles and bed roughness.

The flume floor was made of marine plywood covered with perforated steel sheeting to protect the bed from erosion. The perforated steel sheeting was 1.3 mm thick with 1.6 mm diameter holes covering 23% of the area creating a roughness (k_s) of 0.52 mm, which is the standard deviation of surface elevation of the steel sheet. We consider this roughness estimate to be a maximum because it does not include the surface of the smooth bedrock samples, which would decrease the overall roughness. In runs 3 and 4 the bed roughness (k_s) was 4.7 mm (standard deviation of elevation) due to the inclination of bedrock samples and the metal bed surface between samples. We estimated the critical Shield's stress (τ_c^*) of gravel on the steel sheeting by

measuring the Shield's stress (τ^*, equation 8) at the initiation of motion. We placed five pieces of gravel (grain sizes of 10-61 mm) in the flume and slowly raised the water depth by increasing the flow rate until the particles moved. We repeated this procedure three times for both bed slopes used in our experiments (0.033 and 0.023), and averaged the critical Shield's stresses to $\tau_c^* = 0.0167 \pm 0.004$ std (slope of 0.033) and $\tau_c^* = 0.0145 \pm 0.0016$ std (slope of 0.023). Because the difference in τ_c^* between the two slopes is small and is within the error of our measurements we used the average of the two values (τ_c^* = 0.0156) for all analyses. Our value of τ_c^* is less than typical alluvial beds (0.03 – 0.08), greater than that for gravel on plexiglass (0.005) (Auel et al., 2017a), and similar to sediment transported on planar bedrock with grooves (0.015) (Chatanantavet, 2007).

The sediment used for all experiments was natural river gravel. Using pre-sieved 20 cm gravel from a local quarry we further narrowed the grain size distribution by removing the material that fell through a mesh with 1.3 cm openings. Based on 100 randomly sampled gravels we estimated the composition of our sediment to be 73% granitic, 17% basalt, and 10% other rock type. The distribution of intermediate axis diameters had a mean of 23.8 mm ± 5.5 std and a mean Corey Shape Factor of 0.57 ± 0.13 std (Figure 1.3). A CSF of 1 means the particle shape is spherical and smaller values describe prolate or oblate particle shapes.

METHODS FOR MEASURING SALTATION TRAJECTORIES AND VELOCITIES

The saltation trajectories and velocities were recorded for a duration of 60 seconds for each experimental run. A high-speed camera capturing 240 frames per second with a resolution of 240 x 1130 pixels recorded the sediment position with time through a clear glass wall of the

flume. The camera was positioned perpendicularly to the side of the flume at a height level with the flume floor and at a distance from the flume able to capture a frame length of ~1.5 m along the centerline of the flume (Figure 1.2). Within the frame of view, saltating sediment was backlit by angling six 150-watt bulbs to reflect light off of the back wall of flume (Figure 1.2). Backlighting the water column occurred for the image processing to provide sharp edge definition of saltating sediment. The lights were angled in order to only allow sediment travelling between the centerline of the flume and glass wall to be visible. Gravel traveling along the back half of the flume was lit on the side facing the camera causing it to blend into the white background while gravel traveling along the front half of the flume was in a shadow causing it stand out from the brightly lit back wall of the flume.

Calculating Saltation Trajectory Components and Particle Grain Size from Images

Individual particles were tracked through image sequences using an edge detection algorithm to identify the dark side of a particle on the brightly lit white background. Normalizing the image by the mean gray-scale value, applying a smoothing filter, and applying a pixel tolerance on captured images enhanced the ability of the algorithm to accurately track particles. Our procedure was to track every particle as it entered the field of view and record the particle trajectory after the first impact. This was done so that only the hops that impacted the bed area within the imaging window were considered. For each frame of every particle tracked, we recorded the pixel area of the particle, the position in x and z of the particle's center point, and time. This usually resulted in several impacts for a single particle. The number of impacts recorded for each run is listed in Table 1.1. The edge detection algorithm would fail when particles overtook one another and in these cases the trajectory data were discarded.

The hop length, impact velocities, and impingement angle are the quantities leading up to the impact. The particle path was smoothed by fitting 3rd degree polynomial over a moving window (20 neighboring points) along the particle path because the rotation of a non-spherical particle will cause the center point to oscillate around the trajectory path (Figure 1.4). Removing these higher frequency oscillations allowed accurate identification of minima and maxima of the particle path from which we calculated the point of impact (minima), hop length (distance between minima), and hop height (distance between the bed and the maxima). The instantaneous particle velocity upon impact (w_{si} and v_{si}) are estimated from the vertical component of velocity ($w_s = {\Delta z}/{\Delta t}$), and the diagonal component of the velocity $\left(v_s = \sqrt{{\Delta x}/{\Delta t} + {\Delta z}/{\Delta t}}\right)$ using the difference between the particle's *x* and *z* positions averaged over two consecutive images prior to impact (Auel et al., 2017b) (Figure 1.4 inset)

$$w_{si} = \frac{w_{s(i-1)} + w_{s(i-2)}}{2}, \tag{9}$$

$$v_{si} = \frac{v_{s(i-1)} + v_{s(i-2)}}{2}. \tag{10}$$

Images were scaled by placing a measuring tape within the captured frame.

In this study, we quantified the scaling relation between non-dimensional saltation components and transport stage, which are useful for scaling across many different environments (e.g. flumes and rivers). Here, we used the same non-dimensional forms as previous authors (Sklar and Dietrich, 2004; Auel et al., 2017a, 2017b) of hop length

$$\frac{l_s}{D_s}, \tag{11}$$

vertical impact velocity

$$\frac{w_{si}}{\sqrt{R_b g D_s}}, \tag{12}$$

diagonal impact velocity

$$\frac{v_{si}}{\sqrt{R_b g D_s}}, \tag{13}$$

as well as erosional efficiency of impacts on a planar bed

$$\frac{\varepsilon_{ki}}{R_b g} = \frac{w_{si}^2}{2R_b g l_s}, \tag{14}$$

and a non-planar bed

$$\frac{\varepsilon_{ki}}{R_b g} = \frac{\sin(\theta-\varphi) v_{si}^2}{2R_b g l_s}, \tag{15}$$

where R_b is the non-dimensional buoyant density of the sediment, $(\rho_s/\rho_w) - 1$. The transport stage of each particle depends on the intermediate axis diameter of the particle (equation 8). The edge detection algorithm identifies the long and short axes as the longest and shortest diameter through the center point of the two dimensional projection of the particle. The intermediate axis of the particle in each frame was estimated as the average of the short and long axis. For each particle the intermediate axis of all image frames captured for the particle were averaged into a single value (D_s) for that particle.

Error Estimation

The depth of field across the width of the flume added uncertainty to the position of particles. The lights were angled to only allow sediment travelling between the centerline of the flume and glass wall to be visible, which divided the depth of field to the front half of the flume. We can be sure that sediment that was backlit was traveling within the front half of the flume, but we cannot be certain of the exact particle path. Therefore we estimated hop trajectories and velocities using *x* and *z* positions along an assumed a median path that bisects the front half of the flume (Figure 1.2). By placing scale bars within the field of view, we measured the streamwise distance along the front glass (1.473 m) and the streamwise distance along the flume centerline (1.635 m). From the camera's perspective this equates to a distance of 0.0801 m per one degree along the front glass, a distance of 0.0889 m per one degree along the centerline, and a distance of 0.0845 m per one degree along the assumed median path that bisects the front glass and centerline. Thus assuming that the particle traveled along the median path the largest error would occur if the particle actually traveled either along the front glass or the centerline. Therefore, the uncertainty of all length and velocity measurements is ± 5.2% of the distance traveled in *x* and *z* directions.

RESULTS

Hop Trajectories Over a Planar Bed

Here we focus on three key saltation components of the saltation-abrasion model: the dimensionless vertical impact velocity ($w_{si}/(R_b g D_s)^{0.5}$), the dimensionless hop length (l_s/D_s) of impacting particles, and the dimensionless impact energy efficiency ($\varepsilon_{ki}/R_b g$) and how they scale with transport stage. For simplicity we neglect local turbulent fluctuations of bed shear stress, and therefore, assume that transport stage varies only according to the diameter (D_s) of

each particle and mean bed shear stress of each experiment. We plot the regressions of previous authors (Sklar and Dietrich, 2004; Auel et al., 2017a, 2017b) in Figure 1.5 for comparison with our data.

The vertical component of the particle velocity (w_{si}) is a controlling factor in the energy per particle impact. The raw values of w_{si} range between 0.003 and 0.24 m/s for run 1 (τ_b= 36.5 kg/ms^2) and 0.005 and 0.19 m/s for run 2 (τ_b= 25.4 kg/ms^2). Here the dimensionless vertical impact velocity shows weak dependence on transport stage

$$\frac{w_{si}}{(R_b g D_s)^{1/2}} = 10^{-1\pm0.1}\left(\tau^*/\tau_c^* - 1\right)^{0.17\pm0.19}, \quad (16)$$

where the error on the exponents is the 95% confidence interval (Figure 1.5a). The regression of Sklar and Dietrich (2004) over predicts the non-dimensional impact velocity by an order of magnitude. The regression of Auel et al (2017b) is close to ours and within the error bounds of our regression coefficients.

The hop length (l_s) of particles partly determines the impact rate. Longer hops result in fewer impacts and thus less energy delivered to the bed. The raw values of l_s range between 0.093 and 1.38 m for run 1 and 0.12 and 0.84 m for run 2. The non-dimensional form of hop length scales with transport stage according to

$$\frac{l_s}{D_s} = 10^{0.8\pm0.15}\left(\tau^*/\tau_c^* - 1\right)^{0.6\pm0.3}. \quad (17)$$

The scaling relationship of Sklar and Dietrich (2004) is within the error bounds of our regression coefficients, where the magnitude of Sklar and Dietrich's (2004) hop lengths are the same to 3.2 times less than our hop lengths in the range $0.4>T^*>25$ (Figure 1.5b). However, the regression of Auel et al (2017a) is outside of our error bounds.

The erosive kinetic energy delivered to the bed (ε_{ki}) accounts for both the energy upon impact and the impact rate through ratio of w_{si}^2 and l_s. The scaling relationship between the our observed dimensionless ε_{ki} and transport stage is

$$\frac{\varepsilon_{ki}}{R_b g} = \frac{w_{si}^2}{2R_b g l_s} = 10^{-3.2\pm0.05}\left({\tau^*}/{\tau_c^*} - 1\right)^{-0.25\pm0.1}. \quad (18)$$

The correlation between dimensionless ε_{ki} and transport stage is negative because the impact rate decreases more drastically with increasing transport stage than does the square of impact velocity. This is consistent with the findings of Sklar and Dietrich (2004) where the erosion rate is predicted to peak at low transport stages and then decrease as hop lengths grow longer and longer (Figure 1.5c). However, our observed energy values are roughly an order of magnitude less than their predicted energies. The regression of Auel et al (2017b) is closer to our regression than Sklar and Dietrich (2004), but is still not within our error bounds. Furthermore, our data implies that dimensionless ε_{ki} decreases with increasing transport stage whereas (Auel et al., 2017b) show no dependence.

Hop Trajectories Over a Non-Planar Bed

Here we focus on the results of the non-planar bed and include calculations of the dimensionless diagonal impact velocity (Figure 1.6). In the non-planar experiments, the vertical

impact velocity was more sensitive to transport stage than in the planar bed experiments (Figure 1.6a)

$$\frac{w_{si}}{(R_b g D_s)^{1/2}} = 10^{-1\pm0.05}\left(\tau^*/\tau_c^* - 1\right)^{0.28\pm0.19}. \quad (19)$$

However, the impact energy for the non-planar bed is a function of the velocity normal to the impact angle ($\theta - \varphi$). Thus, for a φ of 0° equation 19 is valid. For impacts on the tilted disc surfaces ($\varphi = -10°$), the impact velocity normal to the surface has a stronger positive correlation with transport stage than the vertical impact velocity (Figure 1.6b)

$$\frac{\sin(\theta-\varphi)v_{si}}{(R_b g D_s)^{1/2}} = 10^{-0.7\pm0.05}\left(\tau^*/\tau_c^* - 1\right)^{0.34\pm0.1}, \quad (20)$$

where ϕ= -10° and θ is calculated for each impact from the image analyses. Equations 19 and 20 represent the range of impact velocities for runs 3 and 4. There was very little change in the dimensionless hop length scaling between the planar and non-planar bed experiments (Figure 1.6c)

$$\frac{l_s}{D_s} = 10^{0.8\pm0.15}\left(\tau^*/\tau_c^* - 1\right)^{0.53\pm0.3}. \quad (21)$$

The dimensionless energy delivered to the bed had a slightly positive relation with transport stage on the non-planar surfaces (Figure 1.6d)

$$\frac{E_{ki}}{R_b g} = \frac{(\sin(\theta-\varphi)v_{si})^2}{2R_b g l_s} = 10^{-2.5\pm0.1}\left(\tau^*/\tau_c^* - 1\right)^{0.08\pm0.15}, \quad (22)$$

whereas the planar bed experiments showed a negative relation (Figure 1.5c). These results imply that the energy delivered to the bed increase with higher transport stages for non-planar

beds with bed topography as subtle as our non-planar flume floor that has a standard deviation of elevation of 4.7 mm.

Statistical Tests Between Planar and Non-Planar Data

Here we explore how non-planar bed topography affects the following components of particle saltation: dimensionless hop length (l_s/D_s), impingement angle (ϑ), and dimensionless hop height (h_s/D_s). We determine the statistical likelihood that the distributions of particle trajectory components from the different experiments are distinct from one another. This allows us to further examine the influence of shear stress and bed topography on saltation hop trajectories that is not observable with the regression analyses above. Using the two-sample Kolmogorov-Smirnov goodness of fit test (k-s test) we test the null hypothesis that the distribution of values of the saltation trajectory components of the separate experiment runs could come from the same continuous distribution. The likelihood of the null hypothesis is determined by the significance level (p). For example a p value is less than 0.05 indicates a greater than 95% certainty that the distributions are distinct. For each saltation component listed above we test the null hypothesis for (1) a planar bed with unequal τ_b (runs 1 and 2), (2) planar bed vs. non-planar bed for τ_b= 36.5 kg/ms^2 (runs 1 and 3), (3) planar bed vs. non-planar bed for τ_b= 25.4 kg/ms^2 (runs 2 and 4), and (4) a non-planar bed with unequal τ_b (runs 3 and 4). Figure 1.7 shows the cumulative distribution functions of saltation components for each run and the results of Kolmogorov-Smirnov tests.

Hop length

All k-s tests show that dimensionless hop length is statistically distinct ($p<0.001$) between experiments (Figure 1.7a) implying that hop length is sensitive to differences in bed shear stress and bed topography. Hop lengths are expected to increase with higher shear stresses, but the non-planar bed shows interesting behavior. Between the planar and non-planar experiments at the weaker flow (run 2 and 4), the non-planar bed caused statistically significant shorter dimensionless hop lengths than the planar bed. However, at the stronger flow the opposite effect occurred between planar and non-planar experiments (runs 1 and 3). Note that there is no difference between the regressions of planar and non-planar hop lengths (equations 17 and 21), but the distributions in Figure 1.7a show opposing responses between lower and higher shear stresses. This suggests that the roughness of the non-planar bed either impedes the flow velocity or the increased angle of impact shortens hop trajectories or both, but it is beyond the scope of this study and available data to distinguish the relative contributions of these factors.

Impingement Angle

Holding bed topography similar and changing the shear stress of the experiments (runs 1 vs. 2 and runs 3 vs. 4) resulted in a statistically significant lower particle impingement angles (θ) for the stronger flows (Figure 1.7b). Lower impact angles are expected to occur as bed shear stress increases and hop trajectories become longer and flatter (Auel et al., 2017a, 2017b). Holding bed shear stress similar and changing bed topography (runs 1 vs. 3 and runs 2 vs. 4) shows that at the stronger flow the impingement angles are not statistically distinct, but at the weaker flow the non-planar bed alters the trajectories with statistical significance ($p=0.03$) to have higher arcs and shorter hop lengths (demonstrated in Figure 1.7a). The statistical similarity of the shape of trajectories between the planar and non-planar experiments at the stronger flow (runs 1 vs.

3) could be partly due to the higher shear stress on the particle counteracting the increase in vertical rebound velocity that the inclined bed surface causes. With the available data it is difficult to understand why the non-planar bed did not significantly alter the impingement angles for the stronger flow and did for the weaker flow; but this does imply that at higher shear stresses any differences in energy delivered to a non-planar bed relative to a planar bed are not caused by changes in impingement angle.

Hop Height

Statistical tests suggest that the values in the distribution of hop heights are overall greater for higher bed shear stresses for both planar and non-planar beds (Figure 1.7c). This result is consistent with previous studies (Sklar and Dietrich, 2004; Auel et al., 2017a). Statistical tests also show that at higher shear stresses the distributions of hop heights over the non-planar bed are distinct from the planar bed ($p<0.0001$) and that hop heights are greater for the non-planar bed. However, at lower shear stresses it is more likely that the distributions of hop heights are indistinct ($p=0.2$).

Together these trajectory components (l_s, θ, and h_s) suggest that at the higher shear stresses particle trajectory shapes of non-planar beds are similar but scaled up from those of the planar beds (Figure 1.8). However, at the lower bed shear stress the non-planar bed had shortened hop lengths but hop heights were un-affected (statistically). This may be explained by the effect that relative roughness (ratio between the hydraulic roughness of the channel and flow depth) has on the flow. At the lower shear stress there is a higher relative roughness than at the higher shear stress. The effects of bed roughness (in the form of bed topography) are likely stronger on

the flow field, and thus, decrease the particle velocity for lower shear stresses. With the available data it is difficult to quantify a relation between relative roughness and trajectory components; but these results do suggest that the relative roughness of the bed could be an important factor in the saltation trajectories over non-planar bed topography.

Power Law Distribution Analyses

Both the dimensionless vertical impact velocity and the dimensionless hop length show almost an order of magnitude variation at most transport stages (Figures 1.5a,b and 1.6a,b). As a result, the non-dimensional energy delivered to the bed, which is a function of both impact velocity and hop length, can vary across four orders of magnitude within our range of transport stages (Figures 1.5c and 1.6c). To consider the statistical implications of such wide variation of impact energies we plot the cumulative distribution of dimensionless ε_{ki} in log-log space (Figure 1.9). The data on the right-hand side of these distributions (the 'tail') appears linear in log-log space and therefore likely follows a power law. We calculate the power law slope (α) of the tail of the distribution with

$$\alpha = 1 + n\left[\sum_{i=1}^{n} ln\frac{c_i}{c_{min}}\right]^{-1}. \quad (23)$$

where $c_{\min}$ is the smallest value for which the distribution is linear in log-log space and n is the number of data points greater than $c_{\min}$ (Newman, 2005). An estimate of the expected statistical error on equation 23 is given by (Newman, 2005)

$$\sigma = \frac{\alpha-1}{\sqrt{n}}. \quad (24)$$

The smaller the value of α is the 'heavier' the tail of the distribution. For any distribution where $2<\alpha<3$, the second moment of the distribution (the variance) may not converge to a finite value because a larger sample of observations is more likely to include an extreme value (Newman, 2005). Thus in our case, a heavy tail distribution of the observed impact energies would imply that the observed energy delivered to the bed would increase with the number of observations and that a regression through the average dimensionless ε_{ki} for a given transport stage would underestimate the energy delivered to the bed.

Figure 1.9 shows a comparison of the distributions of dimensionless ε_{ki} between the planar and non-planar bed experiments. For the planar bed experiments dimensionless ε_{ki} is calculated using the vertical impact velocity (equation 14) and for the non-planar bed ε_{ki} is calculated using the velocity normal to the bed (equation 15) using a φ of 0° and -10° as these are the two bed surface angles of the non-planar bed. The tail of the distribution of dimensionless ε_{ki} from the planar bed experiments does not suggest high randomness and the variance converges to a finite value. The dimensionless ε_{ki} of the non-planar bed takes on a heavy tail for both bed surface angles and the slopes of the distribution tails (α) of both non-planar scenarios suggest a divergent variance. Note that the 0° case essentially uses the vertical velocity component and that the distribution only deviates from the planar bed data at the tail of the distribution. This implies that the non-planar bed mostly affects the energy delivered to the bed by increasing the probability of anomalously high-energy impacts.

DISCUSSION

Overall, our results suggest that the erosive energy delivered to the bed is a negative function of transport stage for the planar bed but that relation shifts towards a weakly positive to constant function for the non-planar bed. Furthermore, we find that the non-planar bed generates more anomalous high-energy impacts than the planar bed. These findings suggest that bed load abrasion, similar to the stochastic nature of downstream bed load transport, is a process in which extreme events are responsible for most of the erosion. We acknowledge that this study does not comprise an exhaustive set of experiments testing a very large range of transport stages, grain sizes, or bed roughness conditions; and more thorough considerations of bed roughness, particle shape, and other relevant factors are needed to work towards a complete understanding of bedrock channel erosion. Nonetheless, this work reveals distinct differences in saltation behavior caused by a non-planar bed and adds calculations of key impact parameters to the literature on bed load impact erosion.

Hop Trajectories Over Planar Beds

At low transport stages (T^*<3) normalized w_{si} and l_s each tend towards a relatively constant value. The dimensionless w_{si} of our experiments approach a constant value of roughly 0.1, which is not that dissimilar to the value of 0.2 found by Auel et al. (2017b). Below an excess transport stage of 2 the normalized hop lengths here approach a constant value of roughly 8, where the hop length is 8 times greater than the particle diameter. The data in Auel et al (2017a) deviates from a power law in similar way for large (D_s= 16.5 ± 1.1 mm) irregular-shaped particles. The decreased sensitivity of w_{si} and l_s (Figure 1.5a, b) to lower transport stages suggests that near the onset of sediment motion, the energy delivered to the bed only varies with the sediment supply rate (equation 6). At higher transport stages (T^*> 3) our results suggest that the energy

delivered to a planar bed decreases with transport stage (Figure 1.5c), which is consistent with the findings of Sklar and Dietrich (2004). These results imply that the erosion of smooth planar beds (i.e. concrete structures) is more efficient at low transport stages and that large runoff events are less important than more frequent runoff events that produce transport stages just above the threshold for motion.

The hop trajectories from our planar bed experiments (Figure 1.5) show some similarities to the data of previous authors (Sklar and Dietrich, 2004; Auel et al., 2017a, 2017b), but not without considerable differences in either the magnitude of saltation components or their trend with transport stage. This may be due to a contrast in bed roughness or the shape of particles used in these experiments. The types of beds in the dataset used by Sklar and Dietrich (2004) vary between mobile-alluvial and fixed-alluvial with k_s ranging from 1.4 to 31 mm, and particle shapes that were both spherical and irregular. This wide range of conditions and lack of instantaneous impact velocity measurements makes it difficult to infer the source of disparity between the dimensionless ε_{ki} of our experiments and the consolidated dataset of Sklar and Dietrich (2004). However, Auel et al (2017a) uses a single bed type and quantified particle shape. The roughness of our bed (k_s= 0.5 mm) is similar to the plane mortar bed of Auel et al (2017b), which was k_s= 0.2 mm. Auel et al (2017a) used the roundness factor (K_r) (Woldman et al., 2012) to quantify particle shape

$$K_r = \frac{P^2}{4\pi A}, \tag{24}$$

where P is the particle's perimeter and A is the area of the particle's two-dimensional projection. For a spherical grain K_r= 1 and for a prism that is twice as long as it is thick K_r= 1.433.

Half of the grains used by Auel et al. (2017a) were spheres and the other half were irregular shaped grains for which they report a roundness factor of $1.0<K_r<1.3$. Assuming a smooth elliptical shape we use the short and long axes to estimate P we measure a median K_r of 1.45 with standard deviation of 0.45 for all particles captured in video. Our assumption of a smooth elliptical shape discounts irregular shapes and thus our estimation of K_r is a minimum. While the bed roughness of our planar bed does not differ much from Auel et al (2017a, 2017b) the difference in roundness factor suggests that bed load impact dynamics may be sensitive to particle shape irregularity. The experiments of Auel et al. (2017b) showed no dependence of energy delivered to the bed on transport stage (solid line in Figure 1.5c). Our experiments show that as transport stage increases the increases in hop length suppress the impact rate to a degree that counteracts the faster impact velocities, which ultimately causes the energy delivered to the bed to decrease with transport stage. If this effect is sensitive to grain shape then one might expect the erosion rate of a planar bed to decrease more strongly with transport stage for grain shapes that are more irregular than what we used, but more work is needed to address the effect of grain shape specifically on instantaneous impact velocity.

The Effect of Non-Planar Beds on Saltation Trajectories

Our results suggest that the erosion rate of a non-planar bed weakly increases or is constant with transport stage. The saltation-abrasion model is based on the assumption of a planar bed where the vertical impact velocity is normal to the surface, however this is rarely the case in natural streams, which usually have some bed topography. The angle of the bed surface relative to the trajectory of an impacting particle can significantly alter the energy of the impact through the impact angle (i.e. low-angle glancing contact to a high-angle direct contact) or through the

effects on the particle trajectory. Particle trajectories are affected either by the previous rebound of the particle on a non-planar surface or by the turbulence generated by the non-planar surface. Step features such as the surface of our non-planar bed create flow separation, which can cause (Nelson et al., 1995) the magnitude and frequency of turbulence structures to vary dramatically downstream of the step (Nelson 1995). In the experiments of, a single 10 cm step caused greater turbulence intensity and more variable sediment velocities (vertical and horizontal) than a planar bed. Although the average transport rate was greater for the planar bed, peak instantaneous transport rates were higher for the non-planar bed. Vortex shedding and wake flapping behind a sharp break in bed elevation create low frequency fluctuations in flow velocity (Bradshaw and Wong, 1972; Simpson, 1989). Measuring near-bed fluid flow at turbulent-resolving frequencies was beyond the scope of our study. Thus, we cannot determine the relative of influence the particle's rebound or the turbulence on the particle's trajectory.

Ultimately, the dependence of energy delivered to the bed on transport stage is a factor of the change in hop length relative to the change in impact velocity. Between planar and non-planar experiments, the change in hop length was negligible but the impact velocity normal to the bed increased significantly for the non-planar bed. This effect may depend on the roughness height of the bed relative to the water depth. For beds with topography that further increase the impact velocity normal to the bed while causing relatively smaller changes in hop length the relation between energy delivered to the bed and transport stage will become more positive than what these experiments demonstrate. Depending on the bed roughness effects on the turbulent structure the energy delivered to the bed could increase with higher transport stages,

which occurred in the experiments of Johnson and Whipple (2007) who observed an increase in the erosion rate after an inner channel was eroded into a planar concrete channel.

Stochasticity of Bed Load Impacts

We show that ε_{ki} for a non-planar bed follows a heavy-tailed distribution (Figure 1.9) and thus complicates our ability to predict bed load abrasion. Heavy-tailed distributions violate the Central Limit Theorem where anomalously large values skew the distribution and prevent statistical moments from converging to finite values (Newman, 2005). Since (Einstein, 1950) authors have considered the downstream motions of bed load to be stochastic (Nikora et al., 2002; Ganti et al., 2010; Hill et al., 2010; Furbish et al., 2012; Martin et al., 2012; Fathel et al., 2015; Bradley et al., 2018). For the most part these studies reveal that the downstream travel length and velocity of bed load sediment follow exponential distributions with some evidence of heavy-tail distributions of sediment wait times (time between particle motions) (Nikora et al., 2002), of sediment transport rates over short sampling times (Hill et al., 2010), and of sediment travel distances for mixed-particle sizes (Hill et al., 2010). It has been suggested through experimental studies that the highly random nature of sediment transport is due to turbulent fluctuations (Nelson et al., 1995; Papanicolaou et al., 2001; Diplas et al., 2008). Lamb et al. (2008) modified the saltation-abrasion model to include a turbulence effect on the vertical impact velocity that accounts for the vertical fluctuations in the flow field

$$w_{si} = \overline{w_{si}} + w', \tag{25}$$

where $\overline{w_{si}}$ is defined by equation 16 and w' is a random number drawn from a normal distribution of mean zero and standard deviation equal to the shear velocity of the flow ($(\tau_b/\rho_w)^{1/2}$). Their modification provides a framework to consider the random variation of

impact energies. The results in this study, although limited to two flow stages and two bed topographies, suggest that the distribution of impact efficiencies have heavy, power law tail for non-planar beds (Figure 1.9), which a normal distribution would not capture. In natural settings where local variations in flow turbulence and bed roughness are common, greater probabilities of extreme impact energies may require a probabilistic consideration of saltation trajectories that captures the large-value skewness typical of stochastic processes.

CONCLUSION

We have used high-speed video imaging to indirectly quantify the erosive energy delivered to the bed by saltating gravel-sized sediment in flume experiments. Our results suggest complex behavior in saltation trajectory components responsible for the energy delivered to the bed. The data suggest a threshold at an excess transport stage of 3 below which the energy delivered to the bed does not vary with transport stage. Above this threshold the energy delivered to the bed decreases with transport stage for a planar bed. For non-planar beds the energy delivered to the bed increases weakly with transport stage. Furthermore, the non-planar bed affected saltation trajectories in a manner that increased the probability of extreme impact energies. This stochastic behavior of bed load impacts suggests a probabilistic rather than deterministic approach to predicting erosion by bed load may be appropriate. The results herein suggest that particle trajectories are sensitive to grain shape and the ratio of flow depth to bed roughness (relative bed roughness) and emphasizes the need for future research to focus on the influences of these factors on the relation between transport stage and the erosive energy of bed load impacts.

Table 1.1: Experimental Conditions

Table 1: Experimental Conditions

	Rock Sample φ (°)	Water Discharge (m^3/sec)	Flume Slope	*H* (m)	Water Velocity (m/sec)	τ_b (kg/ms^2)	*T** of mean Grain Size	$H/D_{s\text{-}mean}$	Froude number	number of impacts recorded	k_s (mm)
run1	0	0.429 +- 0.013	0.033	0.165 +- 0.005	2.62 +- 0.16	36.5	5.22	6.93277	2.2	174	0.5
run2	0	0.256 +- 0.002	0.023	0.133 +- 0.003	1.93 +- 0.06	25.4	3.18	5.58824	1.8	188	0.5
run3	-10	0.429 +- 0.013	0.033	0.165 +- 0.005	2.62 +- 0.16	36.5	5.22	6.93277	2.2	178	4.7
run4	-10	0.256 +- 0.002	0.023	0.133 +- 0.003	1.93 +- 0.06	25.4	3.18	5.58824	1.8	158	4.7

Corey Shape Factor (*CSF*) = $c/(ab)^{0.5}$, where *a*, *b*, and *c* are the long, median, and short axes respectively. Water Velocity, U=Q/WH, where Q, W, and H are water discharge, flume width, and water depth respectively. Water discharge was continuously measured and controlled by magnetic flow meters and error reported represents the maximum fluctuation in the volume flow rate detected by the flow meters. Water depth was measured by hand from the flume floor to the water surface at three locations along the particle trajectory recording zone and averaged.

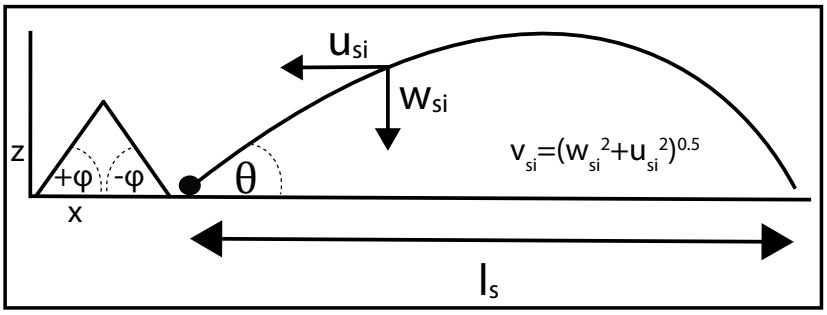

Figure 1.1: Saltation trajectory diagram. Shown are the hop length (l_s), vertical impact velocity (w_{si}), horizontal impact velocity (u_{si}), diagonal impact velocity (v_{si}), impingement angle (θ), and bed surface angle (ϕ).

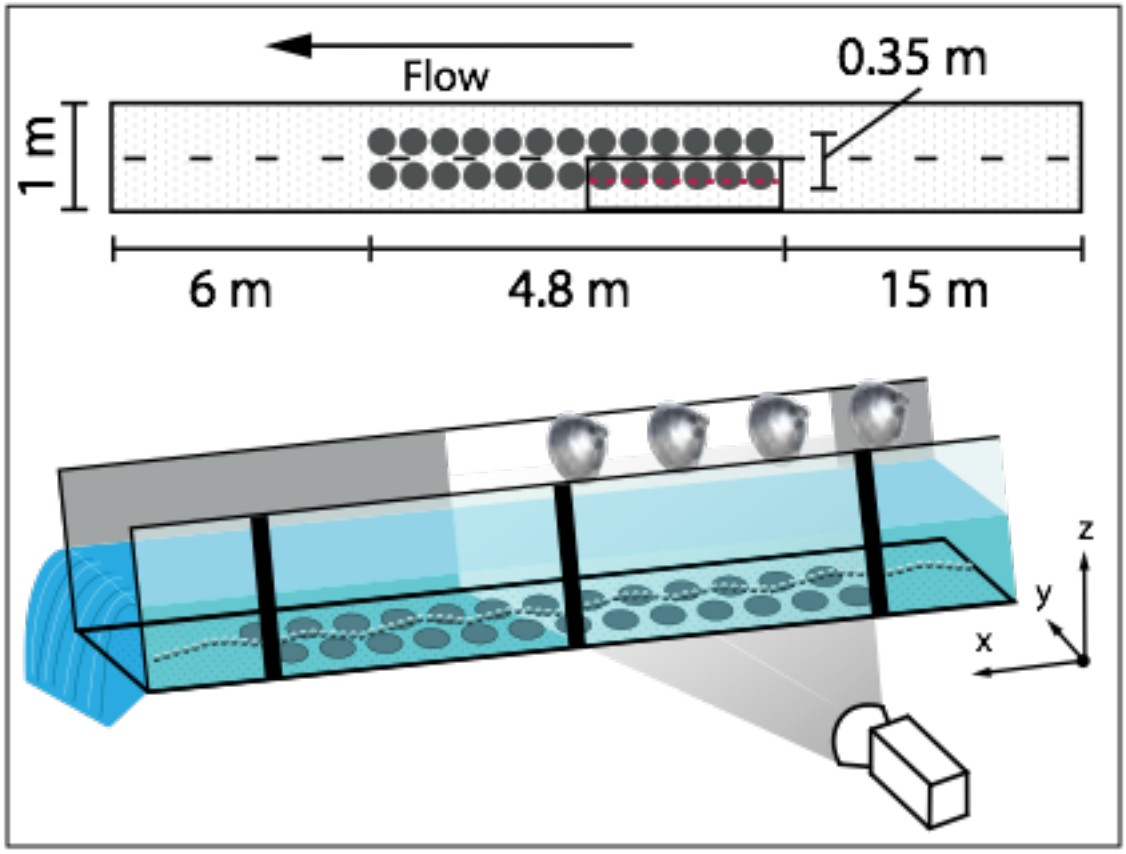

Figure 1.2: Experimental Setup. The top diagram is not drawn to scale. Black dashed line is the centerline of the flume in the longitudinal direction. The black box outlines the area of the bed captured in video. The red dashed line is the assumed path of particles captured in video. The middle diagram shows the lighting and camera set up.

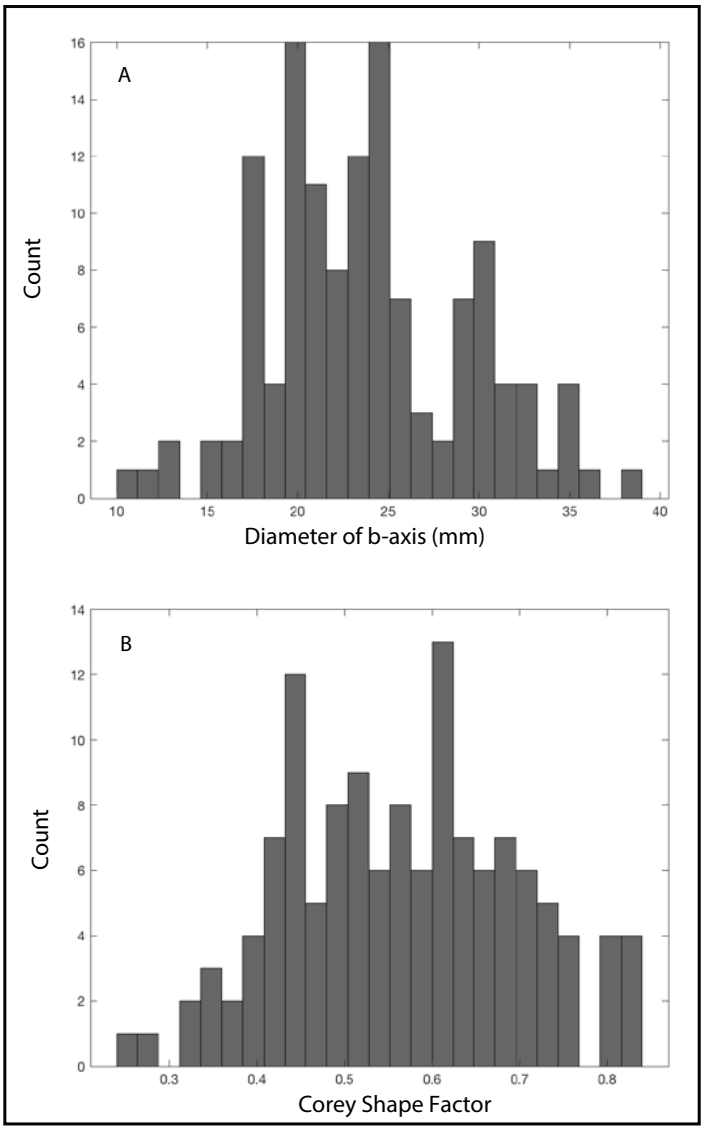

Figure 1.3: (A) Distribution of bed load sediment sizes and (B) Corey Shape Factor. $CSF = c/\sqrt{ab}$, where *a* is the long axis length, *b* is the intermediate axis length *c* is the short axis length.

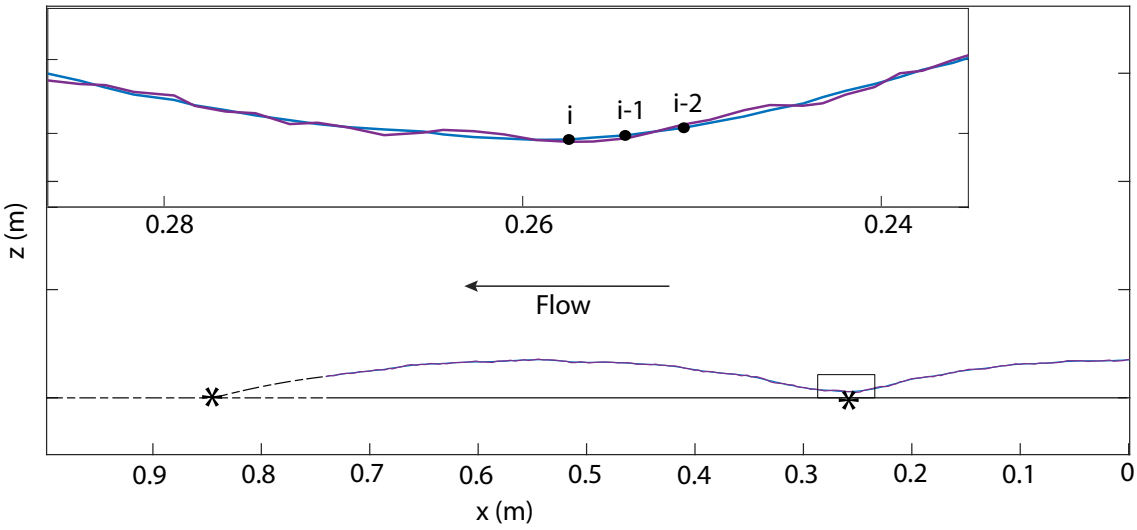

Figure 1.4: Example saltation trajectory captured with high-speed video imaging. The inset shows a zoomed-in view. Purple line is the path of the particle center. The blue line is the smoothed path. The dashed line is the projected path. The open circles show the smoothed path of the particle center over three frames prior to the detected impact point. Asterisks show the estimated point of impact.

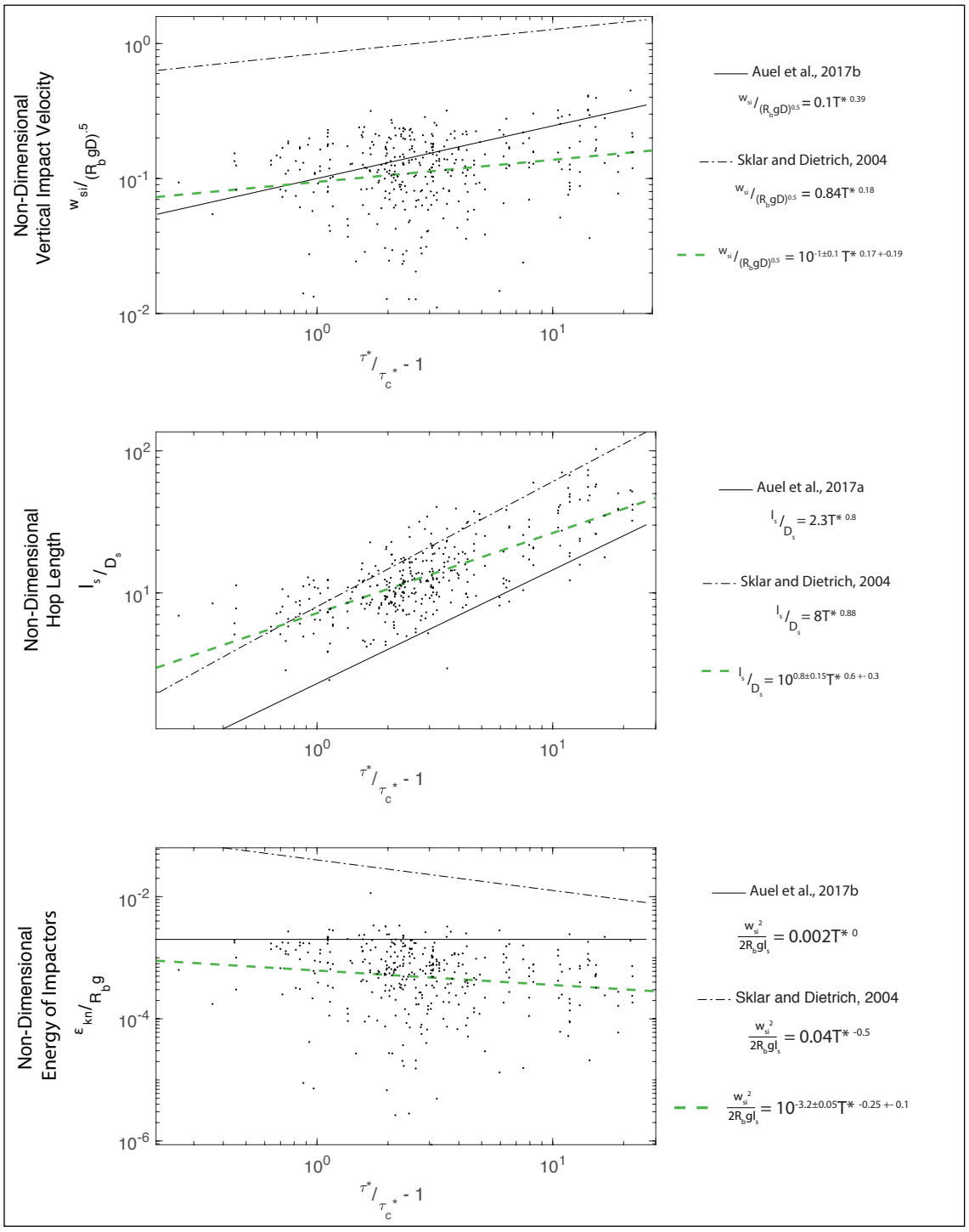

Figure 1.5: Dimensionless forms of vertical impact velocity, hop length, and erosive energy delivered to the planar bed. The green line is fit to a regression of our data. Regressions from previous studies are plotted for comparison (Sklar and Dietrich, 2004; Auel et al., 2017a, 2017b).

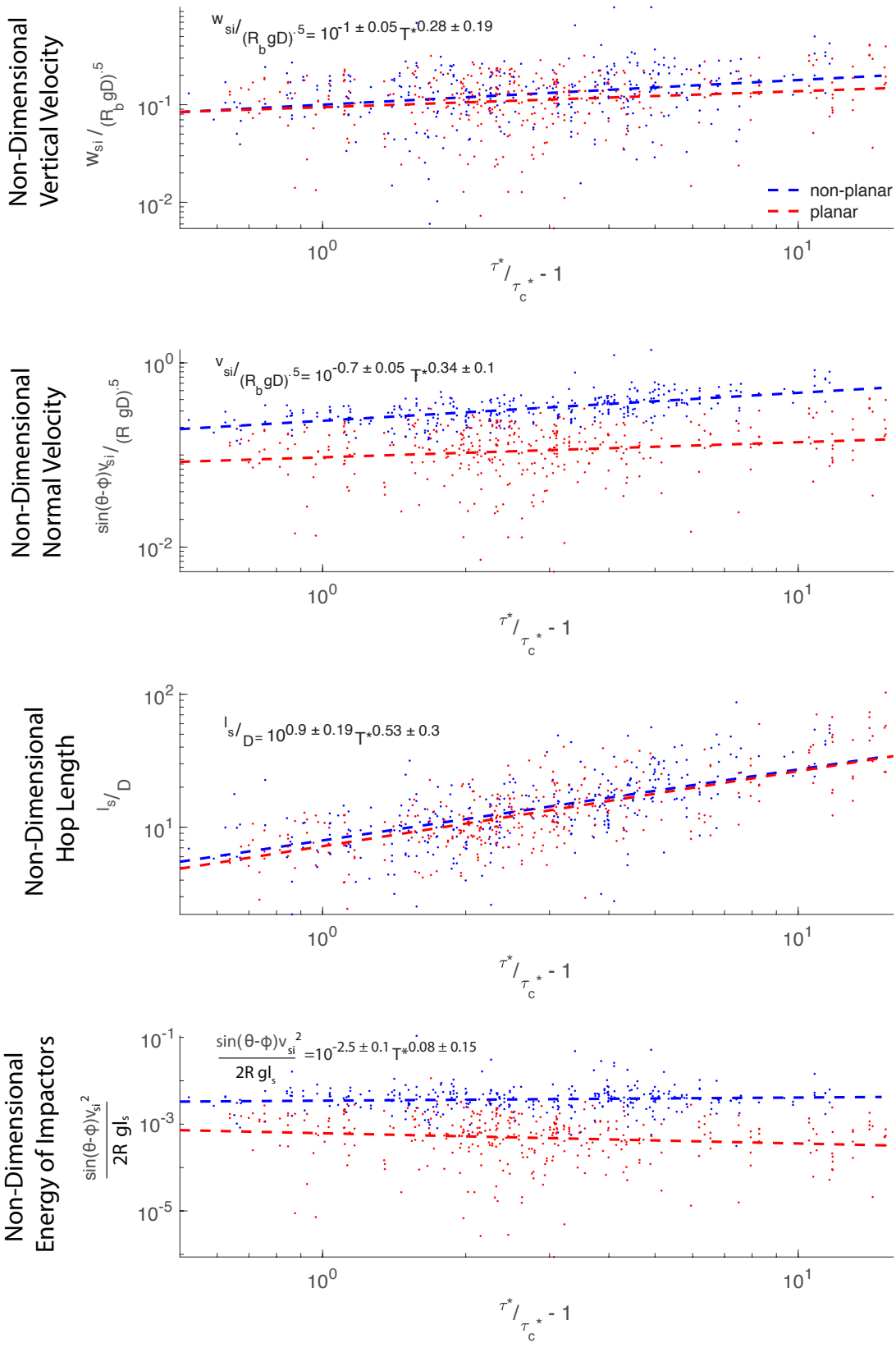
Non-Dimensional Vertical Velocity
$w_{si}/(R_b gD)^{.5} = 10^{-1 \pm 0.05} T^{*0.28 \pm 0.19}$
$w_{si}/(R_b gD)^{.5}$
non-planar
planar
$\tau^*/\tau_c^* - 1$
Non-Dimensional Normal Velocity
$v_{si}/(R_b gD)^{.5} = 10^{-0.7 \pm 0.05} T^{*0.34 \pm 0.1}$
$\sin(\theta-\phi)v_{si}/(R\ gD)^{.5}$
$\tau^*/\tau_c^* - 1$
Non-Dimensional Hop Length
$l_s/D = 10^{0.9 \pm 0.19} T^{*0.53 \pm 0.3}$
l_s/D
$\tau^*/\tau_c^* - 1$
Non-Dimensional Energy of Impactors
$\frac{\sin(\theta-\phi)v_{si}^2}{2R\ gl_s} = 10^{-2.5 \pm 0.1} T^{*0.08 \pm 0.15}$
$\frac{\sin(\theta-\phi)v_{si}^2}{2R\ gl_s}$
$\tau^*/\tau_c^* - 1$

Figure 1.6: Dimensionless forms of vertical impact velocity, diagonal impact velocity, hop length, and the energy delivered to the non-planar bed. Red dots and red trend lines are from planar bed experiments (runs 1 and 2). Blue dots and blue trend lines are from non-planar experiments (runs 3 and 4). Equations in each plot represent the blue dashed line.

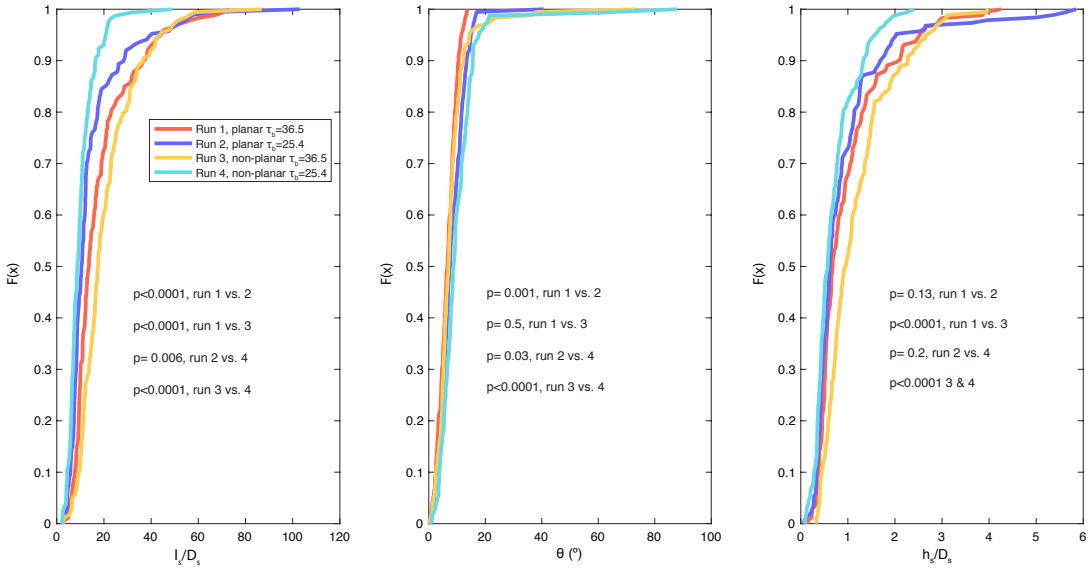

Figure 1.7: Cumulative Distribution Functions of Saltation Components. *F*(*x*) = fraction of total observations <= *x*. Results of Kolmogorov-Smirnov tests are shown. p-values are shown for each test.

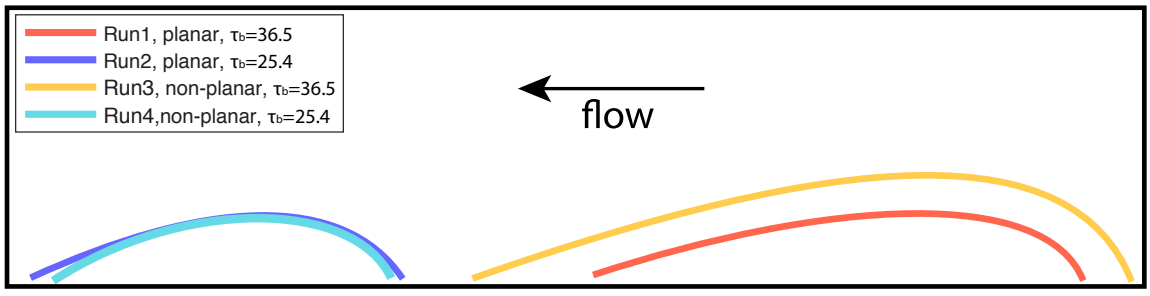

Figure 1.8: Generalized characteristic hop trajectories for each experiment using the relative differences in mean values for each trajectory component (*F(x)*=0.5 in Figure 1.7).

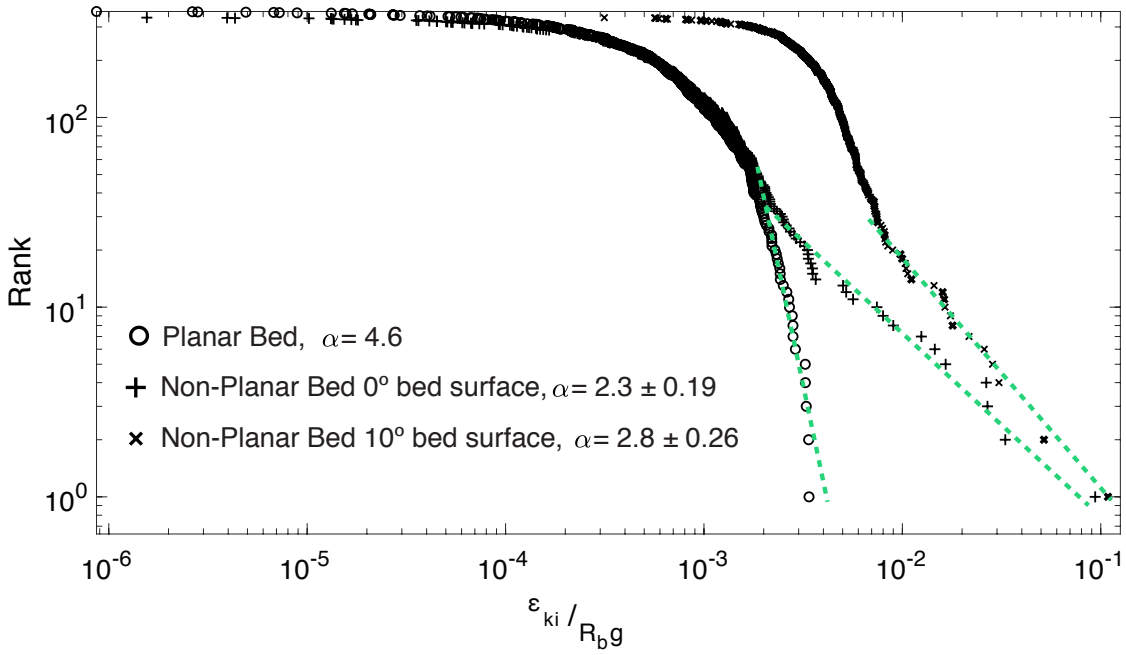

Figure 1.9: Cumulative distributions of ε_{ki}. Power law slopes (α) are fit to the linear portion of data on the right-hand side of the distributions. Rank for each hop is quantified as the number of observed hops with greater impact energy. The most energetic impact would therefore have a rank of 1.

CHAPTER 3: THE INFLUENCE OF EROSION RESISTANCE ON RIVER MORPHOLOGY IN BEDROCK CHANNELS OF CENTTRAL ARIZONA

ABSTRACT

Channel form controls the style and pace of landscape evolution by transmitting the signals of climate and tectonics through the filter of erosion resistance. However, the influence of erosion resistance remains poorly understood. Channel slope and width partly govern the bed shear stress of a stream, and thus the efficiency of bedrock incision and the ability to evacuate sediment from a landscape. We exploit a field setting where channels have experienced a common base level fall history but are composed of various lithologies that display a range of bedrock properties and channel sediment conditions. This natural experiment allows us to determine how channel morphology has been influenced by bedrock detachment and bedrock exposure. For 24 bedrock reaches spanning 10 different rock types we investigate the correlation between channel morphology and erosion resistance factors, which include laboratory measurements of abrasion rate and field measurements of fracture spacing and the size of the 84th percentile sediment in the channel (D_{84}). Our results show that the steady-state channel slope has the strongest correlation with the abrasion resistance factor and D_{84} while the steady-state channel width shows the strongest correlation with fracture spacing and the D_{84} grain size of sediment in the channel. Using multiple-linear regression of all erosion resistance factors provides a robust prediction of morphology. This work suggests strong coupling between bedrock properties and river incision and provides a method to assess the influence of detachment processes and sediment effects on river incision.

INTRODUCTION

Incision into bedrock controls the style and pace of landscape evolution in response to climate and tectonic forcing (Whipple, 2004). The signals of climate and tectonics are transmitted to the landscape through adjustments in channel form (Kirby and Whipple, 2012). However, the erodibility of the river channel modulates the channel form based on factors that limit or enhance the processes of erosion. These factors include the properties of the underlying bedrock that limit detachment of material and the effects of sediment that cover and shield bedrock from erosion. The dominant physical processes of bedrock detachment include abrasion by bed load sediment (Foley, 1980; Sklar and Dietrich, 2004) and hydraulic plucking (Miller, 1991; Whipple et al., 2000; Chatanantavet and Parker, 2009; Lamb and Dietrich, 2009). Rock strength and joint spacing are factors that govern the resistance to abrasion and plucking respectively (Hack, 1957; Selby, 1993; Stock and Montgomery, 1999). Detachment of bedrock is also limited by the ability to transport the coarse sediment load to both expose underlying bedrock and provide tools for erosive processes. Sklar and Dietrich (2006) showed that the threshold for motion is the dominant sediment effect on channel slope. The threshold for sediment motion is primarily a function of sediment size for a given bed shear stress. Understanding what the dominant factors are that limit the processes of bedrock incision and control channel form is a fundamental question in landscape evolution. To address this problem we quantify field–based relations between channel morphology and erosion limiting factors related to rock strength and the mobility of sediment in the channel.

The erosive capacity of a stream is related to the energy exerted on the channel bed by both impacting sediment (abrasion) and hydraulic processes (plucking). In a given channel (i.e. for a

given discharge), the ratio between slope and width partly control the energy exerted on the bed for a given discharge because steep narrow rivers focus faster flow over smaller lateral area. The stream power model posits that the steady-state channel slope adjusts to the erosion resistance of the bedrock channel to achieve the erosion capacity necessary to keep pace with the rate of rock uplift (Whipple and Tucker, 1999). Thus stronger rock will develop steeper slopes (and/or narrower channels) than weaker rock if uplift is spatially invariable. Evidence in the field supports this concept and shows channel slope increases with the intact strength of the rock mass (Duvall et al., 2004; Allen et al., 2013; Marshall and Roering, 2014; Bursztyn et al., 2015). However, the stream power model assumes that erosion is limited only by the rate of detachment of bedrock and neglects the effects of sediment supply and grain size that limit erosion through bed cover. The saltation-abrasion model (Sklar and Dietrich, 2004) accounts for both the erosive and cover effects of sediment transport. Sklar and Dietrich (2006) use the saltation-abrasion model to show that the steady-state bedrock channel slope primarily adjusts to transport the coarse sediment load at the rate bed load is supplied from upstream. Evidence in the field shows that channel slope is sensitive to the size and flux of sediment in the channel (Sklar and Dietrich, 2006; Johnson et al., 2009; Attal et al., 2015; Finnegan et al., 2017; Yanites et al., 2018). However, width adjustment is another way that channels respond to rock erodibility (Montgomery and Gran, 2001; Wohl, 2008; Hancock et al., 2011; Allen et al., 2013; Limaye and Lamb, 2014; Shobe et al., 2017), sediment loading (Finnegan et al., 2005, 2007; Turowski et al., 2007; Yanites and Tucker, 2010), or changing boundary conditions (Stark, 2006; Turowski et al., 2007; Yanites et al., 2010).

The studies above show that many factors related to the erosion efficiency can drive adjustments in channel morphology that control the bed shear stress of the stream (e.g. channel slope and width). However, functional relationships between channel morphology and erosion resistance remain poorly constrained due to complex interactions among the factors involved. Here, we exploit a natural experiment to determine the dominant factors that control channel morphology within the Aqua Fria and Verde River basins of central Arizona, USA. The field setting offers bedrock channels composed of various lithologies that display a range of bedrock properties and channel sediment conditions. Our framework considers the resistance factors to three processes: abrasion, plucking, and sediment mobility, and how well each of the resistance factors (as a single predictor and in multiple regression) explains the variability in channel morphology in a steady-state landscape. Our goal is to determine the relative influences that bedrock detachment processes and bedrock exposure have had on the channel morphology of central Arizona.

FIELD SETTING

Our study area is comprised of tributaries of the Verde River and Aqua Fria Rivers in the Prescott National Forest, Coconino National Forest and the Bradshaw Mountains of central Arizona (Figures 2.1 and 2.2). This landscape is often referred to as the transition zone located between the Colorado Plateau and Basin and Range (Figure 2.1). The recent tectonics of the region are well understood, and faults have not experienced significant activity since the Miocene (Mayer, 1979). Since Miocene age basin filling and volcanic activity, incision has carved through deposits exposing older sedimentary and basement rock. Headward incision of Miocene deposits has propagated to a distinct escarpment within the overlying basalt flow deposits. We focus our

analyses on areas downstream of the escarpment where steady-state conditions are more plausible. Ar^{40}/Ar^{39} dates of lava flows on various Miocene age erosional surfaces perched above modern river valleys along the Mogollon Rim (Figure 2.1) suggest incision rates of 0.05-0.08 mm/yr in the area over the last 5-8 my. (Ott et al., 2018). Due to the monsoon climate of central Arizona riverbeds are easily accessed during the dry season. This allows direct access to measure and sample bedrock channels that actively erode during runoff events (Figure 2.2). The rock types studied here include: Paleozoic age metamorphic and intrusive basement rocks; Mississippian, Permian, and Miocene age sedimentary rock; and Miocene age basalt and volcaniclastic rock (Table 2.1).

METHODS

We attempt to use the properties of bedrock channels to better understand the morphology of a bedrock reach. Here reaches range in downstream distance from 30 to 100 m. We chose reaches with significant bedrock exposure that did not show large variations in channel slope or width. Each reach was limited to one rock type.

Channel Morphology

Downstream changes in slope and width correspond to changes in drainage area and follow hydraulic scaling laws (Leopold and Maddock, 1953; Hack, 1957). Channel slope (*S*) tends to decrease with upstream drainage area (*A*) according to a power law

$$S = k_s A^{-\theta}, \tag{26}$$

where k_s is the channel steepness index, and θ is the channel concavity index (Morisawa, 1962; Flint, 1974). To compare channel steepness across different reaches or basins a reference

concavity is used for the empirical calculation of the normalized channel steepness (k_{sn}) (Wobus et al., 2006)

$$k_{sn} = SA^{\theta_{ref}}. \quad (27)$$

In this study, we measure the channel steepness using χ transformation where we integrate the drainage area along the downstream length of the channel

$$\chi = \int_{x_0}^{x} \left(\frac{A_0}{A(x)}\right)^{\theta_{ref}} dx, \quad (28)$$

where *x* is the longitudinal distance along the stream and A_0 is a reference drainage area, which is set to 1 m^2 throughout this study so that k_{sn} is equal to the change in elevation with the change in χ ($^{dz}/_{d\chi}$) (Harkins et al., 2007; Perron and Royden, 2013; Mudd et al., 2014). This approach reduces the noise introduced by step increases in drainage area with downstream length. Channel width (*W*) tends to increase with upstream drainage area according to a power law

$$W = k_w A^b, \quad (29)$$

where k_w is the wideness index and *b* is typically between 0.3 and 0.5 (Montgomery and Gran, 2001). Using a reference wideness exponent allows comparison of channel width among different reaches and basins with the normalized channel wideness index (k_{wn})

$$k_{wn} = WA^{-b_{ref}}. \quad (30)$$

By removing the effect of increasing drainage area on river slope and width we are able to consider differences in k_{sn} and k_{wn} to be representative of equilibrium channel morphology set by the resistance to erosion processes. Ultimately, the ability of a given river reach to both

detach material from the bed and transport material downstream is a function of the ratio of slope to width. Combining the channel steepness and wideness indices we calculate a normalized stream power index (ω_n)

$$\omega_n = \frac{k_{sn}}{k_{wn}} = \frac{S}{W} A^{\theta_{ref}+b_{ref}}, \quad (31)$$

where a greater ratio between slope and width delivers more energy to a smaller channel bed area. Channel slope and drainage area were calculated from 10m USGS DEMs. Channel width is measured at high flow markers (debris and vegetation scouring) with a handheld range finder at a minimum of three locations at each reach. We used a value of 0.5 for both θ_{ref} and b_{ref} as these are typical values for many rivers.

Erosion Resistance Factors

Abrasion Resistance Factor

In this study we define abrasion as the impact wear of the bedrock surface by bed load particles. The resistance to fluvial abrasion depends on properties of the rock mass and has been shown to correlate with tensile strength, the elastic modulus, and crystalline grain size of the target material (Sklar and Dietrich, 2001; Hobley 2005; Beyeler and Sklar, 2010). In this study we are able to use directly measured abrasion rates on the bedrock samples collected from field sites. In chapter two we performed experiments in a large-scale sediment flume. Here, we present the abrasion rates (A_r) measured over those experiments and derive the abrasion resistance factor (ε_v) from those results using the energy of sediment impacts on the bed (ε_{kt}) (Sklar and Dietrich, 2004)

$$A_r = \frac{\varepsilon_{kt}}{\varepsilon_v}, \quad (32)$$

where A_r is the vertical incision rate with units of length per time, ε_{kt} subsumes the volume eroded per impact as well as the impact rate and has units of mass per time cubed, and ε_v is equivalent to the energy necessary to erode a unit volume of material through elastic deformation wear and has units of stress (Engel, 1978). Note that bed cover was not a factor in the experiments and is thus neglected in equation 32. In chapter two we calibrated the relation between energy delivered to a planar bed and excess shear stress as

$$\varepsilon_{kt} = 10^{-3.2} T*^{-0.25} R_b g q_s. \quad (33)$$

where R_b is the dimensionless buoyant density of sediment ($\rho_s/\rho_w - 1$= 1.65, where ρ_s is the density of sediment), g is gravity, and q_s is the mass flux of sediment per unit length and time (throughout experiments q_s was held at 0.15 kg/ms). Using equations 32 and 33 we calculate ε_v over two experiments and average the values. Using the conditions of runs 1 and 2 (described in chapter two) we continuously ran sediment through the flume at rate of 0.15 kg/s and measured the mass loss after 75 hr and 50 hr for runs 1 and 2 respectively.

Rock samples were collected from bedrock channels in the Verde and Aqua Fria Rivers of central Arizona. They comprise various lithologies including: Paleozoic Age metamorphic and igneous basement rock, Mississippian to Miocene age sedimentary rock, and Miocene age basalt and volcaniclastic rock. Discs for our erosion experiments were cut from 15 cm diameter cores at a depth of 5 – 10 cm below the channel surface. Performing the experiments on fresh rock from depth avoids surface degradation due to the physical and chemical weathering of the bedrock. Erosion rates were determined by removing the discs from the flume floor and measuring the mass loss using an electronic scale with maximum weight= 8.1 kg and precision= 0.01 g. The

mass loss rate was converted to vertical incision rate using the density of each rock type and the surface area of discs. The density of each rock type was measured using the mass and volume displacement of ~1 cm cubes of each sample.

Fracture Spacing

In general, hydraulic plucking is a more efficient detachment process than abrasion but is limited to infrequent and extreme events especially in wider spaced fracture sets. The entrainment of fractured blocks of bedrock (hydraulic plucking) depends on the size of jointed blocks of bedrock, the orientation of fracture sets, and the protrusion of blocks into the flow (Lamb and Dietrich, 2009). However, entrainment only partially accounts for the efficiency of hydraulic plucking because the river must then transport the plucked blocks downstream to prevent alluviation and enable erosion (Lamb et al., 2015) adding additional importance to the size of jointed blocks. We quantify a potential efficiency of hydraulic plucking as the average fracture spacing of the channel bed over three separate 1 m^2 areas. Fracture spacing was measured in the field by placing a measuring tape on the bedrock floor of the channel and counting the number of fractures that intersect the measuring tape over a distance of 1 meter. The tape was then rotated 90° to get a fracture count in the perpendicular direction. The fracture spacing (f_s) of each survey was determined as 2 divided by the total fracture count over both transects, and the fracture spacing of the reach was determined by averaging three surveys.

Sediment Mobility

Sediment mobility limits abrasion and plucking by controlling the available tools for erosion and by covering the bed with alluvium. Sediment supplied to the channel provides the tools that

abrade exposed bedrock (the 'tools effect'), but can inhibit incision by burying the bed in alluvium and reducing the amount of exposed bedrock (the 'cover effect'). Bedrock exposure is a function of the ratio of transport capacity to sediment supply (Sklar and Dietrich, 2004). Transport capacity is a function of bed shear stress in excess of the shear stress necessary to mobilize a particle of a particular grain size (Fernandez Luque and Van Beek, 1976), thus larger grain sizes require more shear stress to mobilize than smaller grain sizes. Lacking a robust method to quantify the sediment supply rate to channels we focus on sediment mobility through the grain size dependence on the threshold for motion. Note that this consideration of sediment effects based on grain size alone requires an assumption that spatial variability in the flux of sediment to the channel is negligible and that bedrock exposure is primarily a response to the mobility of sediment. Here, we use the large sediment size fraction, D_{84} (84^{th} percentile of the distribution of sediment sizes in the channel) as a proxy for the resistance to sediment mobility. Larger, more immobile sediment in the channel decreases erodibility by (1) reducing the available shear stress to the bed through form drag on immobile obstacles and by (2) reducing the transport of material out of a reach relative to the rate supplied to the reach thereby covering the bed. Grain size was measured along the intermediate axis length and estimated for large boulders where the intermediate axis was not accessible. We measured 100 intermediate axis lengths (Wolman, 1954) at each reach by picking the at each 10 cm interval along a measuring tape oriented in the cross stream direction.

RESULTS

Our results focus on the correlations between three metrics of channel morphology (channel steepness index (k_{sn}), channel wideness index (k_{wn}), and stream power index (ω_n)) and three

metrics of erosion resistance (abrasion resistance factor (ε_v), fracture spacing (f_s), and the size of the coarse fraction of sediment in the channel (D_{84}). This dataset includes 24 separate reaches of bedrock channels in central Arizona that vary among ten different rock types.

Channel Morphology

The k_{sn} values (normalized channel steepness index) of the studied reaches range between 45 and 250 m and vary as much as 2–fold for a single rock type (Table 2.1). The k_{wn} values (normalized channel wideness index) range between 0.0009 and 0.0037 and vary as much as 2.6-fold for a single rock type (Table 2.1). The ω_n values (normalized stream power index) range over two orders of magnitude from 7.91×10^3 to 1.58×10^5 m. Figure 2.3 shows plots of elevation with χ for each reach, the slope of which is k_{sn}. These χ-plots show the location of contacts along the streams, and in general changes in steepness often coincide with changes in lithology implying that lithologic properties play some part in channel morphology. Note that we did not survey channels along the entirety of each lithologic reach, so while the steepness is quantifiable along the entire river segment we only measured channel width at locations marked with an asterisk in figure 2.3.

Resistance Factors to Channel Incision Processes

Abrasion Resistance Factor

The abrasion resistance factor, ε_v, is related to the energy required to detach a unit volume of rock and was measured in laboratory experiments for each rock type in this study. The regression of ε_v with k_{sn} shows that channel slope increases with the resistance to abrasion, but ε_v can only explain 14% of the variability in channel steepness indices across all of the studied

reaches (Figure 2.4A). The variability of ε_v with k_{wn} is so large that the regression does not suggest any relation between resistance to abrasion and channel width (Figure 2.4B). The regression of ε_v with ω_n suggests a regression slope similar to that of ε_v vs. k_{sn}, but the scatter is large (Figure 2.4C). While each sample of a specific rock type on which ε_v was calculated comes from an individual reach we assume that the resistance factor is applicable to other reaches of the same rock type. We recognize that inconsistencies exist in bedrock and that a sample from one location may not be representative of the integrity of that lithology throughout a landscape. In figure 2.4 the reach from which the sample taken to measure the abrasion resistance factor is marked by a solid dot while the reaches in which ε_v is assumed are marked with an open circle. If we only consider the reaches that correspond to the measured abrasion resistance factor (solid dots), the R squared goodness-of-fit of ε_v vs. k_{sn} increases from 0.14 to 0.4 but does not significantly improve for ε_v vs. k_{wn} or ε_v vs. ω_n (Figure 2.4). Overall, resistance to abrasion is a strong single predictor of channel slope for the channels where samples for abrasion experiments were collected, but shows no evidence of being a strong control on channel width adjustment.

Fracture Spacing

The mean fracture spacing (f_s) of the channel floor is related to the efficiency of hydraulic plucking. The regression of f_s with k_{sn} shows weak correlation and does not suggest any relation between fracture spacing with channel slope (Figure 2.5A). Fracture spacing is the strongest predictor of k_{wn} (Figure 2.5B). The regression suggests that channels narrow as fracture spacing increases, but can only explain 21% of the variability. This inverse trend confirms findings of other studies that show wider channels form in more densely fractured bedrock (Whipple et al.,

2000) and abrasion dominated channels in widely spaced fractured rock form narrow channels (Wohl, 2008; Johnson and Finnegan, 2015a). Despite the high degree of variability between f_s and ω_n, the regression shows the expected positive relation suggesting that the stream power of a channel increases with resistance to plucking (Figure 2.5C). Of the resistance factors considered here, fracture spacing is the strongest single predictor of channel width, and shows no evidence of being a strong control on channel slope adjustment.

Sediment Mobility

The D_{84} grain size represents the fraction of large sediment in the channel and is related to the resistance to detachment processes. As sediment size increases the shear stress of the threshold of motion increases which means that for equilibrium to occur over long timescales the channel slope must steepen to transport larger grains. Grains that are significantly large compared to the surface roughness of the surrounding bed can reduce the available shear stress due to form drag on immobile sediment in the channel. This may only be a factor for a few of the reaches with the largest D_{84} (>300 mm) and during below-threshold runoff events when these grains are immobile. D_{84} has the most robust correlation with k_{sn} of any single resistance factor considered in this study (Figure 2.6A) and accounts for 41% of the variability in channel steepness index. The regression of D_{84} with k_{wn} shows an inverse correlation (Figure 2.6B) with a regression slope similar to that of f_s vs. k_{wn}. The D_{84} also shows the most robust correlation with ω_n of any single resistance factor considered in this study and explains 45% of the variability in stream power index (Figure 2.6C). Of the resistance factors considered here, the size of sediment in the channel is a relatively strong single predictor of both channel slope and channel width.

Multiple-Regression Model

Combining the data from all survey reaches and applying the rock type specific ε_v to reaches of the same rock type, we use multiple linear regression to find that stream power index (ω_n) is predicted as a power function of ε_v, f_s, and D^{84} (R^2=0.62)

$$\omega_n = 10^{3.95(\pm 1)} \epsilon_v^{0.39(\pm 0.12)} f_s^{0.28(\pm 0.23)} D_{84}^{0.5(\pm 0.28)} \quad (34)$$

where the best-fit exponents include the $\pm$ error estimate of the 95% confidence interval. The multiple-regression model explains 62% of the variability in stream power index. Figure 2.7 plots the predicted stream power index (equation 34) with the observed stream power index of each reach. While equation 34 is calibrated only for ephemeral bedrock channels of central Arizona this framework suggests that channel morphology is a strong function of both resistance to detachment processes and the size of sediment delivered to the rivers.

We quantify the relative importance of these factors for predicting channel morphology by measuring the change in R^2 as we remove a parameter from the regression. The change in R^2 represents the percentage of variance that the removed parameter explains that the other combined parameters could not. Adding ε_v, f_s, and D_{84} to the model explains 22%, 16%, and 18% of the variability in stream power index respectively. These percentages suggest a more or less equal importance of each erosion process resistance factor.

A number of other rock mass properties were measured for each rock type. The measurement methods and values are reported in the appendix. These properties include porosity, density, slake durability, uniaxial tensile strength, uniaxial compressive strength, elastic modulus, p-wave

speed, a damage parameter, and mean crystalline grain size. However, none of these rock properties significantly improved the R^2 value of the multiple-regression model either by substitution for abrasion resistance (as an alternate measure of rock mass strength) or through adding additional predictors to the model. The inability for these various geotechnical metrics to improve the model accuracy suggests that simulated abrasion experiments provide the most robust measurement of the resistance to abrasion.

DISCUSSION

The slope and width of the bedrock channels that we studied in central Arizona are sensitive to the abrasion resistance coefficient of the rock type, the mean fracture spacing of the bedrock channel reach, and the D_{84} grain size of sediment in the channel. As a single predictor, D_{84} describes both channel slope and width better than ε_v or f_s suggesting that the effects of sediment mobility may overprint the effects of bedrock erodibility even in bedrock channel systems. This finding is consistent with the saltation-abrasion model that predicts the threshold of motion is the most important sediment effect and abrasion is the least important sediment effect on channel slope (Sklar and Dietrich, 2006). However, when all three process resistance factors are considered in a multiple regression the correlation significantly improves and each parameter has a similar contribution in explaining both the slope and width in the stream power index. The hydraulic roughness of a channel is a first order control on the local flow velocity, bed shear stress, and near bed turbulence; and thus, the energy of bed load impacts as well as the sediment transport dynamics of a stream. Lacking robust measurements of local bedrock channel topography we were not able to consider the influence of roughness, but we

acknowledge that the roughness of channel beds and walls may account for a significant portion of the variability in channel slope and width.

Results show that channel slope has the strongest correlation with abrasion resistance (ε_v) and sediment size (D_{84}) while channel width has the strongest correlation with fracture spacing (f_s). Channel slope may be less sensitive to fracture spacing because along the channel floor abrasion tends to wear bedrock to an even surface. In the absence of knickpoints or vertical ledges that provide a free surface, abrasion of the bedrock floor may limit the streams ability to topple, slide, or vertically entrain blocks. Therefore, while the propagation of knickpoints, and thus the timescale of landscape response to perturbations in climate and tectonics, may be strongly dependent on fracture spacing, the steady state channel slope is less dependent on fracture spacing. On the other hand, channel width may not be sensitive to ε_v because abrasion by bed load sediment is more rare along channel margins, whereas f_s is a dominant factor because longer periods of weathering are able to prepare blocks and free vertical surfaces of the channel walls allow for toppling or sliding of blocks into the channel.

The Influence of Layered Stratigraphy

We have shown that bedrock erodibility and the size of sediment in the channel can modulate the stream power index. Additionally, the dip of the contact between rock layers can also affect the incision rate and morphology of a reach (Howard, 1988; Forte et al., 2016; Perne et al., 2017). For non-vertical contacts, the location of the contact between adjacent rock units migrates laterally as a river incises vertically. If adjacent rock units differ in erodibility then contacts migrate at different rates. This effectively shrinks or stretches the lateral extent of the

lithologic reach causing disequilibrium between topography, erodibility, and uplift rate. In addition to the erodibility of adjacent units the spatial extent of disequilibrium also depends on the distance from base level, the thickness of the lithologic unit, the dependence of erosion physics on channel slope, and the direction of contact migration (upstream or downstream). A consideration of all of these factors is beyond what is capable with the available data in this study. As a simple test to determine if lithologic contact dip causes significant disequilibrium in our studied reaches, we can use our multiple-regression model to identify any instances in which a more resistant lithology (determined from equation 34) has a lower stream power index than an adjacent less resistant lithology. In only two cases, where we have surveyed adjacent reaches, the less resistant rock is steeper than the more resistant rock: (1) Gn145 overlying PH17 and (2) PH141 overlying GN142 (Figure 2.7). Although the overall resistance to erosion factors (predicted by equation 34) of the greenstone reaches are only slightly greater than the adjacent phyllite reaches, the k_{sn} values of the phyllite reaches are greater. This provides evidence that contact migration may play a role in channel morphology in these reaches. For the most part however, less erodible reaches are steeper than more erodible reaches suggesting that either (1) contact dip is not close enough to horizontal to have a significant effect on lateral contact migration or (2) that the erosion physics of the other rock types does not allow for steeper slopes to be maintained in weaker units or a combination of both scenarios.

The Influence of Sediment Strength

The strength of bed load sediment also has an effect on the erodibility of bedrock. Harder bed load grains impacting a softer bed have the ability to indent and scratch the surface resulting in greater erosion per impact (Wilson and Lavé, 2014). The abrasion resistance factors for the rock

types in this study were calculated from experiments using predominantly hard granitic bed load clasts. In these studied reaches, for most part the sediment in the channel is near the same hardness or harder than the bedrock (using the abrasion resistance factor as an indication of the strength of sediment sourced from upstream drainages). Therefore, the calculated abrasion resistance factor is likely a good characterization. However, for the two basalt reaches a large percentage of the sediment supplied from upstream is made of weaker sandstone. While weaker particles are capable of eroding harder target material (Dietrich, 1977), it is unclear to the extent that erosion is limited, but this may in part explain why both basalt reaches are steeper than predicted with the multiple-regression model.

Implications for Future Work on Erodibility and Landscape Evolution

We demonstrate a method to calibrate the erodibility of bedrock in the field that can guide millennial-timescale bedrock incision models and interpretation of channel morphology in response to external forcing in basins with variable lithology. Applying these methods to a landscape with robust constraints on sediment supplied to the channels would likely provide further insight on the influence of hillslope processes on channel erodibility and may explain some of the remaining variability in stream power indices measured here. Moving forward, a more complete understanding of how bedrock erodibility develops over longer timescales could provide deeper insights on the influence of tectonics and climate on landscape evolution. It can be argued that all of the processes considered in this paper (abrasion, plucking, and sediment mobility) depend on the density of fractures at the micro and macro scales. At the granular scale abrasion of rock occurs through the intersection of microscopic cracks (Finnie, 1960; Bitter, 1963a) and thus the density of cracks will determine the efficiency of abrasion. In bedrock

landscapes the size of sediment delivered to the channel reflects the bedrock fracture density (Sklar et al., 2017). Thus, focusing landscape erodibility on the development of fractures in response to the effects of climate driven weathering (e.g. Eppes and Keanini, 2017; Eppes et al., 2018), tectonic deformation (e.g. Molnar et al., 2007), and topographic stresses (e.g. Molnar, 2004; Clair et al., 2015) could account for resistance to erosion through both detachment processes and sediment effects.

CONCLUSIONS

Overall, the available field data explains differences in the stream power of the studied reaches, but topographic disequilibrium and the ratio of hardness between bed load sediment and bedrock may account for some of the remaining variability. Correlations between channel morphology and factors related to erosion resistance show that channel width is more difficult to predict than channel slope. Channel slope is more strongly correlated to abrasion resistance and sediment size in the channel, but not to fracture density. Channel width is more strongly correlated to fracture density and sediment size in the channel, but not to abrasion resistance. Combining all of the erosion resistance factors in a multiple linear regression model predicts stream power index of most reaches in this study well. The regression model shows that across variable rock types and sediment loading conditions the influences of abrasion, plucking, and sediment mobility have similar importance in setting the slope and width of steady-state channel morphology. While these results are specific to streams of central Arizona this work provides a method for assessing erodibility controls on bedrock incision and topography and for incorporating bedrock properties into landscape evolution models.

Table 2.1: Channel Morphology and Erosion Resistance Data

Table 2: Channel Morphology and Erosion Resistance Factors

Lithology	Reach Name	Basin	Upstream Coordinate		Downstream Coordinate		k_{sn} (m)	k_{wn}	ω_n (m)	ε_v (kg/ms^2)	D_{84} (m)	F (m)	A (km^2)
			Easting (m)	Northing (m)	Easting (m)	Northing (m)							
Granodiorite	gd_{106}	Lower Bumblebee	392622	3784000	392371	3783834	189	0.0013	1.45E+05	*1.93E+07	200	0.037	96.93
Greenstone	gn_{145}	Mule canyon	377087	3804826	377627	3804295	129	0.0019	6.79E+04	*4.18E+06	127.8	0.018	12.34
Greenstone	gn_{53}	Sycamore	389212	3780783	389279	3780234	98	0.0017	5.76E+04	4.18E+06	50.8	0.013	6.6963
Greenstone	gn_{142}	Mule canyon	381056	3799663	381208	3799521	124	0.0019	6.53E+04	4.18E+06	183.8	0.015	45.36
Phyllite	ph_{147}	Middleton	383334	3793155	384940	3793089	123	0.0029	4.24E+04	*3.05E+06	184	0.036	16.224
Phyllite	ph_{143}	Mule canyon	380270	3803462	380175	3803320	101	0.0014	7.21E+04	3.05E+06	64	0.048	5.1916
Phyllite	ph_{17}	Mule canyon	377987	3804068	378139	3804068	144	0.0027	5.33E+04	3.05E+06	170.4	0.027	14.902
Phyllite	ph_{141}	Mule canyon	380459	3801387	380478	3801094	160	0.0028	5.71E+04	3.05E+06	183.8	0.018	38.293
Granite	gr_{151}	Middleton	385148	3792914	385272	3792800	188	0.0016	1.18E+05	5.74E+06	99.12	0.100	18.873
Granite	gr_{1}	Middleton	380137	3791015	380289	3791043	187	0.0008	2.34E+05	*5.74E+06	100	0.053	2.1733
Granite	gr_{30}	Buckhorn	366920	3775315	366996	3775068	137	0.0015	9.13E+04	5.74E+06	170	0.056	15.482
Granite	gr_{138}	Mule canyon	380213	3802335	380365	3802306	203	0.002	1.02E+05	5.74E+06	183.8	0.042	29.862
Volcaniclastic	vc_{61}	Upper Bumblebee	393456	3795974	393546	3795770	66	0.0029	2.28E+04	*438000	65	0.333	19.694
Miocene Sandstone	mc_{115}	Mexican Tank	389501	3870719	389393	3870398	45	0.0029	1.55E+04	*8.87E+05	57.6	0.018	2.5355
Miocene Sandstone	mc_{36}	West Oak Creek	414672	3857553	414813	3856389	92	0.0011	8.36E+04	8.87E+05	100	0.083	85.75
Vesicular Baslat	vb_{112}	Mexican Tank	389600	3871407	389572	3871303	81	0.0027	3.00E+04	*1.66E+06	306.2	0.091	2.1429
Permian Sandstone	ps_{134}	May Tank	388226	3874334	387872	3874329	170	0.0012	1.42E+05	*6.11E+05	400	0.333	67.319
Mississippian Sandstone	ms_{110}	May Tank	387490	3869620	387405	3869375	158	0.0018	8.78E+04	*1.64E+06	312.6	0.250	72.35
Mississippian Sandstone	ms_{34}	West Oak Creek	415264	3859637	415245	3859140	160	0.0012	1.33E+05	1.64E+06	852	0.053	43.19
Mississippian Sandstone	ms_{137}	May Tank	385263	3867516	385235	3867308	157	0.0012	1.31E+05	1.64E+06	300	0.167	75.988
Mississippian Sandstone	ms_{45}	Wet Beaver	437444	3838346	437435	3838215	141	0.0027	5.22E+04	1.64E+06	169.6	0.200	6.6079
Mississippian Sandstone	ms_{50}	Wet Beaver	436581	3837661	436346	3837698	239	0.0031	7.71E+04	1.64E+06	500	0.125	295.98
Miocene Basalt	bs_{111}	Bull Tank	389273	3867676	389113	3867119	192	0.001	1.92E+05	*4.33E+06	153.2	0.059	46.61
Miocene Basalt	bs_{128}	West Oak Creek	415658	3855760	415658	3855187	121	0.0026	4.65E+04	4.33E+06	102.16	0.043	92.633

*-Denotes the reach from which the bedrock sample was extracted for abrasion experiments. UTM Zone 12N

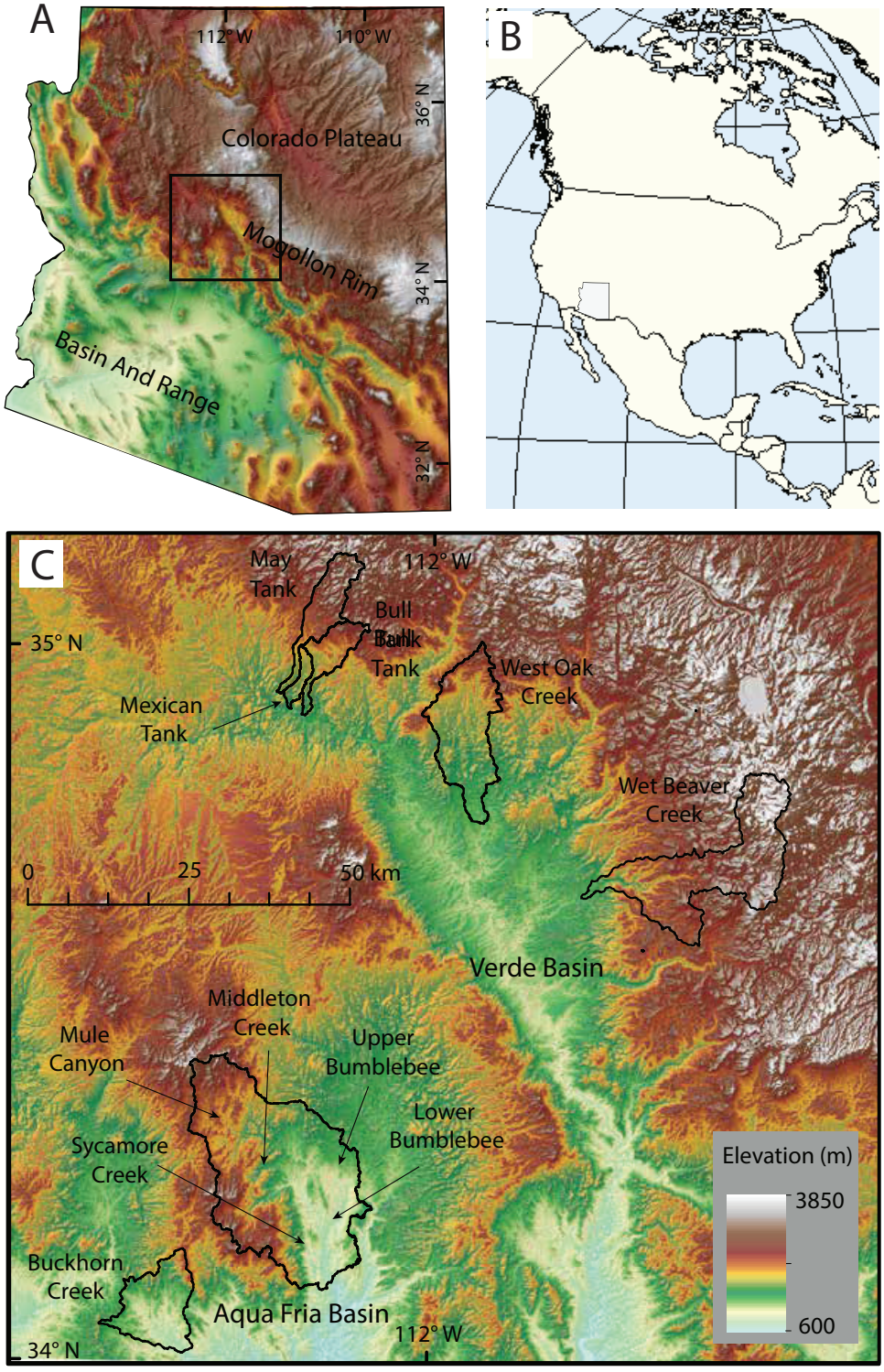
A
112° W
110° W
36° N
34° N
32° N
Colorado Plateau
Mogollon Rim
Basin And Range
B
C
May Tank
112° W
Bull Tank
35° N
West Oak Creek
Mexican Tank
Wet Beaver Creek
0
25
50 km
Verde Basin
Middleton Creek
Mule Canyon
Upper Bumblebee
Lower Bumblebee
Sycamore Creek
Elevation (m)
3850
600
Buckhorn Creek
Aqua Fria Basin
112° W
34° N

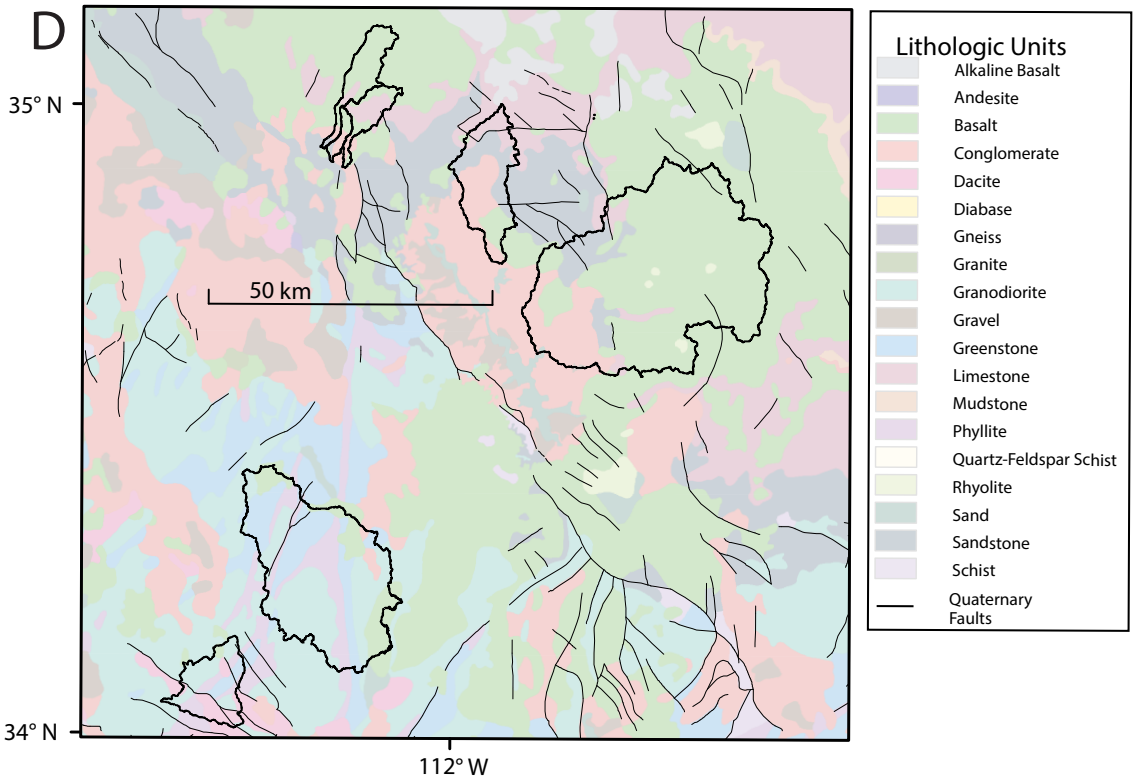

Figure 2.1: Study Area. (A) The state of Arizona, USA. (B) The continent of North America. (C) Studied basins shown in the box in A. (D) Geologic map of the box area shown in the box in A.

Figure2.2: Examples of Bedrock Reaches

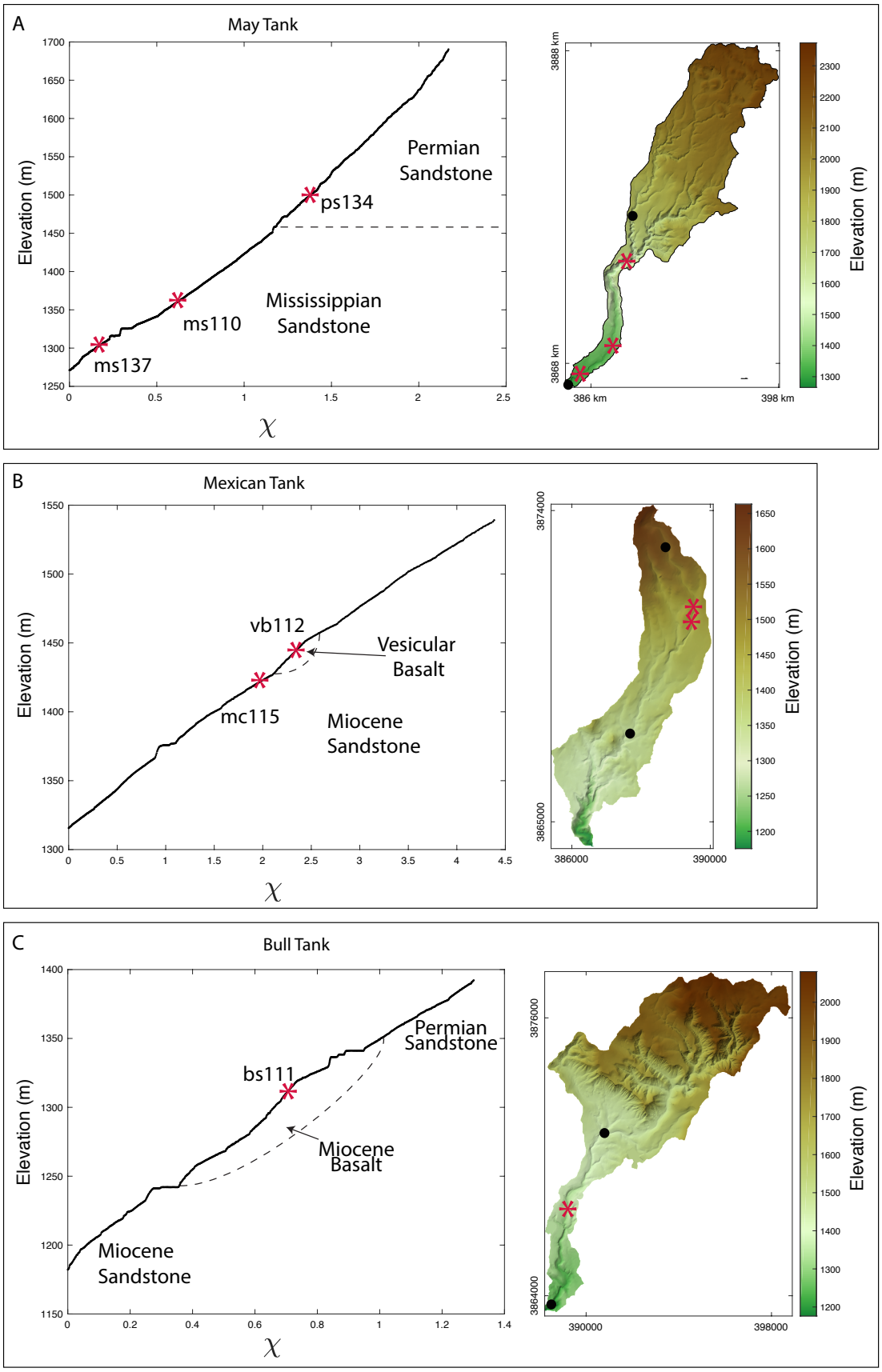
A
May Tank
Elevation (m)
Permian
Sandstone
ps134
Mississippian
Sandstone
ms110
ms137
χ
3888 km
3868 km
386 km
398 km
Elevation (m)
B
Mexican Tank
Elevation (m)
vb112
Vesicular
Basalt
mc115
Miocene
Sandstone
χ
3874000
3865000
386000
390000
Elevation (m)
C
Bull Tank
Elevation (m)
Permian
Sandstone
bs111
Miocene
Basalt
Miocene
Sandstone
χ
3876000
3864000
390000
398000
Elevation (m)

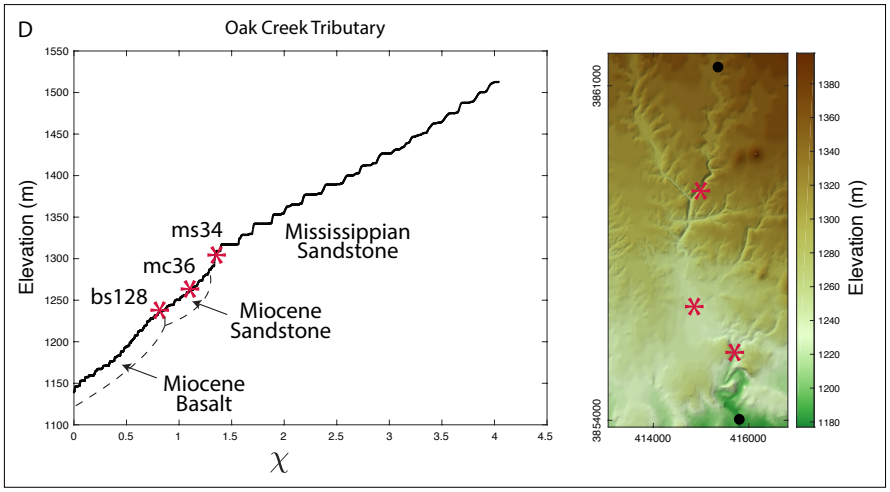
D
Oak Creek Tributary
Elevation (m)
χ
ms34
mc36
bs128
Mississippian
Sandstone
Miocene
Sandstone
Miocene
Basalt
Elevation (m)

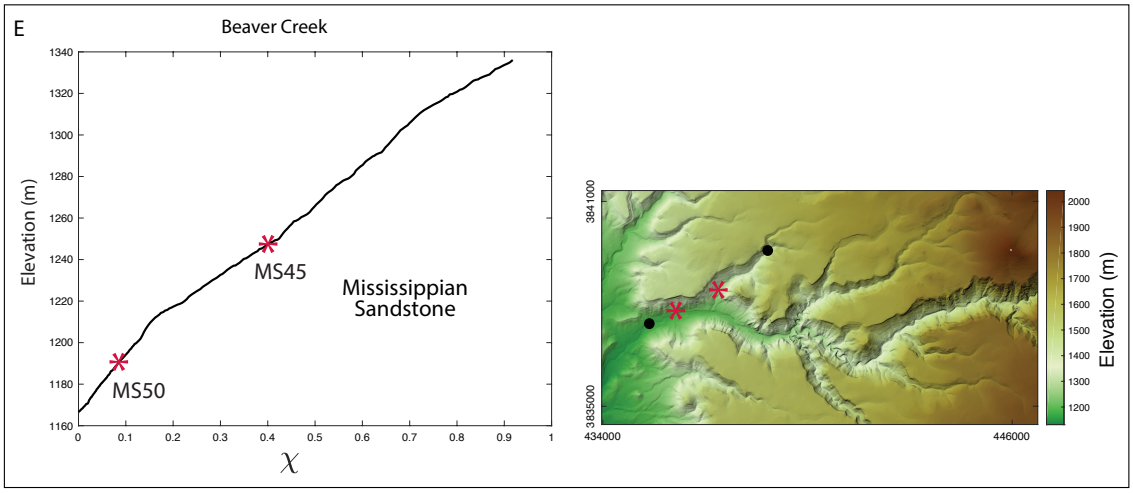
E
Beaver Creek
Elevation (m)
χ
MS45
MS50
Mississippian
Sandstone
Elevation (m)

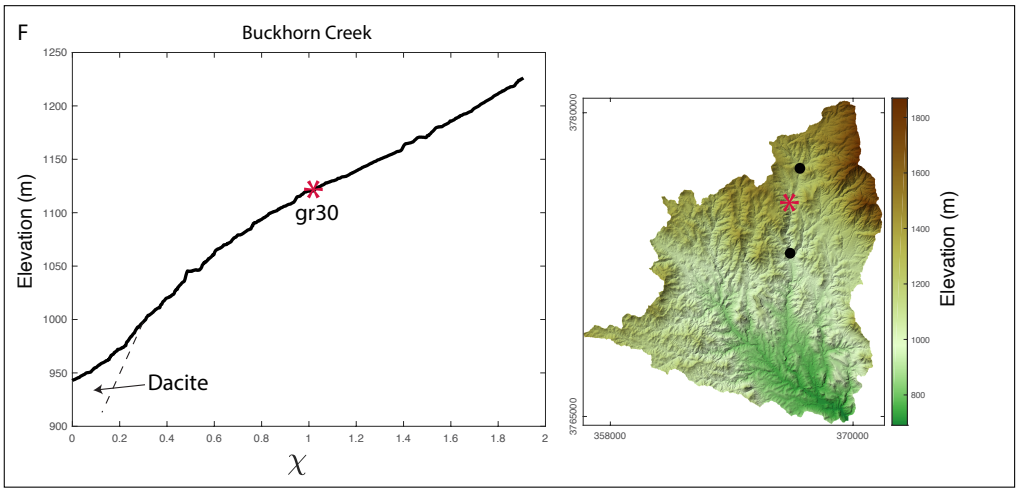
F
Buckhorn Creek
Elevation (m)
χ
gr30
Dacite
Elevation (m)

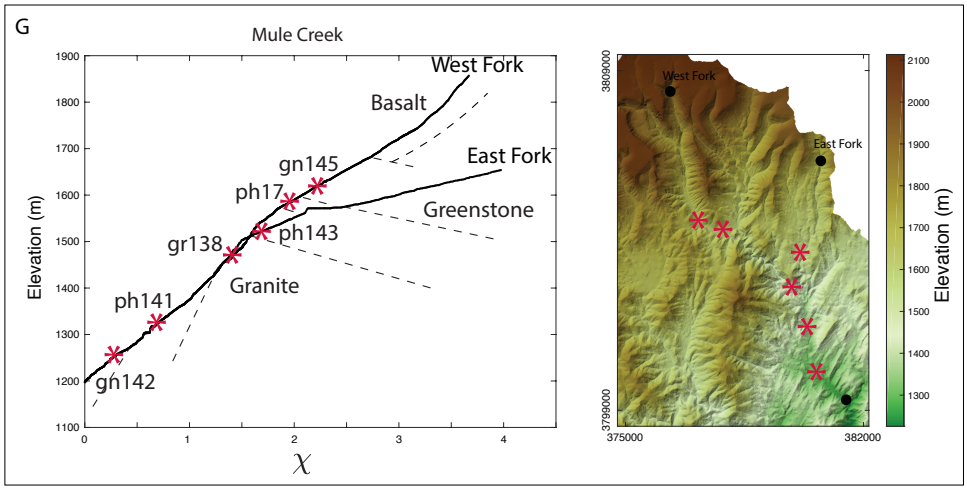
G
Mule Creek
West Fork
Basalt
East Fork
gn145
ph17
Greenstone
ph143
gr138
Granite
ph141
gn142
Elevation (m)
χ
West Fork
East Fork
Elevation (m)

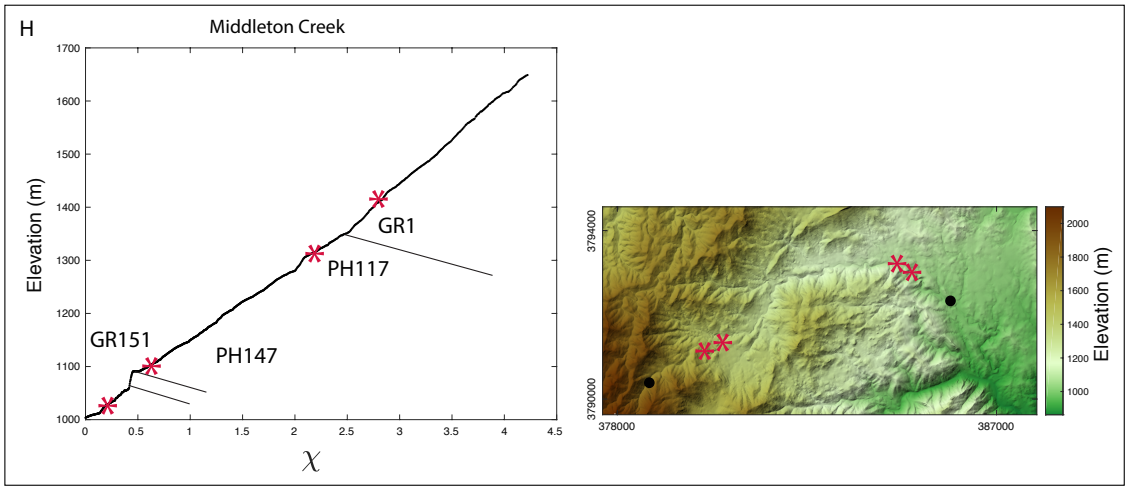
H
Middleton Creek
GR1
PH117
GR151
PH147
Elevation (m)
χ
Elevation (m)

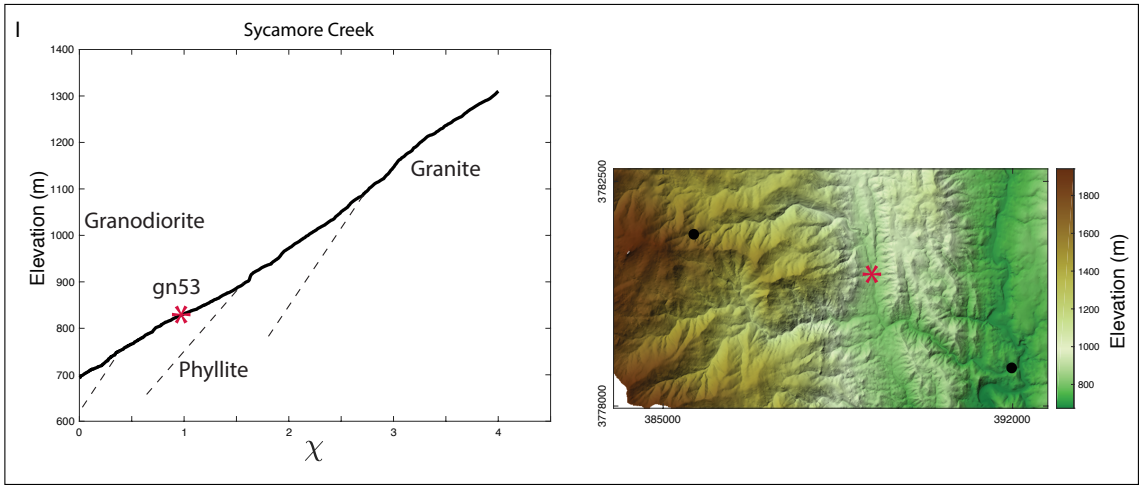
I
Sycamore Creek
Granite
Granodiorite
gn53
Phyllite
Elevation (m)
χ
Elevation (m)

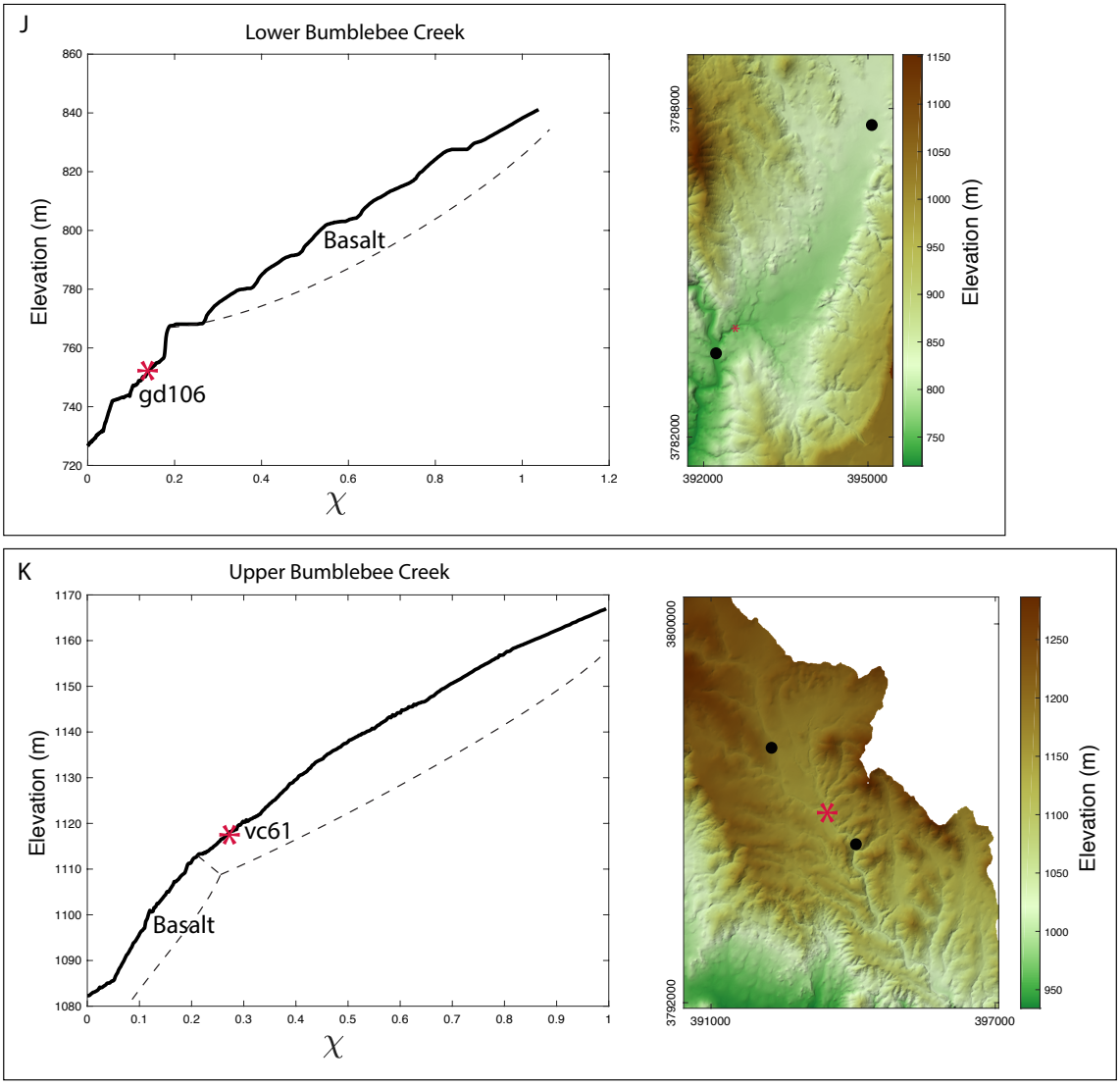

Figure2.3: χ-plots and elevation maps of the studied reaches. Locations of field surveys are marked with a red asterisk and the reach name. Boundaries between lithologic units are marked with vertical lines. Black dots on map figures mark the downstream and upstream end points of the χ-plots. The dashed lines in the χ-plots represent best guesses of lithologic boundaries in cross section. Note that the plots are in χ-space and that dip angles are only meant to show the relative direction of dip to the flow of the river (i.e. downstream, upstream, or horizontal.

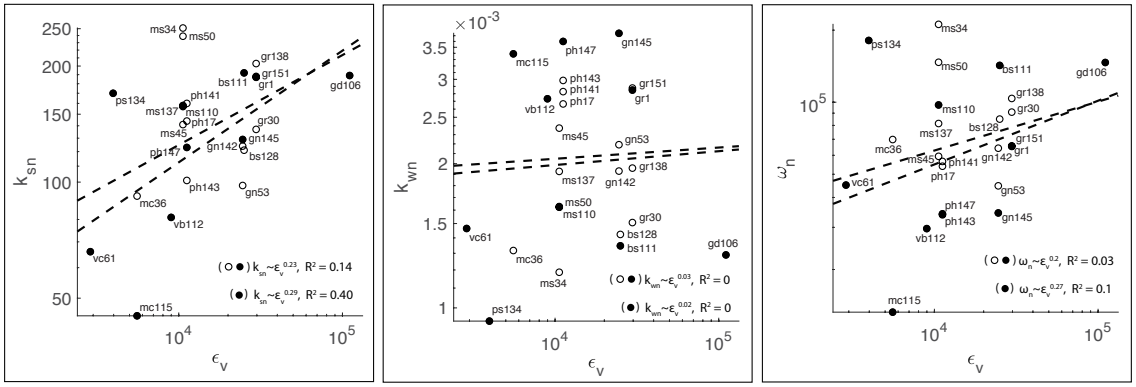

Figure 2.4: ε_v and channel morphology plotted in log-log space. Solid dots mark the reaches that bedrock samples used in abrasion experiments were collected from. Open circles mark the reaches in which ε_v is assumed. Dashed lines show the fit of the regression.

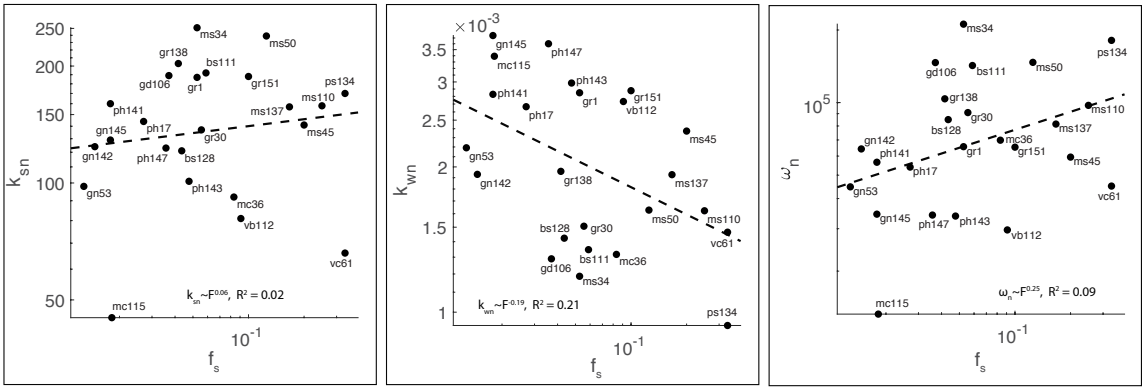

Figure2.5: f_s and channel morphology plotted in log-log space. Dashed lines show the fit of the regression.

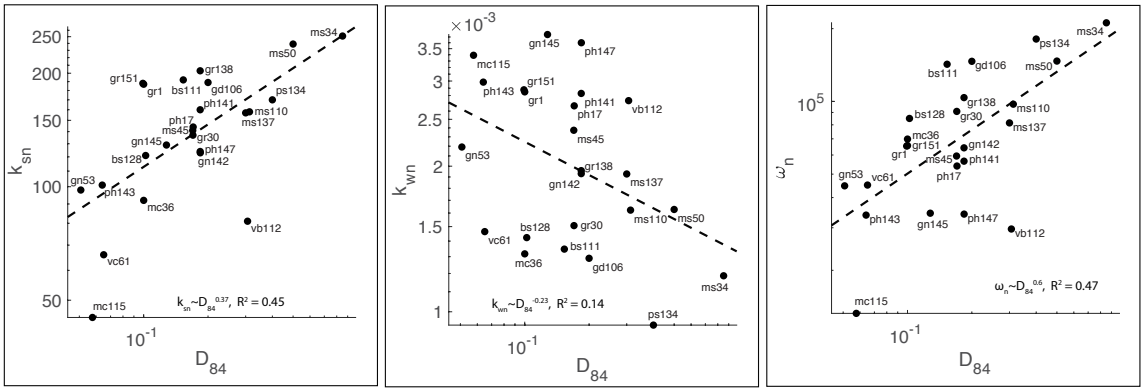

Figure 2.6: D_{84} and channel morphology plotted in log-log space. Dashed lines show the fit of the regression.

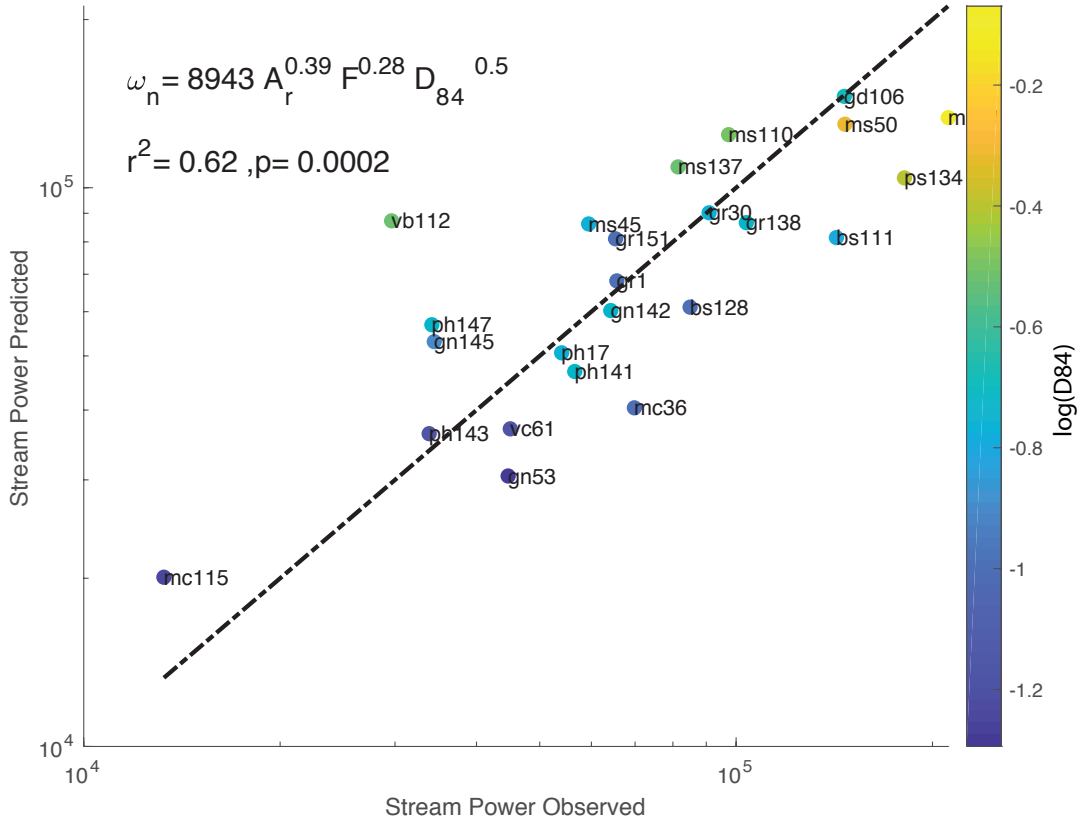

Figure 2.7: Predicted vs. observed stream power index. (A) The stream power index is predicted with the multiple-regression model equation 34. The dashed line shows the 1:1 line between predicted and observed values.

CHAPTER 4: A DAMAGE CONTINUUM FRAMEWORK FOR QUANTIFYING BEDROCK ERODIBILITY

ABSTRACT

The efficiency of river incision is strongly modulated by the resistance of the substrate to erosion processes. Yet how to quantify the resistance of a given rock type to erosion remains a difficult challenge in fluvial geomorphology. Here we suggest resistance to erosion, or erodibility, be defined as the density of discontinuities at a scale appropriate to the process of erosion. As such, erodibility can be quantified using a damage continuum framework. We use a number of laboratory and in-situ measurements of rock mass properties including tensile strength, compressive strength, and P-wave speed of bedrock channel surfaces to detect bedrock damage accumulated from weathering and bed load impacts. We introduce a method to quantify damage using P-wave speed as a proxy for microcrack density and offer empirical relationships for bedrock strength degradation with bed load impact energy for various lithologies. Our results show that channel surface P-wave speeds are 15 – 80% slower than drill core samples from 15 cm below the surface suggesting significantly more microcracking at the surface relative to the sub-surface. Based on P-wave speeds, the channel margins can be significantly weaker than the channel floor or close to the same resilience depending on the lithology. Our results suggest that the accumulation of damage along the channel floor depends on the energy of bed load impacts and that the resistance to damage depends on the inherent properties of bedrock that resist cracking (i.e. tensile strength, mineralogy, crystalline grain size). We find that damage on bedrock surfaces increases with impact energy for coarse-grained felsic rock and decreases with impact energy for finer-grained rock more susceptible to chemical weathering. This phenomenon is explained in part by fracture mechanics in which finer-grained rock is more resistant to impact damage because shorter grain boundaries limit the stress

intensity in the rock and a greater density of grain boundary junctions limit cracking. We argue that for rock that is more susceptible to chemical weathering the decrease in damage with impact energy is likely due to the rock surface being worn away exposing fresher more resistant material in a higher impact energy setting and preserving damage from chemical weathering in low impact energy environments. We use the relationship between impact energy and P-wave speed to subsume a damage equation into the Saltation-Abrasion Model. Model results show that erosional efficiency can increase or decrease with bed load particle size depending on the lithology. In summary, we suggest that a damage continuum framework for erosion resistance provides a fruitful avenue for quantifying bedrock erodibility from rock mass properties.

INTRODUCTION

Incision into bedrock drives landscape evolution and controls the topographic response to climate and tectonics. Bedrock incision sets the lower boundary condition of hillslopes and limits the elevation of peaks and ridges. River incision is the result of driving forces such as tectonics that steepen the landscape and climate that provides the hydraulic energy to drive erosional processes. The efficiency of incision is strongly modulated by the resistance of the substrate to erosion processes. Bedrock resistance to incision is limited by rock strength and has long been recognized as a first order control on landscape form (Gilbert, 1877). Yet how to quantify a given rock type's resistance to erosion remains a difficult challenge in fluvial geomorphology.

River erosion models typically characterize resistance to erosion with poorly defined erodibility coefficients calibrated from topography and known incision history (Seidl et al., 1994; Stock and Montgomery, 1999) or explicitly with rock tensile strength (Sklar and Dietrich, 2004). Although,

abrasion mill experiments demonstrate that the erosion rate can vary by an order of magnitude for a particular tensile strength (Sklar and Dietrich, 2001; Hobley, 2005). Bedrock contains numerous pre-existing flaws in the form of microscopic cracks or pores. Under tensile loading very few cracks initiate and the most critical preexisting flaws propagate and control the failure stress while less critical flaws remain static (Meredith, 1990). Thus, tensile strength tests may not be representative of bedrock incision in which the breakdown of a bedrock surface into small fragments occurs through repeated low energy impacts. The gradual degradation of the upper layer of bedrock into smaller pieces through bed load impacts was suggested by (Whipple et al., 2000) and later built into a mechanistic model through a concept based on time spent in the aging layer of bedrock (Chatanantavet and Parker, 2009). We build on this previous work developing a damage continuum framework for erosional resistance within a bedrock channel.

In this paper we suggest erosional resistance is defined as the density of discontinuities at a scale appropriate to the process of erosion. Rivers erode rock by various processes, but primarily by abrasion, plucking, and chemical dissolution (Wohl, 1993; Hancock et al., 1998; Whipple et al., 2000). The efficiency of these processes is strongly coupled to the density of cracks, which controls the size of removable pieces and the surface area of material exposed to chemical processes. Erosion of brittle materials via grain by grain abrasion occurs through the intersection of cracks (Finnie, 1960; Bitter, 1963b) and the average wear rate is theorized to scale with the flux of kinetic energy transferred by the impacting grain while the resistance to wear is set by the capacity of the material to store energy elastically (Engel, 1978). The work by Sklar and Dietrich (2004) built on these ideas and proposed a mechanistic framework that uses sediment transport dynamics to predict the abrasion rate. Yet we do not fully understand

bedrock river erosion at the grain scale because the active break down of rock at this scale is difficult to observe. Here we use tools and field techniques aimed at detecting in-situ bedrock damage accumulated by weathering and impact abrasion in a river channel (Figure 3.1). Our study is conducted over a variety of lithologies so that we may consider different structural and compositional properties of bedrock and their influence on erosion. While we focus on the grain scale in this paper, we suggest that this damage continuum framework can be up-scaled to include larger erosional events such as plucking.

BACKGROUND

Bedrock is weakened through a wide range of mechanical and chemical processes that damage rock by increasing the density of fractures. Damage is the gradual process of deterioration through the development of microvoids or microcracks. Continuum damage mechanics uses the density and growth of microscopic defects to characterize and model the macroscopic behavior of materials (Kachanov, 1958; Hult, 1979). Through mechanical damage, microcracks develop in rock that has been stressed beyond the elastic limit but has not yet failed. The probability of failure increases with the density of microcracks and depends on material properties that limit or promote crack growth including grain size, the mismatch of grain boundaries, differences in elastic moduli between minerals, and intra-crystalline flaws(Tapponnier and Brace, 1976; Grady and Kipp, 1979; Ashby and Sammis, 1990; Wong et al., 1996). Chemical damage, conceptually analogous to mechanical damage, is the partial dissolution of rock along grain boundaries prior to disintegration (Hoke and Turcotte, 2002). Damage processes ultimately promote the growth of voids or cracks in rock that mechanically concentrate external stresses that reduce the structural strength of rock.

The evolution of damage depends on the rates of crack initiation and propagation. Cracks initiate when the stress on a material surpasses the strength of that material. For geomaterials this happens during lithification, tectonic events, and geomorphic stresses. Along the channel floor, which is the focus of this study, damage can also accumulate from repeated bed load impacts (Figure 3.1). During impact, microcracks initiate and propagate at depths depending on various factors including the impact angle, particle velocity, particle mass, and the relative fracture toughness and hardness between particle and target (Wellman and Allen, 1995). Tribological studies have shown that erosion and impact damage vary with impact energy through impingement angle, velocity, angularity, and particle size (Finnie, 1960; Hutchings, 1987; Oka et al., 1997). The strength of a ceramic surface has been shown to decrease with increasing kinetic energy of impacts both theoretically (Baratta, 1981) and experimentally (Ritter, 1985). Studies of single impact indentation of brittle materials show that cracks extend radially, medianly, or nucleate at depth and extend laterally parallel to the surface (Lawn and Fuller, 1975; Lawn et al., 1980; Marshall et al., 1982; Cook and Pharr, 1990) (Figure 3.1b). Microcracks are also classified based on their location within the grain structure: grain boundary cracks are located between grains, intergranular cracks cut through more than one grain, and intragranular cracks are contained within a single grain. The growth of microcracks depends on the stress state at crack tips, which can be quantified with a stress intensity factor (K_I) commonly given as

$$K_I = s\sqrt{\pi c} \tag{35}$$

where s is the stress induced by a load and c is one half the crack length. The average length of microcracks typically scales linearly with the average grain size (Peng and Johnson, 1972; Sprunt and Brace, 1974; Hadley, 1976; Wong et al., 1996). Therefore, the strength of rock should

decrease with square root of grain size. This relation has been confirmed experimentally (Brace, 1961, 1964; Olsson, 1974; Fredrich et al., 1990).

Geomorphic processes that propagate cracks include topographic stresses (Molnar, 2004; Stock et al., 2012; Leith et al., 2014; Clair et al., 2015b), biologic activity (Viles et al., 2011), frost weathering (Walder and Hallet, 1985; Anderson, 1998; Matsuoka and Murton, 2008; Draebing et al., 2017), wetting and drying cycles (Montgomery, 2004; Stock et al., 2005; Johnson and Finnegan, 2015b; Collins et al., 2016), and thermomechanical stresses (Warke and Smith, 1998; McFadden et al., 2005; Gischig et al., 2011; Collins and Stock, 2016; Eppes et al., 2016). Crack propagation at sub-critical stress is facilitated by stress corrosion at crack tips where chemical action of an environmental agent, such as water, weakens the strained bonds at the crack tip (Atkinson, 1984). It is likely that all such near surface cracking occurs due to stress corrosion at stresses lower than the rock's critical stress (Eppes and Keanini, 2017), which would therefore be the rate-limiting factor on crack propagation when erosion process, climate, and stress loading factors are similar (Eppes et al., 2018). The environmental processes mentioned above are responsible for creating and propagating discontinuities from the microcrack scale (microns wide) to macrocrack scale (100's of microns wide) that drive patterns of landscape morphology. Our hypothesis is that bed load impacts may also play a role in modifying bedrock erodibility through the accumulation of damage at the microcrack scale. The promotion of damage depends on the energy of bed load impacts and the resistance to damage depends on the inherent properties of bedrock that resist cracking (i.e. tensile strength, fracture toughness, mineralogy, grain size).

The goals of this study are to measure bedrock damage accumulated from both weathering processes and bed load impacts and develop a basic understanding of how impact energy and material properties modulate bedrock erodibility for various lithologies. In-situ measurements of compressive strength and P-wave speed of bedrock channels are used to detect damage and validated with thin sections of samples collected from the channel surface. We introduce a method to quantify damage using P-wave speed and offer empirical relationships for strength degradation with bed load impact energy for various lithologies.

APPROACH AND FRAMEWORK

In this section, we review the damage continuum framework developed mostly by engineers but with relevance to erosional resistance to geomorphic processes. Damage can be quantified with physical parameters using the effective stress ($\tilde{s}$) concept (Chaboche, 1988), where a damaged volume of material under the applied stress (s) shows the same strain response as the undamaged one under the effective stress. Damage (D) represents the volume of material occupied by voids that is unable to support the load

$$\tilde{S} = \frac{S}{1-D}. \quad (36)$$

D is the continuum damage parameter ($0<D<1$) where $D=0$ for undamaged rock and $D=1$ for complete failure. For example, if $D= 0.5$ the same strain can be accomplished at half the stress of an undamaged volume. Therefore, rock strength (σ) measured as the peak stress prior to failure takes on the form

$$\sigma = \tilde{\sigma}(1 - D) \quad (37)$$

in which $\tilde{\sigma}$ is the strength of a pristine volume of rock and *1-D* represents the volume of intact material able to support load.

There are several ways to define and measure damage including direct observations of crack density in photomicrographs, variation in rock density, elastic modulus, ultrasonic wave speed, and electrical resistivity (Lemaitre and Dufailly, 1987). Here we apply a damage equation derived by Lemaitre and Dufailly (1987) that uses the ultrasonic wave speed of a damaged sample ($\tilde{v}_p$) relative to an undamaged sample (v_p)

$$D = 1 - \frac{\tilde{v}_p^2}{v_p^2}. \quad (38)$$

When $\tilde{v}_p << v_p$ the volume of material is highly damaged with high density of void space. When $\tilde{v}_p \approx v_p$ there is little damage and the strength of the rock (equation 37) is essentially the intact, undamaged strength. With these concepts our goal is to detect the magnitude of damage and how it influences the erosional resistance of rocks in our study area.

STUDY AREA

We study a suite of six lithologies across twelve different bedrock reaches in tributaries of the Verde River and Aqua Fria Rivers in the Prescott National Forest, Coconino National Forest, and the Bradshaw Mountains of central Arizona (Figure 3.2). This landscape is often referred to as the Mogollon Rim or the transition zone located between the Colorado Plateau and Basin and Range. Our study area receives a mean annual rainfall of ~482 mm/yr with a summer monsoon season that generates flash flooding. Ephemeral conditions of streams in this area allow direct

measurement and sampling of bedrock channel floors. Lithologies include granite, quartzite, phyllite, and greenstone of Proterozoic age. These rocks form the Bradshaw Mountains through a series of folds belts. We also include Mississippian sandstone and a Miocene basalt flow deposit. These rock types provide a range of ages, strengths, textures, and mineralogical susceptibility to weathering.

METHODS

Thin Section Analyses of Inherent Rock Properties

We make qualitative assessments of grain size, mineralogy, porosity, and crack density at the micron scale with thin sections of surface samples taken from both the channel margins and the channel floor. This allows us to categorize lithologies by their inherent properties and also provides validation measurements used as proxies for damage with qualitative inspection of cracks at the micron scale. Thin sections were prepared from rock samples that were either drilled or pried from the thalweg and margins of each lithology. Photomicrographs were taken of the thin sections under 5x magnification and stitched together. Quantitative micro-structural analyses involve detailed exploration of grain boundary, intercrystalline, and intracrystalline cracks. The diversity of such features and their relative importance to rock strength requires an effort beyond the scope of this paper to be statistically meaningful. Our qualitative analyses are meant to verify the presence of surface cracking, the types of cracking (i.e. grain boundary, intercrystalline, and intracrystalline), and offer a comparison of crystalline grain size among the different rock types.

Rock Tensile Strength

In this study the tensile strength of the rock is used as the basic component of erosional resistance, which we will later modify by a damage component that combines equations 37 and 38. We use tensile strength to follow the convention of others (Sklar and Dietrich, 2001; Johnson and Whipple, 2010; Bursztyn et al., 2015) and because it is relatively easy to measure in the laboratory due to minimal sample preparation. Tensile strength was measured at the University of Idaho on an MTS810 with Flex Test SE system using the Brazilian splitting method on 45 mm diameter discs with a thickness that met the 0.5 to 0.6 thickness/diameter ratio recommended by the International Society for Rock Mechanics. For each rock type we measured the tensile strength of 16 discs prepared from rock cores from a depth at least 3 cm below the surface. For each lithology we use the 95% of the distribution of tensile strengths as the 'intact' tensile strength.

Proxies for Damage

Damage occurring at different scales will influence the rate of different erosion processes. Thus, it is unlikely that there is a single rock mass property that will describe erosional resistance in all rock types. To account for this and make headway on how to estimate erodibility, we measure proxies for damage at different scales and use field observations of bed topography and surface roughness to infer the dominant erosion process (i.e. bed load abrasion or chemical/physical weathering).

Q Rebound Value

The Schmidt Hammer measures the rebound velocity of a spring-loaded piston on a bedrock surface. Rebound velocity has been widely used by geomorphologists to study weathering rates

and rock strength on landforms (McCarroll, 1991; Wohl and Achyuthan, 2002; Ericson, 2004; Murphy et al., 2016, 2018; Shobe et al., 2017). The rebound height is sensitive to the degree of weathering on the rock surface (Goudie, 2006; Niedzielski et al., 2009) as well as the density of discontinuities up to 6 cm depth below the surface (ASTM, 2001). We use an N-type Schmidt Hammer and report the raw Q value as a proxy for compressive strength. Q values range up to 100 with a higher Q indicating greater compressive strength. In-situ compressive strength was measured over 30 cm long transects by spacing rebound measurements apart by at least two plunger diameters until 15 to 30 values were taken for the transect. Channel margin transects were located above bankfull markers where bedrock was noticeably discolored from extended weathering. Channel floor transects were located near the thalweg.

P-Wave Speed

Pressure waves (P-waves) can travel through any medium and their speed is sensitive to the density and elastic modulus of the material. P-waves travel slower through air (~330 m/s) and water (~1450 m/s) than in rock (up to 8000 m/s in Earth's crust). Researchers have shown that speed and ultrasonic attenuation are correlated inversely with the growth and density of microcracks (Shah and Chandra, 1970; Maridet et al., 1986; Berthaud, 1991a, 1991b). The largest factor affecting the speed in rock is the amount of pore space or cracks. This effect persists at any scale from core samples to tens of meters (Clarke and Burbank, 2011) to hundreds of meters (Budetta et al., 2001; Leucci and De Giorgi, 2006). We use the P-wave speed between joints or visible cracks as a probe of the amount of damage accumulated through microfractures and chemical dissolution.

We measured the in-situ P-wave speed of the bedrock surface and drill core samples extracted from field sites. Following procedures outlined in ASTM (D 2845- 83), we measured the P-wave speed using a Pundit PL-200 Ultrasonic Pulse Velocity instrument that sends and receives acoustic transmissions between two transducers. The speed of core samples was measured with 'direct' transmission using 54 kHz transducers on either end of the cylindrical core. Core samples all had a diameter of 4.5 cm and ranged between 6.5 and 13 cm in length. The speed of in-situ bedrock surfaces was measured with 'indirect' transmission (i.e. both transducers coupled to the same surface) using 54 kHz exponential transducers, designed for measurements on rough irregular surfaces. The Pundit PL-200 documentation reports that the 'indirect' transmission results in an approximate 5% decrease in the speed relative to a 'direct' transmission. Here we account for this and increase surface measurements by 5%.

The speed of P-waves at the bedrock surface was measured along the same sub-meter length transects that compressive strength was measured. These transects did not cross any visible joints or fractures and were oriented to follow the flattest surface in order to confine wave paths to near surface depths. This method was adopted in order to isolate, as much as possible, the microcracked state of the bedrock. Speeds were recorded at 10 cm intervals along transects. Distances across which speeds were measured range from 10 cm to 30 cm. The depth of the wave path can be variable. We recorded the first arrival of the signal, which is the fastest path through the rock. However, a gradient in damage with depth can make the fastest path deeper below the surface. Due to the added length of a parabolic path the arrival time will increase resulting in a slower measured speed. A parabola that reaches 3 cm depth in homogenous material results in a 3% decrease in effective speed for a 30 cm horizontal spacing and a 17%

decrease for 10 cm spacing. While longer spaced measurements allow the possibility for deeper wave paths being the path of fastest transmission we did not notice any systematic variance in speed with transducer spacing in the 10 to 30 cm range. Furthermore, if the fastest transmission is through a deeper path it is likely because there is more damage near the surface and the longer path still reduces the measured wave speed. Therefore, P-wave speed is highly sensitive to the state of surface material.

Characterizing the Energy of Bed Load Impacts

The degree of damage on the channel floor depends on the energy of bedload impacts. The energy transferred to the channel floor from a single impact depends on the mass, shape, velocity, attack angle, and strength of the impacting particle relative to the bedrock. We lack observations of flow conditions and saltation events in the field and therefore focus only on the size of sediment in the channel, the effect of bed topography on impact angle, and the ratio of tensile strength between the saltating sediment and bedrock.

The kinetic energy (ε_k) of an impacting particle scales with the mass of the impacting particle (M), the impingement angle (α), and the diagonal velocity of the impacting particle (V)

$$\varepsilon_k = {}^{1}/_{2}\, M(\sin(\alpha)\, V)^2. \quad (39)$$

The flux of kinetic energy transferred to the bed during impact depends on the deformation of the particle and bed. Solving for all of the variables related to impact energy in a natural setting over a range of flow conditions and particle sizes, shapes, and strengths is beyond the scope of this study. We take a simple approach and focus on the impingement angle as it relates to the

bed surface. The impingement angle (the approach angle of the particle relative to horizontal) modulates both the energy of the impact and the frequency of impacts (Huda and Small 2014). For flow over a planar bed, hop height is low compared to hop length and the impingement angle is typically less than 5° (Auel et al., 2017b). Here we assume that the vast majority of impacts are at low impingement angles, and thus, bed surface angle has a dominant influence on impact angle (the angle of the approach angle relative to the bed surface angle). Bedrock protrusions into the flow can modulate the impingement angle from a direct impact delivering the total particle energy to an impact of essentially no energy when the impingement angle approaches 0° (Figure 3.3).

At each field site we acquired ground-based photography to create a sub-centimeter scale digital elevation models (DEMs) of channel bed topography over areas of ~10m^2 using structure from motion on Agisoft™ Photoscan software. DEMs of bedrock topography were converted to surface normal angles by fitting tangent planes to every point in the DEM over a moving 3x3 pixel window. The 'surface exposure angle' is the angle between the surface normal vector and a horizontal plane with upstream as positive and downstream as negative. Surfaces that are the most shielded to the flow of water and sediment have a value of -90° and faces most exposed have a value of 90° (Figure 3.3a).

We estimate impact angle (α) by subtracting an assumed impingement angle (angle between the incoming particle and a horizontal plane) of 5° from the surface exposure angle. However, surface exposure angles < 0° require further consideration because negative impact angles are

not possible. As particles saltate over the downstream side of an obstacle we assume that the impact angle decreases from the impingement angle to 0° (Figure 3.3b). Thus, impact angles from 5° and -90° are condensed to 5° to 0° with a linear function (Figure 3.3b).

RESULTS

Thin Section Analyses

Thin sections allow us to see differences in mineralogy, grain structure, and cracking at the grain scale (example photomicrographs shown in Figure 3.4). In general surface cracks, defined here as cracks in the upper millimeter of depth, are more abundant in thin sections of the channel floor than the margin. Table 3.1 lists the characteristics of each lithology. We make distinction of the different lithologies into two groups. We distinguish the groups based on mineralogy, grain size, and structure as well as their tendencies to have similar results, as we will show. Group-A is made up of the coarser-grained felsic rocks that we argue are more resistant to chemical weathering. Group-B is made up of finer-grained, mafic rocks that we argue are more resistant to bed load impacts. Although phyllite is fine grained, we place it in group-A because we suspect that it behaves more like a coarse-grained material due to its metamorphic texture. Foliations create planes of weakness, which are spaced at similar distance to the diameter of coarse minerals in granite and quartzite. If cracking along foliation planes is energetically preferred over grain boundary cracking then the foliation spacing can be considered the effective grain boundary length.

Rock Strength Metrics

The rock strength metrics reported here (tensile strength, P-wave speed, and compressive strength) were taken from 12 different bedrock reaches and 6 lithologies. The results show that the difference in observed damage of the channel margins and channel floor are lithology dependent.

Laboratory Tensile Strength

Tensile strength was measured on core samples taken from depths greater than 3 cm. At these depths it is unlikely the rock was damaged by bed load impacts; therefore we assume the variance in rock strength is indicative of the susceptibility to physical and chemical weathering processes that weaken rock. The distribution of tensile strengths measured in uniaxial loading tests shows notable differences in both the mean values and the variance of values between lithologies (Figure 3.5). The tensile strength tends to vary more for group-B (the group more susceptible to chemical weathering) than group-A suggesting greater strength degradation by chemical weathering for group-B.

Proxies for Damage

Our proxies for damage use in-situ measurements of compressive strength and P-wave speed on the bedrock channel surface. While these metrics are sensitive to different depths of the rock mass they are both sensitive to the amount of damage. The correlation between compressive strength and P-wave speed is stronger for group-B (r^2= 0.7) than group-A (r^2= 0.15) (Figure 3.6). This suggests that lithologies in group-B have less disparity in the state of material at the depth of P-wave paths and the depth of rebound sensitivity. This implies that group-A is more susceptible to surface damage and group-B is less susceptible to surface damage.

In the following two sections we report how compressive strength and P-wave speed vary between the channel margins and channel floor as well as how they vary with impact energy. These two aspects are indicative of the relative efficiency of damage induced by chemical weathering processes and bed load impacts. Damage from chemical weathering processes is likely to be more prevalent on channel margins and on channel floor surfaces shielded from direct impacts. Physical damage from bed load impacts is overall more prevalent on the channel floor and on upstream facing surfaces exposed to bed load impacts.

Compressive Strength

Channel Margins vs. Channel Floor

All six lithologies show that the channel margins are weaker than the channel floor with statistical significance (Figure 3.7a). The compressive strength of channel margins tends to cover a much wider range of values than those from the channel floor. This suggests that Schmidt Hammer rebound is strongly affected by the greater density of macrocracks and deeper weathering profiles associated with channel margins. Using a two-sided Wilcoxon rank sum test we determine the likelihood of the null hypothesis that the distribution of compressive strengths measured on the channel margins and the channel floor come from the same continuous distribution. We use a significance threshold of $p < 0.01$ for all tests. Compressive strength measurements suggest the channel margins are weaker than the channel floor with statistical significance for all six lithologies. This suggests that damage in the upper 6 cm (depth of sensitivity of the Schmidt Hammer) of the bedrock surface is more pronounced along channel margins.

Variation with Bed Topography

We explore how compressive strength varies along the topography of the channel floor and use the surface exposure angle to bed load impacts as a proxy for impact energy. For group-A, compressive strength decreases with impact energy but increases for group-B with the exception of sandstone (Figure 3.8a). We fit linear regressions to these data and report the correlation coefficient (r^2), the correlation strength of a monotonic relationship (ρ), and correlation significance (p) using Spearman rank correlation tests with significance threshold of $p< 0.01$. Overall the trends have low r^2 values due to large scatter, which is expected due to anisotropy of rock, the randomness of bed load impacts, and various environmental processes that break down rock. The fitted relations in group-A monotonically decrease with statistically significance except for quartzite. The quartzite data encompass a narrow range of surface exposure angles and may be too small for statistical testing. In group-B only the fitted relation for sandstone is statistically significant.

P-wave Speed

Channel Margins vs. Channel Floor

Drill core samples offer an opportunity to estimate the speed of rock with nominal damage. Overall the P-wave speed of bedrock surfaces is slower (~800-3200 m/s) than the 95^{th} percentile speed of core samples (the assumed 'intact' speed). The P-wave speed of bedrock surfaces is sensitive to state of the rock mass in the upper few millimeters of rock. Overall the difference is small between the mean P-wave speed of the channel margins and channel floor (Figure 3.7b). For group-A, we cannot reject the null hypothesis that the P-wave speeds of the channel margins and channel floor come from the same distribution. Group-B does show a significant difference in the speed between the channel margins and channel floor. The rock types that

show a significant difference between margin and floor speeds also have the largest decrease from the speed of the core to the speed of the surface (Figure 3.7b). This suggests that these lithologies may be more susceptible to chemical weathering and long-period environmental stresses or that surface erosion of the bedrock floor requires less damage to remove material.

Variation with Bed Topography

The trends in P-wave speed vs. impact energy are similar to those of compressive strength with the exception of sandstone, which here shows an increase in rock strength with impact energy (Figure 3.8b). Again, r^2 values are low indicating considerable randomness in the breakdown of rock surfaces under river processes. Group-A shows a decrease in P-wave speed with impact energy that is significant ($p<0.01$) for granite and phyllite, but is not for quartzite (Figure 3.8b). The slope of the fitted relations between P-wave speed and surface exposure angle for group-B range from flat to slightly decreasing suggesting weak to negative dependence of damage on bed load impact energy. In general, P-wave speed has stronger correlations (ρ) with impact angle than compressive strength suggesting that P-wave speed is more sensitive to damage accumulated from bed load impacts than Schmidt hammer measurements.

Quantifying Erodibility of the Channel Margins and Channel Floor with Damage

In the previous sections we showed the effects of damage on each lithology indicated by the difference between channel margins and channel floor surfaces. In order to measure the amount of damage accumulated in rock one must know the value of an un-damaged volume. Due to the limitations of the Schmidt Hammer we were not able to measure the at-depth compressive strength in a manner comparable to surface measurements, and thus, a damage

variable based on Schmidt Hammer measurements was not possible. P-wave speed, on the other hand, offers a non-destructive metric that can quantify the strength of both intact (core samples) and damaged rock (in-situ). The difference in core speed and surface speed is indicative of the damage accumulated in the rock over the last few decimeters of exhumation. Here we quantify the erodibility with equation 37 using the reduction in P-wave speed from core samples to the bedrock surface (Table 3.1) with equation 38. The ratio of P-wave speed between the channel margins and the channel floor suggests that channel margins can be significantly weaker than the channel floor (e.g. basalt and sandstone) or close to the same resilience (e.g. granite and quartzite) depending on the lithology (Table 3.1). Overall, the difference in erodibility between the channel margins and channel floor is less for group-A than group-B.

Predicting Damage with Impact Energy

Here we quantify the susceptibility to damage from bed load impact energy through the relationship between P-wave speed and impact angle (α) on the channel floor (Figure 3.8c). The kinetic energy of an impact (ε_k) scales with impact angle as the square of $\sin(\alpha)$ (equation 39). Because impact angle is more directly linked to energy of an impact than the surface exposure angle we convert the surface exposure angle to α (equation 38). Figure 3.8c shows how damage varies with the square of $\sin(\alpha)$ (a proxy for impact energy) for the different lithologies. Assuming that impact angle is the dominant influence on reach-scale variations in the kinetic energy of bed load impacts, we can use the data in figure 3.8c to quantify the scaling of damage with impact energy by fitting power laws to these trends

$$1 - \frac{\widetilde{V}_p^2}{V_p^2} = b((\sin\alpha)^2)^m \quad (40)$$

where the left side of equation 40 is our damage variable and the power law terms, *b* and *m,* are estimated with least squares regression. A positive value of *m* suggests that our observed damage increases with increasing bed load impact energy, while a negative value suggests that increased energy results in less damaged rock at the surface. By regression of P-wave speeds and impact energies, we find both positive and negative *m* values for the rocks of our study area. In general, group-A results in positive *m* values suggesting a graduate accumulation of damage and group-B results in negative values suggesting a diminishing accumulation of damage.

In a natural setting, channel floor damage is driven by weathering as well as bed load impacts. Upstream facing surfaces are battered by bed load impacts and the crack density should reflect the susceptibility to impact damage. Because downstream facing surfaces are shielded from impacts the effects of weathering processes are preserved. Therefore, the slope (*m*) of these relationships is strongly influenced by the relative efficiency between bed load impacts and weathering processes for the different rock types.

Similarly, the ratio of margin to floor P-wave speed is also influenced by the relative efficiency between weathering processes and bed load impacts. This is because the effects of weathering processes are preserved along channel margins, but are frequently stripped away along the channel floor. Indeed there is high correlation between *m* and the ratio of margin to floor P-wave speed (Figure 3.9).

DISCUSSION

Our results indicate that the damage continuum concept developed by engineers for complex fracturing processes is measurable in geomorphic settings. A suite of observational tools provided a consistent view that accumulation of damage depends on position within the channel, impact energy, and lithologic properties with respect to grain size, porosity, and mineralogical content (e.g. felsic vs. mafic rocks). We suggest that this provides a useful new framework to consider how different rock mass properties influence erosional resistance.

Damage is Measurable in a Geomorphic Setting

Bedrock accumulates damage at different length scales depending on the location in the channel and the process inducing the damage. Previous studies have shown that the strength of bedrock decreases with height above the channel floor (Montgomery, 2004; Stock et al., 2005; Hancock et al., 2011; Johnson and Finnegan, 2015b; Small et al., 2015; Shobe et al., 2017). Along the channel margins macrocracks are more abundant because rock is allowed more time to accumulate damage through long period weathering processes and infrequent erosion. Along the channel floor the surface is stripped away more frequently by fluvial erosion, but impacts promote the initiation and growth of microcracks. These phenomena are supported by the compressive strength and P-wave speed data of the channel margins and channel floor. Our compressive strength measurements show the expected disparity between the strength of the channel margins and channel floor. However, the P-wave speed results are more nuanced, which we suspect is due to the shallower depth through which the P-wave signal travels and is thus more affected by the shallow damage inflicted by bed load impacts.

Q Rebound Value

The Schmidt Hammer is well suited to detect damage in the form of chemical dissolution and macrocracks because the rebound is sensitive to discontinuities up to 6 cm below the surface (ASTM 2001). These forms of damage occur at greater depths than impact damage at the surface. We suggest that this is why there is a stronger distinction between the compressive strength of the margins and floor than the P-wave speeds. Small et al. (2015) performed experiments on rock discs removed from channel surfaces and showed that the abrasion rate of channel margins can be an order of magnitude faster than the channel floor. Furthermore, they showed that the rate of abrasion decreases with depth into the rock sample due to weakened surfaces. Both margin and floor samples approach a steady abrasion rate at depth; however, the margin samples require an order of magnitude greater depth to reach this steady rate. They suggest the difference in abrasion rates is a result of weathering enhanced erodibility. Shobe et al. (2017) showed that macrocrack density increases with height above the channel floor while the compressive strength (Schmidt Hammer rebound) decreases. The Schmidt Hammer rebound values at our field sites is consistent with these previous findings that found the channel margins to be significantly weaker than the channel floor. We propose that this distinction is pronounced in Schmidt Hammer rebound values because the channel margins have a deeper weathering profile within the depth range of sensitivity of the instrument.

P-Wave Speed

P-wave speed is better suited to detect bed load impact damage if speeds are measured between macrocracks. The first arrival of the P-wave signal follows a shallow path beneath the surface, and therefore, is able to distinguish differences in near surface microcrack density. This is supported by evidence of surface cracks in thin sections and the resulting P-wave speeds. Thin

sections of the channel floor show more surface cracks than the channel margins for group-A. The P-wave speeds of group-A reveal that damage is as severe on the channel floor as the channel margins (Figure 3.7a) challenging the expectation that margins should be more damaged due to prolonged exposure to environmental stresses. Thin sections of group-B show much less evidence of surface cracks and P-wave speeds are clearly faster along the channel floor than the channel margin. This suggests that for group-A lithologies, bed load impacts are as effective as long-period environmental cracking processes at damaging bedrock surfaces, at least through the depth that the P-wave signal was transmitted.

Benefits of a Damage Framework

Measuring the P-wave speed of the bedrock surface offers a non-destructive technique that is more sensitive to the surface erodibility than bulk tensile strength measurements and is simple to acquire in the field. Channel surface thin sections show that the failure strength has been exceeded in flaws within the upper few millimeters but the surface remains intact. This observation is consistent with the experiments of Small et al. (2015), which showed that the strength of bedrock rapidly declines towards the surface within the upper few millimeters. However, the upper few millimeters of the bedrock surface are difficult to measure with failure strength tests due to the dimensions of samples required for testing. Although brittle-material impact wear theory provides a means to characterize the resistance to erosion with tensile strength (Engel, 1978), abrasion mill experiments demonstrate that the erosion rate of natural rock samples can vary by an order of magnitude for a particular tensile strength value (Sklar and Dietrich, 2001; Hobley, 2005). The tensile strengths measured in this study vary significantly for any particular lithology (Figure 3.5). Thus to estimate bedrock resistance to erosion with

laboratory measurements of tensile strength leaves much uncertainty if the tensile strength varies appreciably due to damage of the near surface. The Schmidt Hammer may be sensitive to discontinuities that are too deep to influence the near-surface strength. However, the decrease in P-wave speed of rock from depth relative to the surface allows us to quantify the weakening of rock from an estimated 'intact' value. This offers a method to estimate the damage of different rock types subjected to various environmental stresses (i.e. bed load impacts, chemical weathering, etc.).

Material Properties that Control Damage

Mineralogy, crystalline grain size, and porosity affect the susceptibility to damage through grain boundary cracking. The energy of grain boundary cracking is roughly one half that for intra-crystalline cracking (Davidge, 1979) and rock with weak grain boundaries is shown to erode by grain plucking without need for intragranular cracks (Ajayi and Ludema, 1992). Thus, grain boundary cracking is energetically preferred. The factors that limit grain boundary cracking are the strength of grain boundaries, grain boundary length, and complex boundary junctions.

Mineral weathering degrades the strength of grain boundaries and prepares rock for individual grain plucking. Weathering of minerals depends on the chemical composition of the minerals and is enhanced by porosity. Mafic silicates like olivine and pyroxene tend to weather much faster than felsic minerals like quartz and feldspar. Additionally, pore space allows more of the weathering agent to come in contact with grain boundaries. Thus, mineral composition and porosity play a significant role in the strength of grain boundaries.

The susceptibility to microcracking increases with grain boundary length. Grain boundary length and the density of boundary junctions are both a function of grain size. Smaller grains have shorter grain boundaries and therefore less stress intensity (equation 35) along grain boundaries. Thus, if grain boundaries provide the initial flaws from which microcracks propagate then smaller grained rock is more resistant to microcracking. Experiments have shown the strength of rock to decrease with square root of grain size (Brace, 1961, 1964; Olsson, 1974; Fredrich et al., 1990).

The susceptibility to microcracking decreases with the density of boundary junctions. Grain boundary junctions are where two or more grain boundaries meet. Experiments have shown that material eroded by individual grain plucking and grain boundary fracture, will have increased resistance to cracking due to higher density of grain boundaries (Davidge and Riley, 1995; El-Raghy et al., 2000). Thus, fine-grained material is likely more resistant damage due to higher density of grain boundary junctions and enhanced long-crack toughness.

Damage Susceptibility for Group-A Lithologies

The lithologies in group-A have a higher susceptibility to impact damage than chemical damage because they are of felsic composition, have low porosity, and are coarse-grained. Our results confirm this hypothesis in the following aspects. First, there is less variation in the drill-core tensile strengths of group-A, which suggests less damage due to chemical weathering (Figure 3.5). Second, the ranges of surface P-wave speeds are statistically indistinguishable between the channel margins and channel floor (Figure 3.7). Channel margins are typically weaker than the channel floor (Montgomery, 2004; Stock et al., 2005; Hancock et al., 2011; Johnson and

Finnegan, 2015b; Small et al., 2015; Shobe et al., 2017), but our results suggest that the upper few millimeters of group-A bedrock are as damaged on the channel floor as the channel margin. Third, channel floor surfaces exposed to high energy impacts are more damaged than surfaces shielded from impacts for group-A, which is indicative of the relative susceptibility to physical damage and chemical damage (Figure 3.8).

Damage Susceptibility for Group-B Lithologies

The lithologies in group-B have a higher susceptibility to chemical damage than impact damage because they are either mafic or have high porosity (in the case of sandstone in this study) and are fine-grained. Our results confirm this hypothesis in the following aspects. First, there is greater variation in the drill-core tensile strengths of group-B than of group-A, which suggests more from to chemical weathering (Figure 3.5). Second, the mean compressive strengths and P-wave speeds are significantly less on the margins than the floor (Figure 3.7). Third, group-B channel floor surfaces that are shielded from impacts are more damaged than surfaces exposed to impacts (Figure 3.8). In this case, greater susceptibility to chemical weathering weakens grain boundaries and prepares bedrock for individual grain plucking thereby exposing fresher rock. Work on basalt channels in Hawaii revealed higher compressive strength (Schmidt Hammer rebound) on upstream facing surfaces than downstream facing surfaces (Murphy et al., 2018). They suggest that upstream facing surfaces are subjected to frequent erosion exposing fresh rock while the downstream facing surface is shielded from impacts allowing the surface more time to weather. Weathering rates are likely slower in Arizona compared to Hawaii, but we observe a similar trend emerge for greenstone, basalt, and sandstone (Figure 3.8).

Integrating Damage into the Saltation-Abrasion Model

The well-known Saltation-Abrasion Model (SAM) (Sklar and Dietrich, 2004) is a mechanistic model of impact abrasion by bed load sediment. The SAM solves for the vertical incision rate as the product of the volume removed per impact (V_i), the impact frequency (I_r), and the fraction of exposed bedrock (F_b)

$$E = V_i I_r F_b. \tag{41}$$

Empirical relationships of sediment transport dynamics allowed the authors to model incision rate (E) as a function of transport stage (τ^*/τ_c^*)

$$E = \frac{0.08 R_b g q_s}{\varepsilon_v}\left(1 - \frac{q_s}{q_t}\right)\left(\frac{\tau^*}{\tau_c^*} - 1\right)^{-1/2} \tag{42}$$

where ε_v is the energy to erode a unit volume of material, R_b is sediment buoyancy, g is gravity, q_s is sediment flux per unit width, q_t is sediment transport capacity, τ^* is the nondimensional bed shear stress ($\tau^* = \rho_w g H S/(\rho_s - \rho_w) g D_s$), and τ_c^* is the value of τ^* at the threshold of sediment motion. The energy required to erode a unit volume of material (ε_v) is the resistance to erosion and depends on the substrate's capacity to store elastic energy (Engel, 1978; Sklar and Dietrich, 2004)

$$\varepsilon_v = k_v \frac{\sigma_t^2}{2Y} \tag{43}$$

where k_v is a dimensionless constant that depends partly on the bedrock material properties and partly on the bed load properties, Y is Young's modulus of the bedrock, and σ_t is the tensile strength of the bedrock.

We can subsume a continuum damage framework into the erosional resistance term by applying the effective stress concept (Equation 36) to the yield strength of the material

$$\varepsilon_v = k_v \frac{(\sigma_t(1-D))^2}{2Y}. \quad (44)$$

Equation 44 implies that as damage increases so does the erosion rate. Damage can be estimated with values of $\tilde{v}_p$ and v_p as we have done or with any other metric that can estimate the difference in strength between an intact sample and the bedrock surface. We can also consider the effect of damage driven by impact energy. The kinetic energy of an impact increases with particle mass, velocity, or impact angle (equation 39). In the SAM, impact energy scales with transport stage and sediment diameter (D_s) according to

$$\varepsilon_k = 0.058\pi\rho_s D_s^4 R_b g \left(\frac{\tau^*}{\tau_c^*} - 1\right)^{0.36}. \quad (45)$$

The scaling relationship between P-wave speed and impact angle (Figure 3.8c) provides a way to treat weakening of the bedrock surface due to bed load impacts

$$D = b\varepsilon_k^m \quad (46)$$

where *b* and *m* (Table 3.1) are taken from the power law fits of the data in figure 3.8c. Our values for *m* imply that the resistance to erosion decreases with impact energy for group-A lithologies and increases with impact energy for group-B lithologies. We argue this reflects the efficiency of weathering processes vs. the efficiency of impact processes, both influenced by material properties.

To demonstrate implications of incorporating damage in the SAM we consider the effect of bed load sediment size (D_s) on erosion rate. We calculate the erosion rate of our six lithologies using one transport stage for a range of grain sizes from sand to cobble (model inputs listed in Figure 3.10). This set up could be imagined as a river undergoing a continual rise in flow stage. As the energy of the stream continues to rise the size of sediment at a transport stage of 5 continues to increase. Figure 3.10 only plots the effects of those sediment sizes at a transport stage of 5. The response of the damage model (Figure 3.10a) deviates from the original model (Figure 3.10b). Erosion rates are shifted from the original model because equation 45 (damage model) results in a much less resistant substrate than equation 44 (original SAM). In the original SAM (Figure 3.10b) there is no change in erosional efficiency with increasing bed load sediment size greater than 2 cm (this threshold is due to the sediment cover effect discussed below) because of the tradeoff in impact rate (I_r) and volume removed per impact (V_i). Increasing bed load sediment size increases the volume removed per impact but decreases the impact rate at proportions that do not change the effect the erosion rate. That is not the case for the model that includes damage (Figure 3.10a). In the damage model, the exponent *m* causes either an increase or a decrease in erosion rate with impact energy.

Figure 3.10c shows how increasing grain size affects the three components of the SAM: volume removed per impact (V_i), impact rate (I_r), and fraction of exposed bedrock (F_b). Note that under these model inputs, the channel bed becomes covered by sediment and erosion goes to zero as bed load sediment sizes approach 8 mm. This is due to the number of particles per area of the bed decreasing as sediment size increases but the mass flux rate of sediment (q_s) remaining constant. The slope of volume eroded per impact steepens for weathering resistant rock and

lessens for weathering susceptible rock, while impact rate remains unchanged. This slight change in the volume removed per impact causes erosional efficiency to increase with bed load sediment size for group-A lithologies and to decrease for group-B lithologies (figure 3.10a). A fracture mechanics explanation for this behavior is that lithologies in group-A continually increase in erosional efficiency with impact energy due to growth of impact cracks out pacing the erosion rate. The erosional efficiency of lithologies in group-B initially increases with sediment size, but peak at a relatively small sediment size suggesting that as impact energy increases erosional efficiency decreases because fresh material is exposed that has not inherited deformation from impacts.

CAVEATS

The lithologies studied here comprise a limited range of rock properties. We infer that mineralogy and grain structure play significant roles in promoting damage, but the interaction between these effects are difficult to understand without more data. For example, coarse-grained mafic rock is not represented, nor is a fine-grained felsic rock with low porosity. We chose to investigate lithologies that are subjected to similar environmental conditions (i.e. climate and tectonics) and are therefore limited to lithologies that outcrop in a small region.

There is notable scatter in the compressive strength and P-wave speed data producing wide distributions in figure 3.7 and low r^2 values in figure 3.8. This is likely due to complex interactions between various damage processes, interactions between bed topography and flow dynamics, or the erosion of evidence as crack density increases. Additionally we did not consider the other environmental factors such as the effect that solar insolation and aspect would have

on the channel floor damage values (Warke and Smith, 1998; McFadden et al., 2005; Gischig et al., 2011; Collins and Stock, 2016; Eppes et al., 2016). Exposure to the sun can limit cracking by reducing moisture in the rock or enhance cracking from thermomechanical stresses. Quantifying the tradeoff in damage accumulation between these subcritical processes and the effects on cracking via bed load impacts is necessary to develop empirical relationships, but is beyond the scope of this study. Impact energy may not monotonically increase with bed surface exposure angle in all cases. For example the flow field around obstacles may create eddies or vortices that direct impacts in unpredictable ways. Nonetheless, we suggest that the damage concept utilized and quantified here provides a fruitful avenue towards understanding how to quantify erosional resistance among different rock types.

CONCLUSION

We introduce a continuum damage concept to quantify bedrock resistance to fluvial erosion. In-situ measurements of compressive strength and P-wave speed offer valuable tools to characterize bedrock damage. We have utilized these tools to quantify local variations in damage along bedrock river channels. Our results suggest a fundamental difference in the way bedrock channels erode that depends on lithologic properties of crystalline grain size, structure, and mineralogy.

We use tensile strength and two damage proxies, compressive strength and P-wave speed, to detect the degree of bedrock damage at sub-joint spacing scales. The tensile strength of drill cores extracted from below the channel surface show considerable variance for each lithology suggesting varying degrees of susceptibility to sub-surface damage. Bedrock along channel

margins is exposed to longer durations of weathering, and therefore, are typically much weaker than the channel floor which is eroded more often exposing fresher surfaces. Compressive strength measurements show the expected disparity between the strength of the channel margins and channel floor. The difference in P-wave speeds is statistically less distinct for most lithologies, which is likely caused by the near-surface path of the P-wave signal impeded by shallow cracking from bed load impacts.

We show that efficiency of damage caused by weathering processes and bed load impacts is lithology dependent. We split the six lithologies into two groups based on their mineralogy, crystalline structure, and surface cracking in thin section. Our results suggest opposing behavior between the two groups. Group-A (granite, quartzite, and phyllite) is more resistant to damage from weathering processes, but less resistant to bed load impact damage. Group-B (greenstone, basalt, and sandstone) is less resistant to damage from weathering processes, but more resistant to bed load impact damage. Lithologies of group-B have greater variance in tensile strength of rock cores, larger separation between in-situ strength measurements of the margins and floor, and stronger surfaces on upstream sides of bedrock protrusions than lithologies of group-A. The erodibility of channel margins is up to 2x greater than the channel floor for group-B, but for group-A the difference in erodibilities is much less. These findings suggest that the evolution of reach-scale bedrock channel morphology and roughness is lithology dependent. The effective stress concept is used to quantify rock strength by the volume of material that is un-damaged and can therefore support load. We develop an equation that quantifies the strength degradation with impact energy and subsume the equation into the erosional resistance factor of the Saltation-Abrasion Model. Our modification to the model allows the

strength of the bedrock channel surface to evolve with impact energy. Using a range of bed load grain size as the motive for increasing impact energy we compare model behavior. The original Saltation-Abrasion model predicts that erosional efficiency of impacts is independent of bed load sediment size. Our modification demonstrates how erosional efficiency may increase or decrease with bed load grain size depending on lithologic properties of the bedrock channel. This work highlights the need to incorporate granular scale bedrock properties into erosion al resistance terms and places further importance on the channel sediment size distribution in modeling bedrock incision.

Table 3.1: Schmidt Hammer and P-wave Speed Data

Table 3: Schmidt Hammer and P-wave Speed Results

	Margins		Floor		Rock Core Measurements		D		σ(1-D)		Power Law Terms	
	P-wave Velocity (km/s)	Compressive Strength (Q)	P-wave Velocity (km/s)	Compressive Strength (Q)	P-wave Velocity 95th Percentile (km/s)	Tensile Strength 95th Percentile (Mpa)	Margins	Floor	$\sigma_{tmargins}$	σ_{tfloor}	Coefficient *b*	Exponent *m*
Granite	2.46 +- .38	64.26 +- 14.7	2.48 +- .45	72.59 +- 8.4	4.02	7.29	0.54	0.53	3.36	3.43	0.71	0.044
Quartzite	2.88 +- .1	62.76 +- 4.01	2.76 +- .18	76.94 +- 2.4	5.11	14.39	0.71	0.73	4.22	3.89	0.84	0.036
Phyllite	2.59 +- .32	68.95 +- 9.49	2.86 +- .32	75.13 +- 8.3	5.63	17.68	0.73	0.68	4.73	5.74	0.72	0.024
Greenstone	2.37 +- .23	59.94 +- 6.09	3.01 +- .32	72.15 +- 9.3	6.15	16.39	0.81	0.69	3.16	5.08	0.65	-0.017
Basalt	1.96 +- .18	51.64 +- 6.06	2.93 +- .51	76.22 +- 8.1	5.45	18.25	0.86	0.68	2.62	5.86	0.74	-0.008
Sandstone	0.99 +- .33	40.96 +- 12.51	1.31 +- .3	42.89 +- 8.1	5.03	19.33	0.95	0.90	1.02	1.86	0.91	-0.005

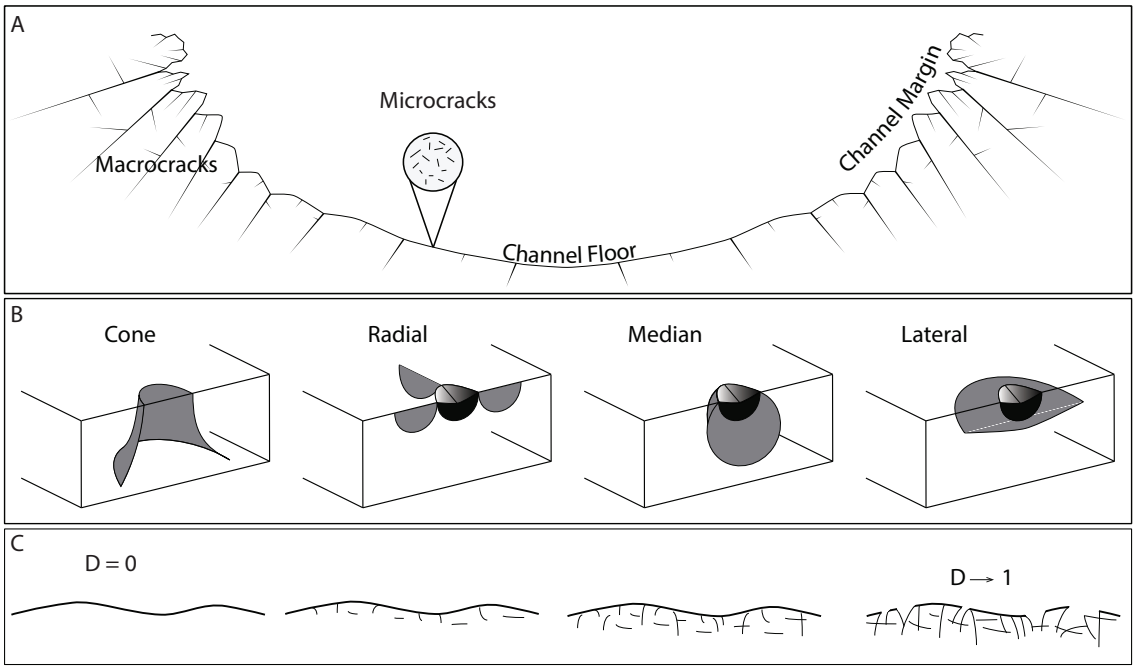

Figure 3.1: Conceptual model of bedrock channel cracking. (A) Cross-section view, the density of cracks increases with height above the channel floor (Shobe et al., 2017) because bedrock that is less frequently exposed to fluvial processes is allowed more time to accumulate damage through long period weathering processes and infrequent erosion. We define channel margins as bedrock along the river banks that lies above high flow markers (B) Types of cracks produced by particle impact (adapted from Cook and Pharr, 1990). (C) Conceptual evolution of impact damage on a bedrock surface.

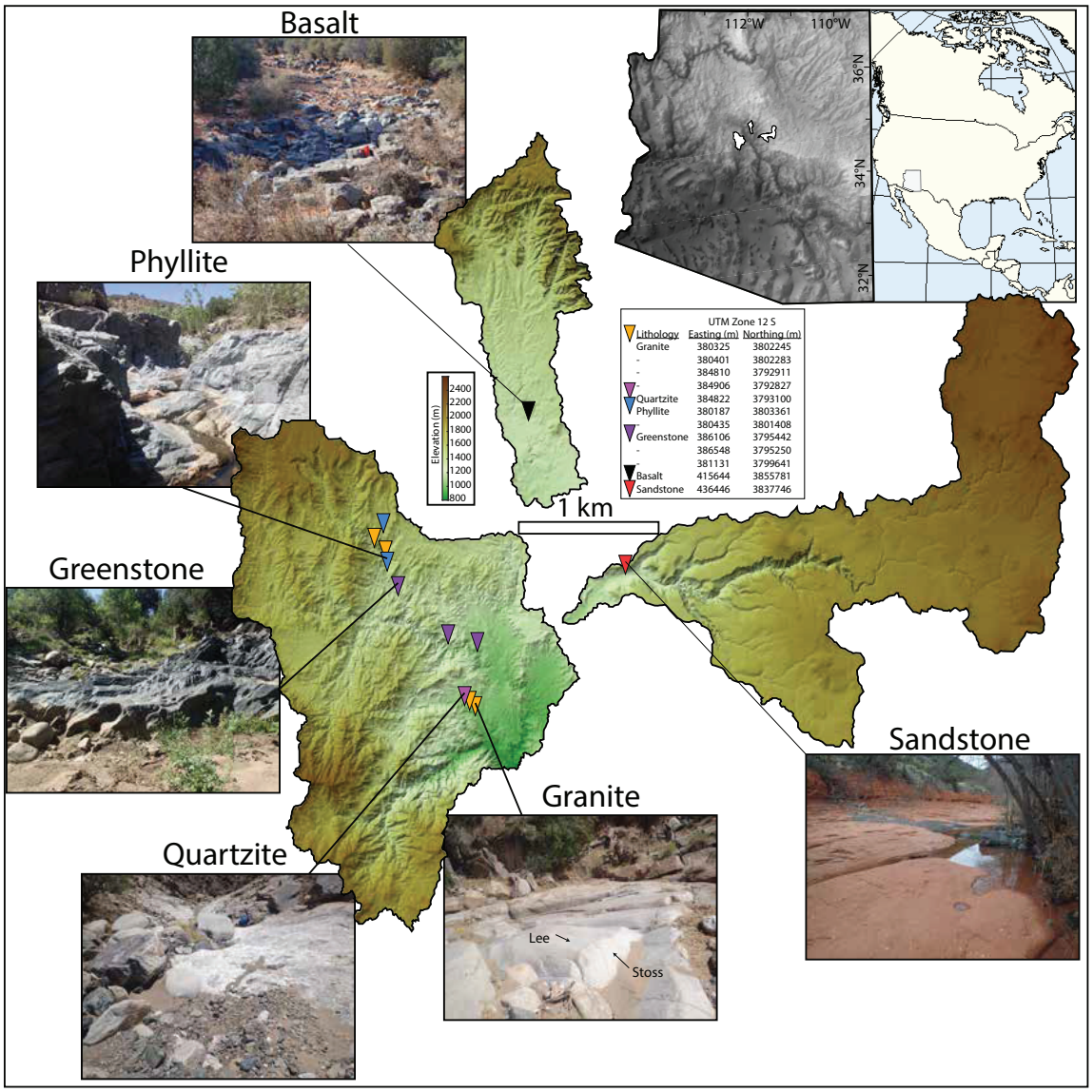

Figure 3.2: Study Area. Central Arizona.

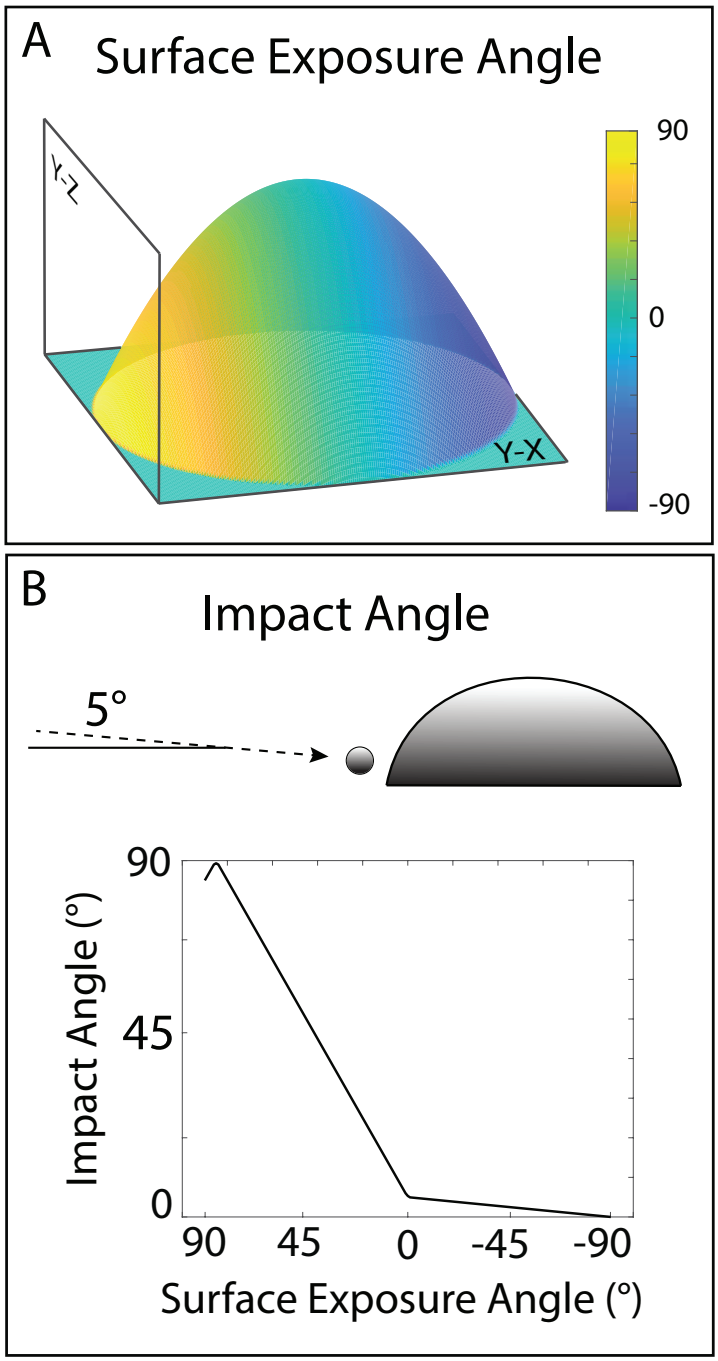

Figure 3.3: Bed topography and impact angle. (A) Surface Exposure angle of a bedrock protrusion. Downstream flow is left to right. Upstream facing surfaces are exposed to bed load impacts and downstream facing surfaces are shielded. (B) Conversion of surface exposure angle to impact angle assuming a 5° impingement angle for all impacts on upstream facing surfaces. Impacts on downstream facing surfaces are converted with a linear function from 5° to 0°.

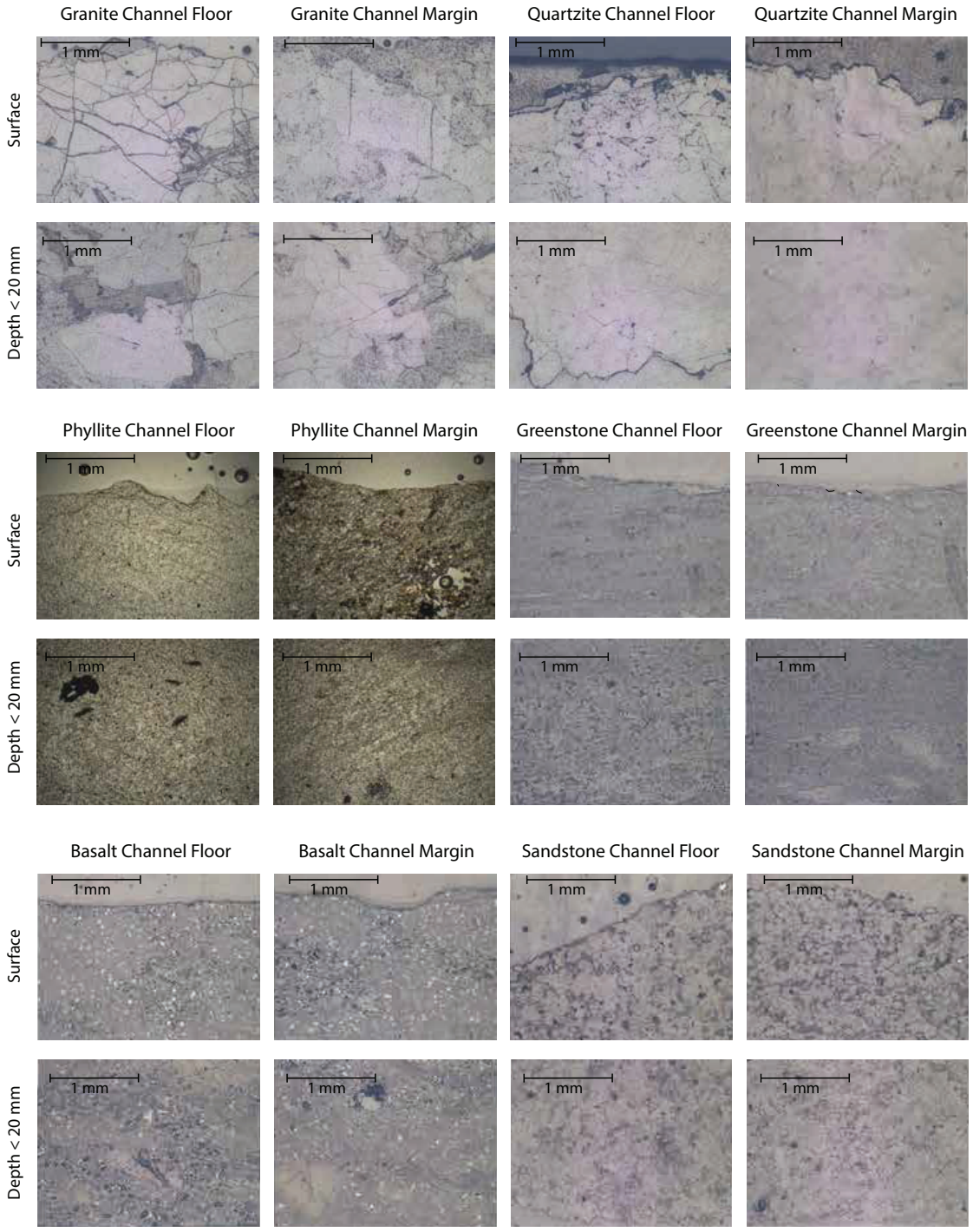

Figure 3.4: Photomicrographs of bedrock surface. For each rock type there is an example of the channel floor and channel margin at the surface and 20 mm depth. Images taken under plane polarized light. Images of phyllite were taken with direct light to show foliation planes. All other images are reflected light.

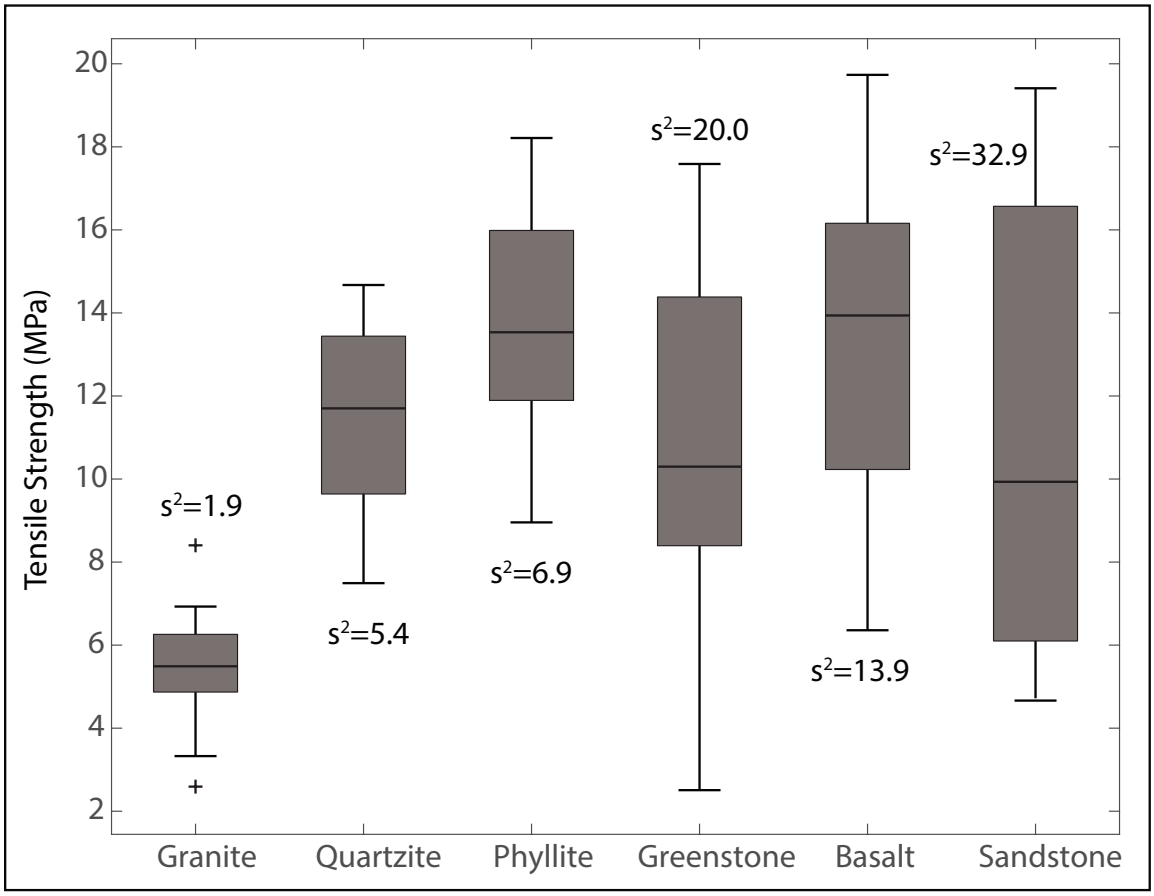

Figure 3.5: Boxplots of tensile strength for each rock type. The central red bar is the median, the box edges are the 25th and 75th percentiles, whiskers extend to the most extreme values, and outliers are plotted as red crosses. The variance of each distribution is shown next the boxes (s^2).

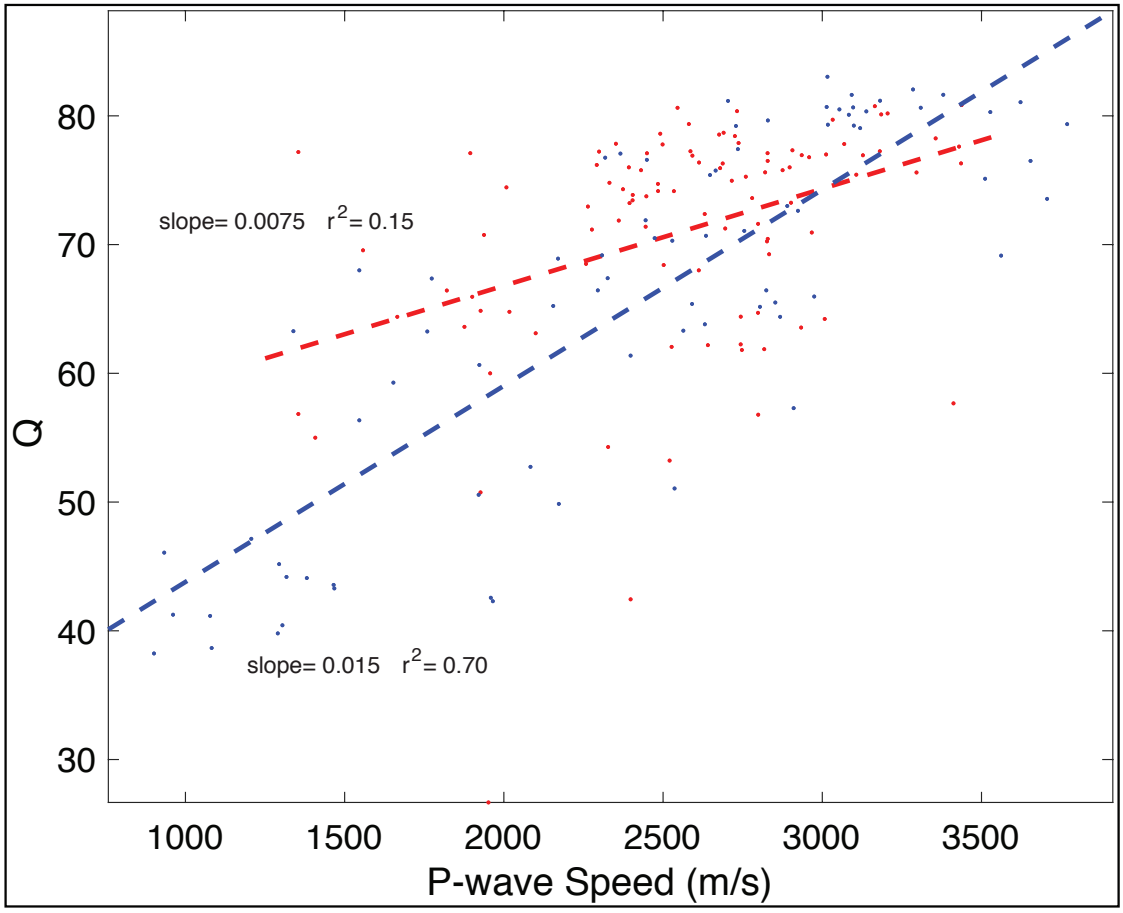

Figure 3.6: The correlation between Schmidt Hammer rebound and P-wave speed for group-A (red) and group-B (blue).

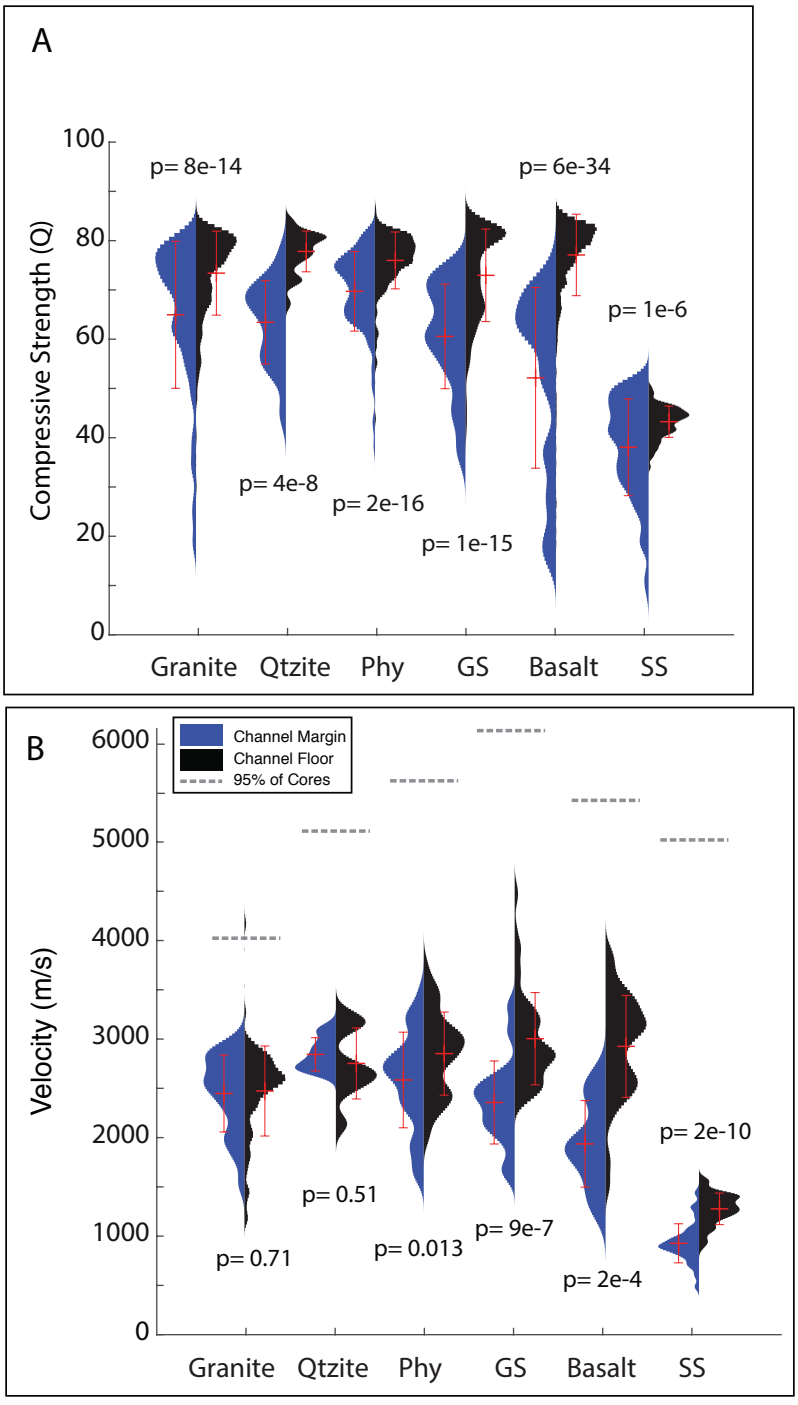

Figure 3.7: Violin plots of P-wave speed and compressive strength distributions. Violins are probability density curves smoothed with a normal kernel function. Widths of the violins are normalized in order to visually compare the distributions with smaller datasets. Red crosses show the mean and whiskers extend to the standard deviation. The statistical significance (p) is shown next to each lithology. (A) Compressive strength. (B) P-wave speed. Gray dashed lines are the 95th percentile tensile strength of drill core samples.

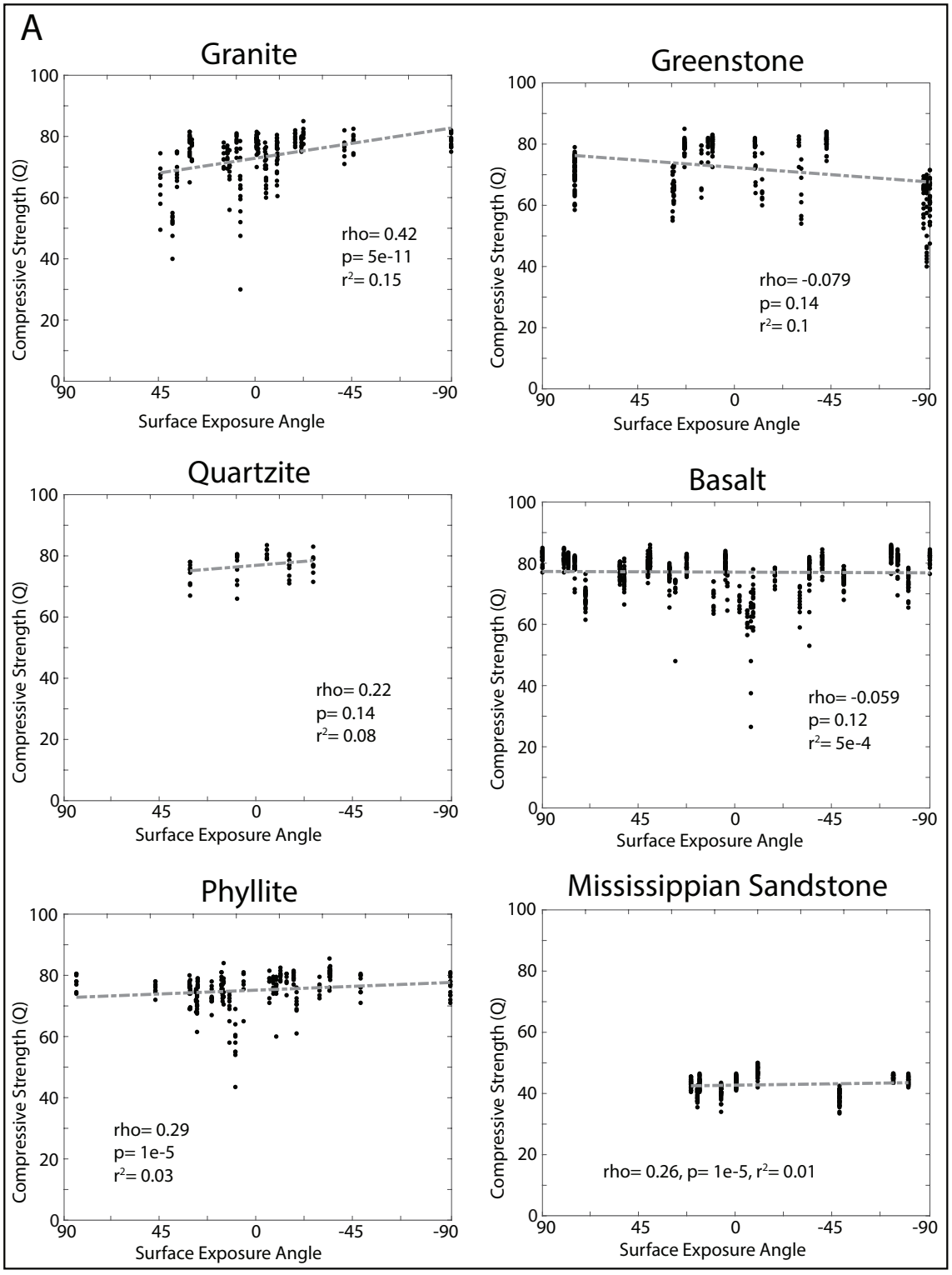
A
Granite
Compressive Strength (Q)
Surface Exposure Angle
rho= 0.42
p= 5e-11
r²= 0.15
Greenstone
rho= -0.079
p= 0.14
r²= 0.1
Quartzite
rho= 0.22
p= 0.14
r²= 0.08
Basalt
rho= -0.059
p= 0.12
r²= 5e-4
Phyllite
rho= 0.29
p= 1e-5
r²= 0.03
Mississippian Sandstone
rho= 0.26, p= 1e-5, r²= 0.01

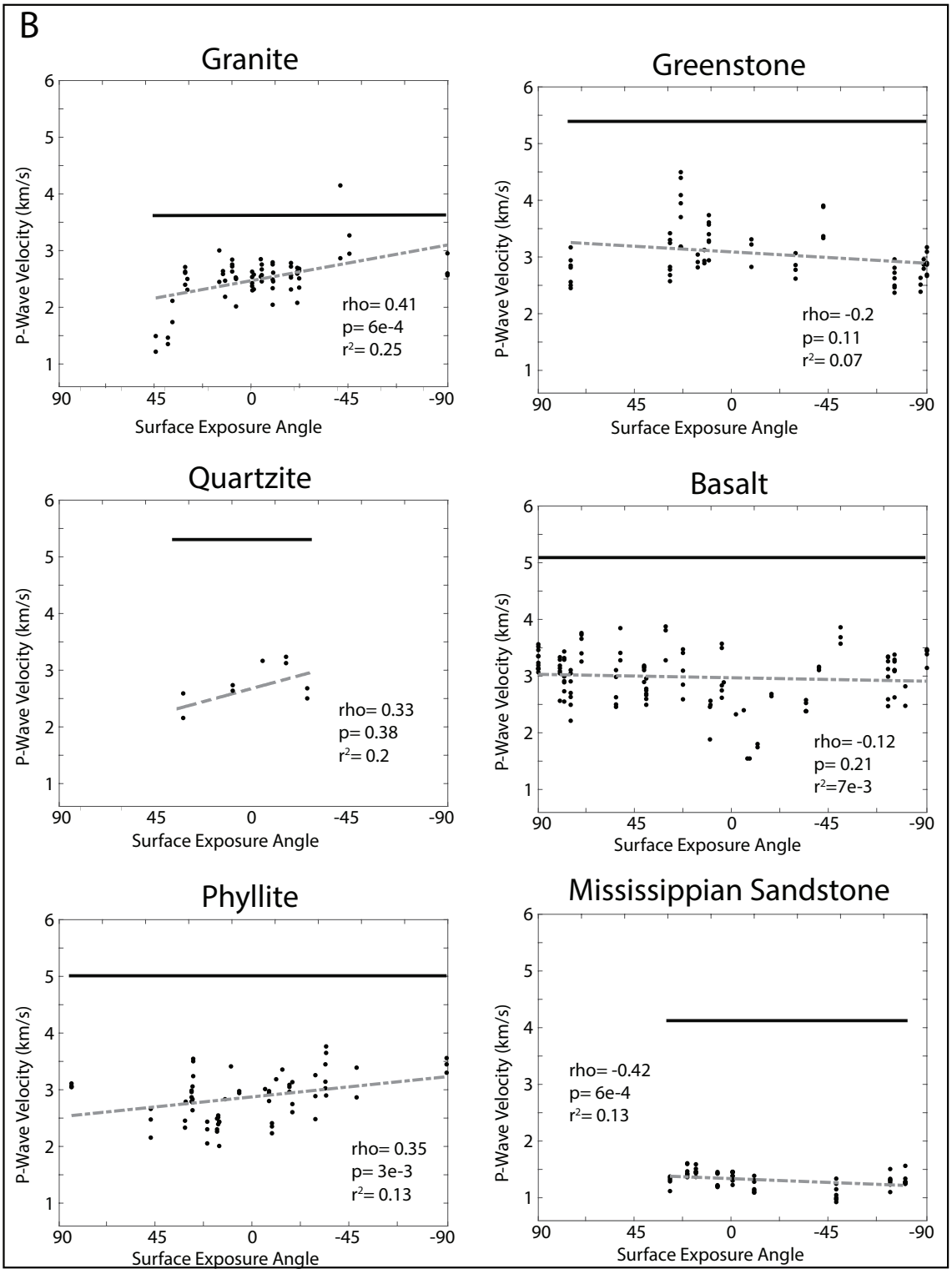
B
Granite
P-Wave Velocity (km/s)
Surface Exposure Angle
rho= 0.41
p= 6e-4
r²= 0.25
Greenstone
rho= -0.2
p= 0.11
r²= 0.07
Quartzite
rho= 0.33
p= 0.38
r²= 0.2
Basalt
rho= -0.12
p= 0.21
r²=7e-3
Phyllite
rho= 0.35
p= 3e-3
r²= 0.13
Mississippian Sandstone
rho= -0.42
p= 6e-4
r²= 0.13

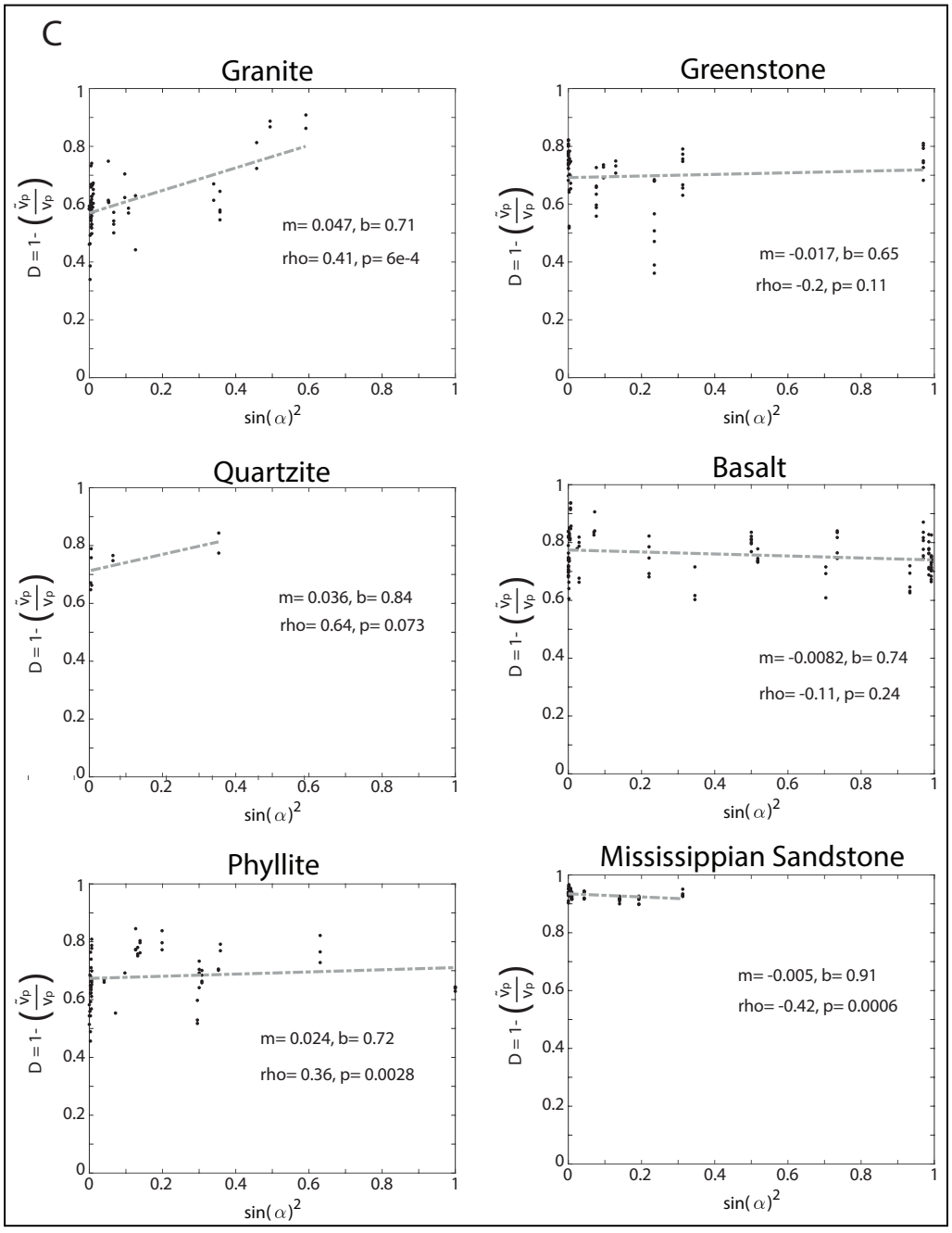

Figure 3.8: Variation of in-situ P-wave speed and compressive strength of the channel floor topography. Spearman rank correlation test parameters r^2, ρ, and p are shown for each lithology. (A) P-wave speed vs. exposure angle. Black solid lines are the 95th percentiles P-wave speed of drill core samples. High values of exposure angle are upstream facing and receive more impact energy than low values of exposure angle, which are downstream facing. (B) Compressive strength vs. exposure angle. (C) Damage vs. impact angle. The damage variable is calculated with equation 38 and the exposure angle is converted to impact angle. Power law terms *b* and *m* are shown for each lithology.

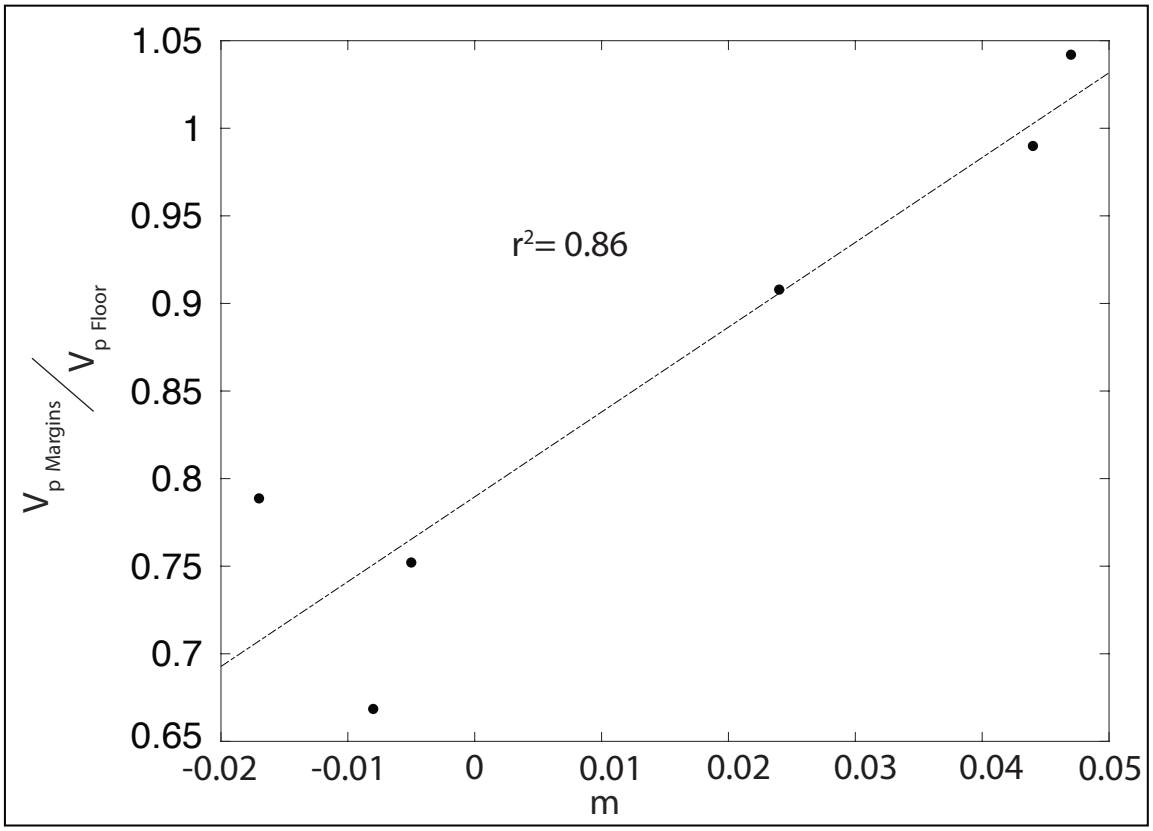

Figure 3.9: The correlation between *m* and the ratio of P-wave speed between the channel margins and channel floor.

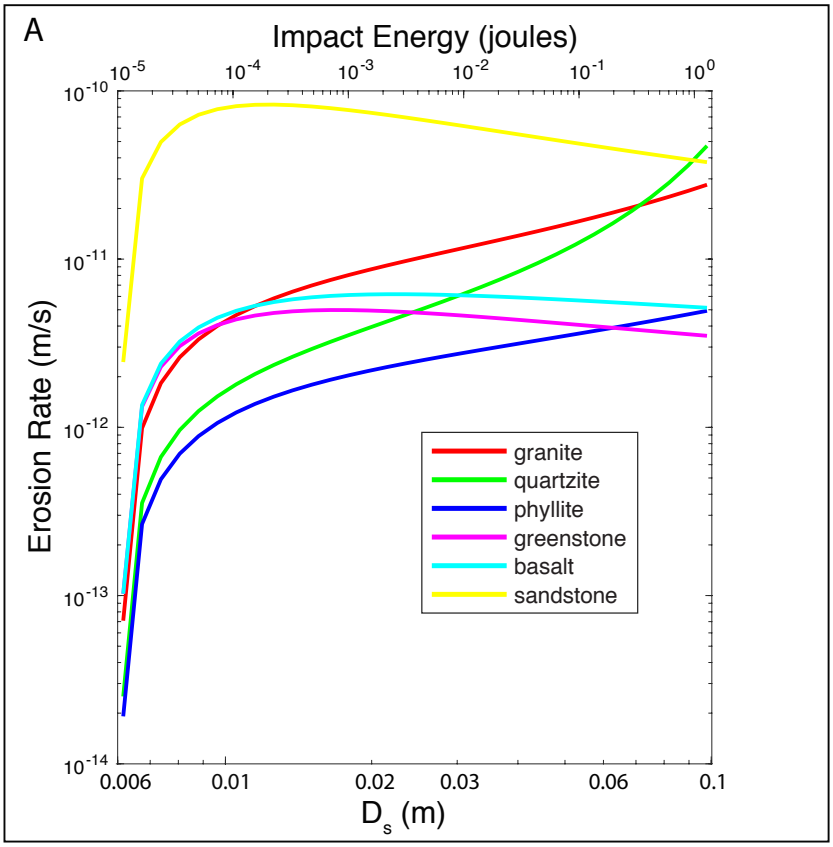
A
Impact Energy (joules)
10^-5
10^-4
10^-3
10^-2
10^-1
10^0
Erosion Rate (m/s)
10^-10
10^-11
10^-12
10^-13
10^-14
granite
quartzite
phyllite
greenstone
basalt
sandstone
0.006
0.01
0.02
0.03
0.06
0.1
D_s (m)

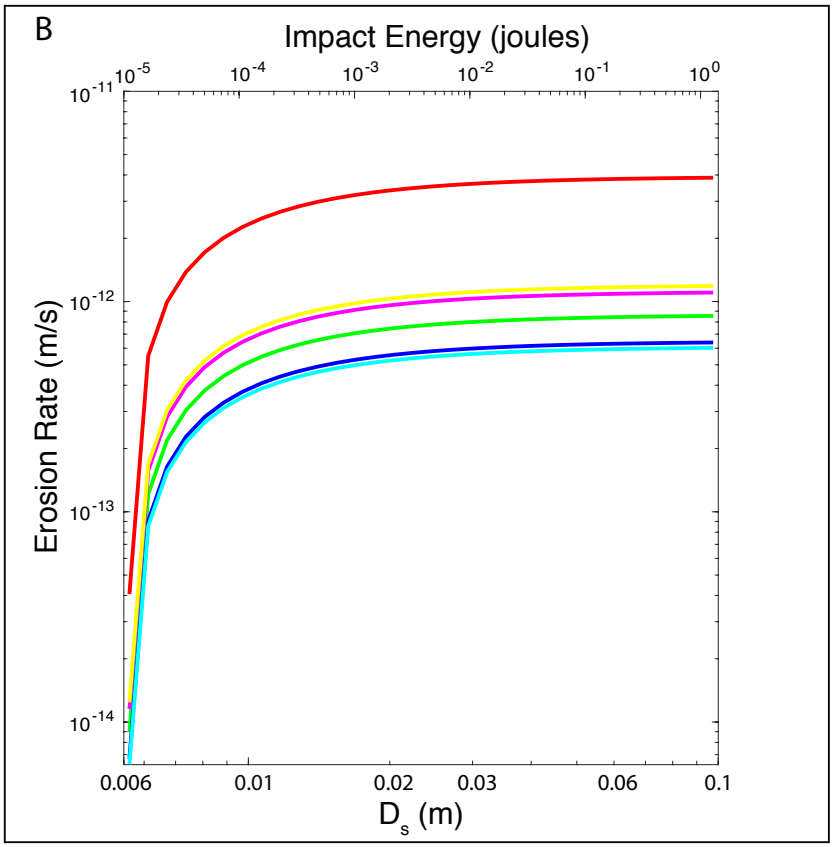
B
Impact Energy (joules)
10^-5
10^-4
10^-3
10^-2
10^-1
10^0
Erosion Rate (m/s)
10^-11
10^-12
10^-13
10^-14
0.006
0.01
0.02
0.03
0.06
0.1
D_s (m)

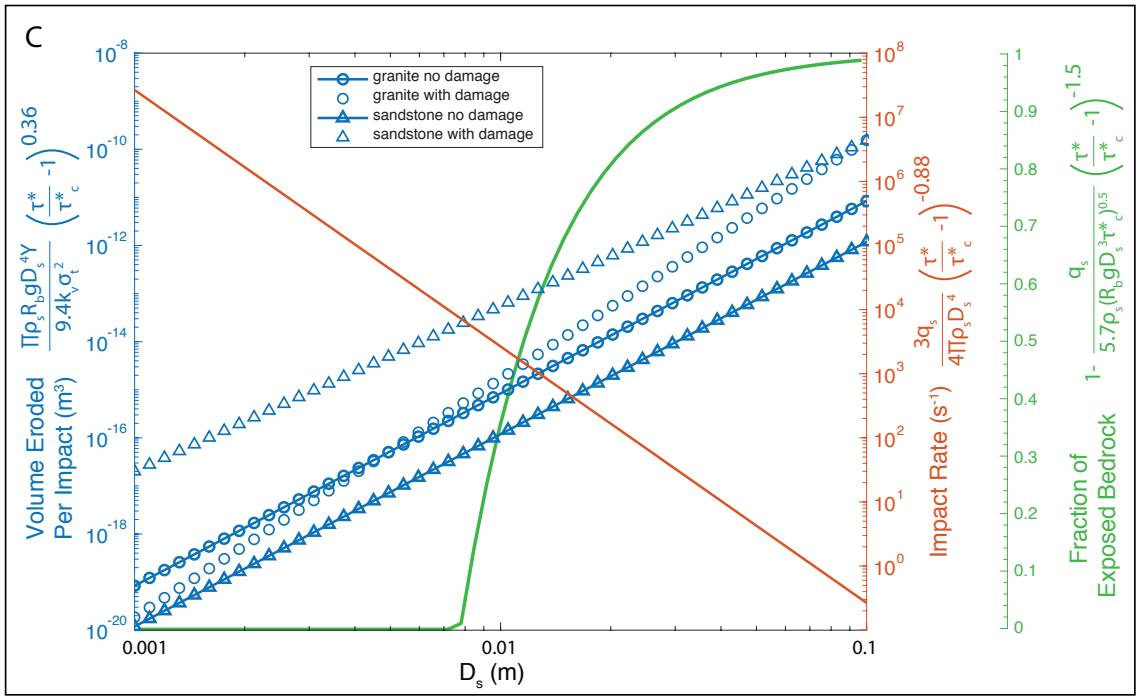

Model Inputs

$\tau^* = 0.15$	b & m (Table 2)
$\tau_c^* = 0.03$	$Y = 5e^4$ MPa
$D_s = 0.001 - 0.1$ m	$k_v = 10^6$
$q_s = 1$ kg/ms	$R_b = 1.65$
$q_t = 5.7\rho_s(R_b g D_s^3)^{0.5}(\tau^*/\tau_c^* - 1)^{1.5}$	$g = 9.81$ m/s
σ_t (Table 1)	

Figure 3.10: Changes in erosion rate with increasing bed load grain size. (A) Erosion rate of the Saltation-Abrasion model modified by equations 44-46, and (B) results using the original Saltation-Abrasion model with the median value of core tensile strength. Data is plotted in log-log space. The top *x*-axis shows the increase in impact energy that is congruent with increasing grain sizes at the same transport stage. (C) The three Saltation-Abrasion model components V_i, I_r, and F_b are plotted as a function of grain size. Model inputs listed in the table. Adding damage equations to the original model only affects the volume removed per impact (V_i).

REFERENCES

Abbott, J.E., and Francis, J.R.D., 1977, Saltation and suspension trajectories of solid grains in a water stream: Philosophical Transactions of the Royal Society of London. Series A, Mathematical and Physical Sciences, v. 284, p. 225–254.

Ahnert, F., 1970, Functional relationships between denudation, relief, and uplift in large, mid-latitude drainage basins: American Journal of Science, v. 268, p. 243–263.

Ajayi, O.O., and Ludema, K.C., 1992, The effect of microstructure on wear modes of ceramic materials: Wear, v. 154, p. 371–385.

Allen, G.H., Barnes, J.B., Pavelsky, T.M., and Kirby, E., 2013, Lithologic and tectonic controls on bedrock channel form at the northwest Himalayan front: Journal of Geophysical Research: Earth Surface, v. 118, p. 1806–1825.

Anderson, R.S., 1998, Near-surface thermal profiles in alpine bedrock: Implications for the frost weathering of rock: Arctic and Alpine Research, v. 30, p. 362–372.

Ashby, M.F., and Sammis, C.G., 1990, The damage mechanics of brittle solids in compression: Pure and Applied Geophysics, v. 133, p. 489–521.

ASTM, 2001. Standard test method for determination of rock hardness by rebound hammer method. ASTM Stand. 04.09 (D 5873-00).

ASTM D 2845- 83

Atkinson, B.K., 1984, Subcritical crack growth in geological materials: Journal of Geophysical Research: Solid Earth, v. 89, p. 4077–4114.

Attal, M., Mudd, S.M., Hurst, M.D., Weinman, B., Yoo, K., and Naylor, M., 2015, Impact of change in erosion rate and landscape steepness on hillslope and fluvial sediments grain size in the Feather River basin (Sierra Nevada, California): Earth Surface Dynamics, v. 3, p. 201–222, doi:https://doi.org/10.5194/esurf-3-201-2015.

Auel, C., Albayrak, I., Sumi, T., and Boes, R.M., 2017a, Sediment transport in high-speed flows over a fixed bed: 1. Particle dynamics: Earth Surface Processes and Landforms, v. 42, p. 1365–1383.

Auel, C., Albayrak, I., Sumi, T., and Boes, R.M., 2017b, Sediment transport in high-speed flows over a fixed bed: 2. Particle impacts and abrasion prediction: Earth Surface Processes and Landforms, v. 42, p. 1384–1396.

Baratta, F.I., 1981, Refinement of stress intensity factor estimates for a peripherally cracked spherical void and a hemispherical surface pit: Journal of the American Ceramic Society, v. 64, p. C–3.

Berthaud, Y., 1991a, Damage measurements in concrete via an ultrasonic technique. Part I experiment: Cement and concrete research, v. 21, p. 73–82.

Berthaud, Y., 1991b, Damage measurements in concrete via an ultrasonic technique part II modeling: Cement and concrete research, v. 21, p. 219–228.

Beyeler, J.D., and Sklar, L.S., 2010, Bedrock resistance to fluvial erosion: the importance of rock tensile strength, crystal grain size and porosity in scaling from the laboratory to the field, *in* AGU Fall Meeting Abstracts,.

Bitter, J.G.A., 1963a, A study of erosion phenomena part I: Wear, v. 6, p. 5–21, doi:10.1016/0043-1648(63)90003-6.

Bitter, J.G.A., 1963b, A study of erosion phenomena: Part II: Wear, v. 6, p. 169–190.

Brace, W.F., 1964, Brittle fracture of rocks, State of Stress in the Earth's Crust WR Judd, 110–178: Elsevier, New York.

Brace, W.F., 1961, Dependence of fracture strength of rocks on grain size, *in* The 4th US Symposium on Rock Mechanics (USRMS), American Rock Mechanics Association.

Bradley, D.N., Tucker, G.E., and Benson, D.A., 2018, Fractional dispersion in a sand bed river: Journal of Geophysical Research: Earth Surface, doi:10.1029/2009JF001268@10.1002/(ISSN)2169-9011.SCALING1.

Bradshaw, P., and Wong, F.Y.F., 1972, The reattachment and relaxation of a turbulent shear layer: Journal of Fluid Mechanics, v. 52, p. 113–135.

Budetta, P., De Riso, R., and De Luca, C., 2001, Correlations between jointing and seismic velocities in highly fractured rock masses: Bulletin of Engineering Geology and the Environment, v. 60, p. 185–192.

Budwig, R., and Goodwin, P., 2012, The center for ecohydraulics research mountain streamlab-A facility for collaborative research and education: Innovations 2012: World innovations in engineering education and research, p. 17–28.

Bursztyn, N., Pederson, J.L., Tressler, C., Mackley, R.D., and Mitchell, K.J., 2015, Rock strength along a fluvial transect of the Colorado Plateau–quantifying a fundamental control on geomorphology: Earth and Planetary Science Letters, v. 429, p. 90–100.

Chaboche, J.-L., 1988, Continuum damage mechanics: Part I—General concepts: Journal of applied mechanics, v. 55, p. 59–64.

Chatanantavet, P., 2007, Physically-based models of bedrock incision processes in mountain streams:

Chatanantavet, P., and Parker, G., 2009, Physically based modeling of bedrock incision by abrasion, plucking, and macroabrasion: J. Geophys. Res, v. 114, p. F04018.

Clair, J.S., Moon, S., Holbrook, W.S., Perron, J.T., Riebe, C.S., Martel, S.J., Carr, B., Harman, C., Singha, K., and Richter, D. deB, 2015a, Geophysical imaging reveals topographic stress

control of bedrock weathering: Science, v. 350, p. 534–538, doi:10.1126/science.aab2210.

Clair, J.S., Moon, S., Holbrook, W.S., Perron, J.T., Riebe, C.S., Martel, S.J., Carr, B., Harman, C., Singha, K., and Richter, D. deB, 2015b, Geophysical imaging reveals topographic stress control of bedrock weathering: Science, v. 350, p. 534–538.

Clarke, B.A., and Burbank, D.W., 2011, Quantifying bedrock-fracture patterns within the shallow subsurface: Implications for rock mass strength, bedrock landslides, and erodibility: J. Geophys. Res, v. 116, p. F04009.

Collins, B.D., Montgomery, D.R., Schanz, S.A., and Larsen, I.J., 2016, Rates and mechanisms of bedrock incision and strath terrace formation in a forested catchment, Cascade Range, Washington: Bulletin, v. 128, p. 926–943.

Collins, B.D., and Stock, G.M., 2016, Rockfall triggering by cyclic thermal stressing of exfoliation fractures: Nature Geoscience, v. 9, p. 395.

Cook, R.F., and Pharr, G.M., 1990, Direct observation and analysis of indentation cracking in glasses and ceramics: Journal of the American Ceramic Society, v. 73, p. 787–817.

Davidge, R.W., 1979, Mechanical behaviour of ceramics: CUP Archive.

Davidge, R.W., and Riley, F.L., 1995, Grain-size dependence of the wear of alumina: Wear, v. 186, p. 45–49.

Dietrich, R.V., 1977, Impact abrasion of harder by softer materials: The Journal of Geology, v. 85, p. 242–246.

Diplas, P., Dancey, C.L., Celik, A.O., Valyrakis, M., Greer, K., and Akar, T., 2008, The role of impulse on the initiation of particle movement under turbulent flow conditions: Science, v. 322, p. 717–720.

Draebing, D., Krautblatter, M., and Hoffmann, T., 2017, Thermo-cryogenic controls of fracture kinematics in permafrost rockwalls: Geophysical Research Letters, v. 44, p. 3535–3544.

Duvall, A., Kirby, E., and Burbank, D., 2004, Tectonic and lithologic controls on bedrock channel profiles and processes in coastal California: Journal of Geophysical Research: Earth Surface, v. 109.

Einstein, H.A., 1950, The bed-load function for sediment transportation in open channel flows.:

El-Raghy, T., Blau, P., and Barsoum, M.W., 2000, Effect of grain size on friction and wear behavior of Ti3SiC2: Wear, v. 238, p. 125–130.

Engel, P.A., 1978, Impact Wear of Materials: Elsevier, 356 p.

Eppes, M.C., Hancock, G.S., Chen, X., Arey, J., Dewers, T., Huettenmoser, J., Kiessling, S., Moser, F., Tannu, N., and Weiserbs, B., 2018, Rates of subcritical cracking and long-term rock erosion: Geology, v. 46, p. 951–954.

Eppes, M.-C., and Keanini, R., 2017, Mechanical Weathering and Rock Erosion by Climate-Dependent Subcritical Cracking: Reviews of Geophysics,.

Eppes, M.C., Magi, B., Hallet, B., Delmelle, E., Mackenzie-Helnwein, P., Warren, K., and Swami, S., 2016, Deciphering the role of solar-induced thermal stresses in rock weathering: Bulletin, v. 128, p. 1315–1338.

Ericson, K., 2004, Geomorphological surfaces of different age and origin in granite landscapes: an evaluation of the Schmidt hammer test: Earth Surface Processes and Landforms, v. 29, p. 495–509.

Fathel, S.L., Furbish, D.J., and Schmeeckle, M.W., 2015, Experimental evidence of statistical ensemble behavior in bed load sediment transport: Journal of Geophysical Research: Earth Surface, v. 120, p. 2298–2317.

Fernandez Luque, R., and Van Beek, R., 1976, Erosion and transport of bed-load sediment: Journal of hydraulic research, v. 14, p. 127–144.

Finnegan, N.J., Klier, R.A., Johnstone, S., Pfeiffer, A.M., and Johnson, K., 2017, Field evidence for the control of grain size and sediment supply on steady-state bedrock river channel slopes in a tectonically active setting: Earth Surface Processes and Landforms, v. 42, p. 2338–2349.

Finnegan, N.J., Roe, G., Montgomery, D.R., and Hallet, B., 2005, Controls on the channel width of rivers: Implications for modeling fluvial incision of bedrock: Geology, v. 33, p. 229–232.

Finnegan, N.J., Sklar, L.S., and Fuller, T.K., 2007, Interplay of sediment supply, river incision, and channel morphology revealed by the transient evolution of an experimental bedrock channel: J. Geophys. Res, v. 112, p. F03S11.

Finnie, I., 1960, Erosion of surfaces by solid particles: wear, v. 3, p. 87–103.

Flint, J.J., 1974, Stream gradient as a function of order, magnitude, and discharge: Water Resources Research, v. 10, p. 969–973.

Foley, M.G., 1980, Bed-rock incision by streams: Geological Society of America Bulletin, v. 91, p. 2189–2213.

Forte, A.M., Yanites, B.J., and Whipple, K.X., 2016, Complexities of landscape evolution during incision through layered stratigraphy with contrasts in rock strength: Earth Surface Processes and Landforms, v. 41, p. 1736–1757.

Francis, J.R.D., 1973, Experiments on the motion of solitary grains along the bed of a water-stream: Proceedings of the Royal Society of London. A. Mathematical and Physical Sciences, v. 332, p. 443–471.

Franklin, J.A., and Chandra, R., 1972, The slake-durability test, *in* International Journal of Rock Mechanics and Mining Sciences & Geomechanics Abstracts, Elsevier, v. 9, p. 325–328.

Fredrich, J.T., Evans, B., and Wong, T.-F., 1990, Effect of grain size on brittle and semibrittle strength: Implications for micromechanical modelling of failure in compression: Journal of Geophysical Research: Solid Earth, v. 95, p. 10907–10920.

Furbish, D.J., Haff, P.K., Roseberry, J.C., and Schmeeckle, M.W., 2012, A probabilistic description of the bed load sediment flux: 1. Theory: Journal of Geophysical Research: Earth Surface, v. 117.

Ganti, V., Meerschaert, M.M., Foufoula-Georgiou, E., Viparelli, E., and Parker, G., 2010, Normal and anomalous diffusion of gravel tracer particles in rivers: Journal of Geophysical Research: Earth Surface, v. 115.

Gilbert, G.K., 1877, Report on the geology of the Henry Mountains: Dept. of the Interior, U.S. Geographical and Geological Survey of the Rocky Mountain Region, 236 p.

Gischig, V.S., Moore, J.R., Evans, K.F., Amann, F., and Loew, S., 2011, Thermomechanical forcing of deep rock slope deformation: 2. The Randa rock slope instability: Journal of Geophysical Research: Earth Surface, v. 116.

Goudie, A.S., 2006, The Schmidt Hammer in geomorphological research: Progress in Physical Geography, v. 30, p. 703–718.

Grady, D.E., and Kipp, M.E., 1979, The micromechanics of impact fracture of rock, *in* International Journal of Rock Mechanics and Mining Sciences & Geomechanics Abstracts, Elsevier, v. 16, p. 293–302, http://www.sciencedirect.com/science/article/pii/0148906279902407 (accessed September 2017).

Hack, J.T., 1957, Studies of longitudinal stream profiles in Virginia and Maryland: US Government Printing Office, v. 294.

Hadley, K., 1976, Comparison of calculated and observed crack densities and seismic velocities in Westerly granite: Journal of Geophysical Research, v. 81, p. 3484–3494.

Hancock, G.S., Anderson, R.S., and Whipple, K.X., 1998, Beyond Power: Bedrock River Incision Process and Form:

Hancock, G.S., Small, E.E., and Wobus, C., 2011, Modeling the effects of weathering on bedrock-floored channel geometry: J. Geophys. Res, v. 116, p. F03018.

Harkins, N., Kirby, E., Heimsath, A., Robinson, R., and Reiser, U., 2007, Transient fluvial incision in the headwaters of the Yellow River, northeastern Tibet, China: Journal of Geophysical Research: Earth Surface, v. 112.

Hill, K.M., DellAngelo, L., and Meerschaert, M.M., 2010, Heavy-tailed travel distance in gravel bed transport: An exploratory enquiry: Journal of Geophysical Research: Earth Surface, v. 115.

Hoke, G.D., and Turcotte, D.L., 2002, Weathering and damage: Journal of Geophysical Research: Solid Earth, v. 107.

Howard, A.D., 1988, Equilibrium models in geomorphology: Modelling geomorphological systems, p. 49–72.

Hu, C., and Hui, Y., 1996, Bed-load transport. II: Stochastic characteristics: Journal of Hydraulic Engineering, v. 122, p. 255–261.

Huda, S.A., and Small, E.E., 2014, Modeling the effects of bed topography on fluvial bedrock erosion by saltating bed load: Journal of Geophysical Research: Earth Surface, v. 119, p. 1222–1239.

Hult, J., 1979, CDM - CAPABILITIES, LIMITATIONS AND PROMISES, *in* Easterling, K.E. ed., Mechanisms of Deformation and Fracture, Pergamon, p. 233–247, doi:10.1016/B978-0-08-024258-3.50025-4.

Hutchings, I.M., 1987, Wear by particulates: Chemical Engineering Science, v. 42, p. 869–878.

ISHIBASHI, T., 1983, A hydraulic study on protection for erosion of sediment flush equipments of dams, *in* Proceedings of the Japan Society of Civil Engineers, Japan Society of Civil Engineers, v. 1983, p. 103–112.

Johnson, K.N., and Finnegan, N.J., 2015a, A lithologic control on active meandering in bedrock channels: Bulletin, v. 127, p. 1766–1776.

Johnson, K.N., and Finnegan, N.J., 2015b, A lithologic control on active meandering in bedrock channels: Bulletin, v. 127, p. 1766–1776.

Johnson, J.P.L., and Whipple, K.X., 2010, Evaluating the controls of shear stress, sediment supply, alluvial cover, and channel morphology on experimental bedrock incision rate: J. Geophys. Res, v. 115, p. F02018.

Johnson, J.P., and Whipple, K.X., 2007, Feedbacks between erosion and sediment transport in experimental bedrock channels:

Johnson, J.P., Whipple, K.X., Sklar, L.S., and Hanks, T.C., 2009, Transport slopes, sediment cover, and bedrock channel incision in the Henry Mountains, Utah: Journal of Geophysical Research: Earth Surface, v. 114.

Kachanov, L., 1958, Rupture time under creep conditions: Izv. Akad. Nauk SSSR, v. 8, p. 26–31.

Kirby, E., and Whipple, K.X., 2012, Expression of active tectonics in erosional landscapes: Journal of Structural Geology, v. 44, p. 54–75.

Kirby, E., and Whipple, K., 2001, Quantifying differential rock-uplift rates via stream profile analysis: Geology, v. 29, p. 415–418, doi:10.1130/0091-7613(2001)029<0415:QDRURV>2.0.CO;2.

Lamb, M.P., and Dietrich, W.E., 2009, The persistence of waterfalls in fractured rock: Geological Society of America Bulletin, v. 121, p. 1123–1134.

Lamb, M.P., Dietrich, W.E., and Sklar, L.S., 2008, A model for fluvial bedrock incision by impacting suspended and bed load sediment: J. Geophys. Res, v. 113, p. F03025.

Lamb, M.P., Finnegan, N.J., Scheingross, J.S., and Sklar, L.S., 2015, New insights into the mechanics of fluvial bedrock erosion through flume experiments and theory:

Lawn, B.R., Evans, A.G., and Marshall, D.B., 1980, Elastic/plastic indentation damage in ceramics: the median/radial crack system: Journal of the American Ceramic Society, v. 63, p. 574–581.

Lawn, B.R., and Fuller, E.R., 1975, Equilibrium penny-like cracks in indentation fracture: Journal of Materials Science, v. 10, p. 2016–2024.

Lee, H.-Y., and Hsu, I.-S., 1994, Investigation of saltating particle motions: Journal of Hydraulic Engineering, v. 120, p. 831–845.

Leith, K., Moore, J.R., Amann, F., and Loew, S., 2014, In situ stress control on microcrack generation and macroscopic extensional fracture in exhuming bedrock: Journal of Geophysical Research: Solid Earth, v. 119, p. 594–615.

Lemaitre, J., and Dufailly, J., 1987, Damage measurements: Engineering Fracture Mechanics, v. 28, p. 643–661.

Leopold, L.B., and Maddock, T., 1953, The hydraulic geometry of stream channels and some physiographic implications: US Government Printing Office, v. 252.

Leucci, G., and De Giorgi, L., 2006, Experimental studies on the effects of fracture on the P and S wave velocity propagation in sedimentary rock (“Calcarenite del Salento”): Engineering Geology, v. 84, p. 130–142.

Limaye, A.B., and Lamb, M.P., 2014, Numerical simulations of bedrock valley evolution by meandering rivers with variable bank material: Journal of Geophysical Research: Earth Surface, v. 119, p. 927–950.

Maridet, C., Joder, C., and Vincent, A., 1986, Measurement of the Speed of Ultrasonic Waves. Application to the Characterization of Materials: Mater. Tech.(Paris), v. 74, p. 439–442.

Marshall, D.B., Lawn, B.R., and Evans, A.G., 1982, Elastic/plastic indentation damage in ceramics: the lateral crack system: Journal of the American Ceramic Society, v. 65, p. 561–566.

Marshall, J.A., and Roering, J.J., 2014, Diagenetic variation in the Oregon Coast Range: Implications for rock strength, soil production, hillslope form, and landscape evolution: Journal of Geophysical Research: Earth Surface, v. 119, p. 1395–1417.

Martin, R.L., Jerolmack, D.J., and Schumer, R., 2012, The physical basis for anomalous diffusion in bed load transport: Journal of Geophysical Research: Earth Surface, v. 117.

Matsuoka, N., and Murton, J., 2008, Frost weathering: recent advances and future directions: Permafrost and Periglacial Processes, v. 19, p. 195–210.

Mayer, L., 1979, Evolution of the Mogollon Rim in central Arizona: Tectonophysics, v. 61, p. 49–62.

McCarroll, D., 1991, The Schmidt hammer, weathering and rock surface roughness: Earth Surface Processes and Landforms, v. 16, p. 477–480.

McFadden, L.D., Eppes, M.C., Gillespie, A.R., and Hallet, B., 2005, Physical weathering in arid landscapes due to diurnal variation in the direction of solar heating: Geological Society of America Bulletin, v. 117, p. 161, doi:10.1130/B25508.1.

Meredith, P.G., 1990, Fracture and failure of brittle polycrystals: an overview, *in* Barber, D.J. and Meredith, P.G. eds., Deformation Processes in Minerals, Ceramics and Rocks, Dordrecht, Springer Netherlands, The Mineralogical Society Series, p. 5–47, doi:10.1007/978-94-011-6827-4_2.

Miller, J.R., 1991, The Influence of Bedrock Geology on Knickpoint Development and Channel-Bed Degradation along Downcutting Streams in South-Central Indiana: The Journal of Geology, p. 591–605.

Molnar, P., 2004, Interactions among topographically induced elastic stress, static fatigue, and valley incision: Journal of Geophysical Research: Earth Surface, v. 109, p. F02010, doi:10.1029/2003JF000097.

Molnar, P., Anderson, R.S., and Anderson, S.P., 2007, Tectonics, fracturing of rock, and erosion: J. Geophys. Res, v. 112, p. F03014.

Montgomery, D.R., 2004, Observations on the role of lithology in strath terrace formation and bedrock channel width: American Journal of Science, v. 304, p. 454–476, doi:10.2475/ajs.304.5.454.

Montgomery, D.R., and Gran, K.B., 2001, Downstream variations in the width of bedrock channels: Water Resources Research, v. 37, p. 1841–1846.

Morisawa, M.E., 1962, Quantitative geomorphology of some watersheds in the Appalachian Plateau: Geological Society of America Bulletin, v. 73, p. 1025–1046.

Mudd, S.M., Attal, M., Milodowski, D.T., Grieve, S.W., and Valters, D.A., 2014, A statistical framework to quantify spatial variation in channel gradients using the integral method of channel profile analysis: Journal of Geophysical Research (Earth Surface), v. 119, p. 138–152.

Murphy, B.P., Johnson, J.P., Gasparini, N.M., Hancock, G.S., and Small, E.E., 2018, Weathering and abrasion of bedrock streambed topography: Geology, v. 46, p. 459–462.

Murphy, B.P., Johnson, J.P., Gasparini, N.M., and Sklar, L.S., 2016, Chemical weathering as a mechanism for the climatic control of bedrock river incision: Nature, v. 532, p. 223.

Nelson, J.M., Shreve, R.L., McLean, S.R., and Drake, T.G., 1995, Role of near-bed turbulence structure in bed load transport and bed form mechanics: Water resources research, v. 31, p. 2071–2086.

Newman, M.E., 2005, Power laws, Pareto distributions and Zipf's law: Contemporary physics, v. 46, p. 323–351.

Niedzielski, T., Migoń, P., and Placek, A., 2009, A minimum sample size required from Schmidt hammer measurements: Earth Surface Processes and Landforms: The Journal of the British Geomorphological Research Group, v. 34, p. 1713–1725.

Nikora, V., Habersack, H., Huber, T., and McEwan, I., 2002, On bed particle diffusion in gravel bed flows under weak bed load transport: Water Resources Research, v. 38, p. 17–1.

Niño, Y., García, M., and Ayala, L., 1994, Gravel saltation: 1. experiments: Water resources research, v. 30, p. 1907–1914.

Oka, Y.I., Ohnogi, H., Hosokawa, T., and Matsumura, M., 1997, The impact angle dependence of erosion damage caused by solid particle impact: Wear, v. 203, p. 573–579.

Olsson, W.A., 1974, Grain size dependence of yield stress in marble: Journal of Geophysical Research, v. 79, p. 4859–4862.

Ott, R.F., Whipple, K.X., and van Soest, M., 2018, Incision history of the Verde Valley region and implications for uplift of the Colorado Plateau (central Arizona): Geosphere, v. 14, p. 1690–1709.

Papanicolaou, A.N., Diplas, P., Dancey, C.L., and Balakrishnan, M., 2001, Surface roughness effects in near-bed turbulence: Implications to sediment entrainment: Journal of Engineering Mechanics, v. 127, p. 211–218.

Peng, S., and Johnson, A.M., 1972, Crack growth and faulting in cylindrical specimens of Chelmsford granite, *in* International Journal of Rock Mechanics and Mining Sciences & Geomechanics Abstracts, Elsevier, v. 9, p. 37–86.

Perne, M., Covington, M.D., Thaler, E.A., and Myre, J.M., 2017, Steady state, erosional continuity, and the topography of landscapes developed in layered rocks: Earth Surface Dynamics, v. 5, p. 85.

Perron, J.T., and Royden, L., 2013, An integral approach to bedrock river profile analysis: Earth Surf. Process. Landforms, v. 38, p. 570–576.

Richardson, K., and Carling, P., 2005, A typology of sculpted forms in open bedrock channels: Geological Society of America, v. 392.

Ritter, J.E., 1985, Erosion damage in structural ceramics: Materials science and engineering, v. 71, p. 195–201.

Seidl, M.A., Dietrich, W.E., and Kirchner, J.W., 1994, Longitudinal profile development into bedrock: An analysis of Hawaiian channels: The Journal of Geology, v. 102, p. 457–474.

Sekine, M., and Kikkawa, H., 1992, Mechanics of saltating grains. II: Journal of Hydraulic Engineering, v. 118, p. 536–558.

Selby, M.J., 1993, Hillslope Materials and Processes Oxford Univ. Press: Oxford.

Shah, S.P., and Chandra, S., 1970, Fracture of Concrete Subjected to Cyclic and Sustained Loading: Journal Proceedings, v. 67, p. 816–827, doi:10.14359/7312.

Shobe, C.M., Hancock, G.S., Eppes, M.C., and Small, E.E., 2017, Field evidence for the influence of weathering on rock erodibility and channel form in bedrock rivers: Earth Surface Processes and Landforms, v. 42, p. 1997–2012.

Simpson, R.L., 1989, Turbulent boundary-layer separation: Annual Review of Fluid Mechanics, v. 21, p. 205–232.

Sklar, L.S., and Dietrich, W.E., 2004, A mechanistic model for river incision into bedrock by saltating bed load: Water Resour. Res, v. 40, p. W06301.

Sklar, L.S., and Dietrich, W.E., 2001, Sediment and rock strength controls on river incision into bedrock: GEOLOGY,.

Sklar, L.S., and Dietrich, W.E., 2006, The role of sediment in controlling steady-state bedrock channel slope: Implications of the saltation–abrasion incision model: Geomorphology, v. 82, p. 58–83.

Sklar, L.S., Riebe, C.S., Marshall, J.A., Genetti, J., Leclere, S., Lukens, C.L., and Merces, V., 2017, The problem of predicting the size distribution of sediment supplied by hillslopes to rivers: Geomorphology, v. 277, p. 31–49.

Small, E.E., Blom, T., Hancock, G.S., Hynek, B.M., and Wobus, C.W., 2015, Variability of rock erodibility in bedrock-floored stream channels based on abrasion mill experiments: J. Geophys. Res. Earth Surf, v. 120, p. 2.

Sprunt, E.S., and Brace, W.F., 1974, Direct observation of microcavities in crystalline rocks, *in* International Journal of Rock Mechanics and Mining Sciences & Geomechanics Abstracts, Elsevier, v. 11, p. 139–150.

Stark, C.P., 2006, A self-regulating model of bedrock river channel geometry: Geophysical Research Letters, v. 33.

Stock, G.M., Martel, S.J., Collins, B.D., and Harp, E.L., 2012, Progressive failure of sheeted rock slopes: the 2009–2010 Rhombus Wall rock falls in Yosemite Valley, California, USA: Earth Surface Processes and Landforms, v. 37, p. 546–561.

Stock, J.D., and Montgomery, D.R., 1999, Geologic constraints on bedrock river incision using the stream power law: Journal of Geophysical Research: Solid Earth, v. 104, p. 4983–4993.

Stock, J.D., Montgomery, D.R., Collins, B.D., Dietrich, W.E., and Sklar, L., 2005, Field measurements of incision rates following bedrock exposure: Implications for process controls on the long profiles of valleys cut by rivers and debris flows: Geological Society of America Bulletin, v. 117, p. 174–194, doi:10.1130/B25560.1.

Tapponnier, P., and Brace, W.F., 1976, Development of stress-induced microcracks in Westerly Granite, *in* International Journal of Rock Mechanics and Mining Sciences & Geomechanics Abstracts, Elsevier, v. 13, p. 103–112.

Turowski, J.M., Böckli, M., Rickenmann, D., and Beer, A.R., 2013, Field measurements of the energy delivered to the channel bed by moving bed load and links to bedrock erosion: Journal of Geophysical Research: Earth Surface, v. 118, p. 2438–2450.

Turowski, J.M., Lague, D., and Hovius, N., 2007, Cover effect in bedrock abrasion: A new derivation and its implications for the modeling of bedrock channel morphology: Journal of Geophysical Research: Earth Surface, v. 112.

Viles, H., Goudie, A., Grab, S., and Lalley, J., 2011, The use of the Schmidt Hammer and Equotip for rock hardness assessment in geomorphology and heritage science: a comparative analysis: Earth Surface Processes and Landforms, v. 36, p. 320–333, doi:10.1002/esp.2040.

Walder, J., and Hallet, B., 1985, A theoretical model of the fracture of rock during freezing: Geological Society of America Bulletin, v. 96, p. 336–346.

Warke, P.A., and Smith, B.J., 1998, Effects of direct and indirect heating on the validity of rock weathering simulation studies and durability tests: Geomorphology, v. 22, p. 347–357.

Wellman, R.G., and Allen, C., 1995, The effects of angle of impact and material properties on the erosion rates of ceramics: Wear, v. 186, p. 117–122.

Whipple, K.X., 2004, Bedrock Rivers and the Geomorphology of Active Orogens: Annual Review of Earth and Planetary Sciences, v. 32, p. 151–185, doi:10.1146/annurev.earth.32.101802.120356.

Whipple, K.X., Hancock, G.S., and Anderson, R.S., 2000, River incision into bedrock: Mechanics and relative efficacy of plucking, abrasion, and cavitation: Geological Society of America Bulletin, v. 112, p. 490–503.

Whipple, K.X., Kirby, E., and Brocklehurst, S.H., 1999, Geomorphic limits to climate-induced increases in topographic relief: Nature, v. 401, p. 39.

Whipple, K.X., and Tucker, G.E., 1999, Dynamics of the stream-power river incision model: Implications for height limits of mountain ranges, landscape response timescales, and research needs: JOURNAL OF GEOPHYSICAL RESEARCH, v. 104, p. 17–661.

Wiberg, P.L., and Smith, J.D., 1985, A theoretical model for saltating grains in water: Journal of Geophysical Research: Oceans, v. 90, p. 7341–7354.

Wilson, A., and Lavé, J., 2014, Convergent evolution of abrading flow obstacles: Insights from analogue modelling of fluvial bedrock abrasion by coarse bedload: Geomorphology, v. 208, p. 207–224.

Wobus, C., Whipple, K.X., Kirby, E., Snyder, N., Johnson, J., Spyropolou, K., Crosby, B., and Sheehan, D., 2006, Tectonics from topography: Procedures, promise, and pitfalls: Geological Society of America Special Papers, v. 398, p. 55–74, doi:10.1130/2006.2398(04).

Wohl, E.E., 1993, Bedrock channel incision along Piccaninny Creek, Australia: The Journal of Geology, v. 101, p. 749–761.

Wohl, E., 2008, The effect of bedrock jointing on the formation of straths in the Cache la Poudre River drainage, Colorado Front Range: Journal of Geophysical Research: Earth Surface, v. 113.

Wohl, E., and Achyuthan, H., 2002, Substrate influences on incised-channel morphology: The Journal of geology, v. 110, p. 115–120.

Wohl, E.E., and Merritt, D.M., 2001, Bedrock channel morphology: Geological Society of America Bulletin, v. 113, p. 1205–1212.

Woldman, M., van der Heide, E., Schipper, D.J., Tinga, T., and Masen, M.A., 2012, Investigating the influence of sand particle properties on abrasive wear behaviour: Wear, v. 294, p. 419–426.

Wolman, M.G., 1954, A method of sampling coarse river-bed material: EOS, Transactions American Geophysical Union, v. 35, p. 951–956.

Wong, R.H., Chau, K.T., and Wang, P., 1996, Microcracking and grain size effect in Yuen Long marbles, *in* International journal of rock mechanics and mining sciences & geomechanics abstracts, Elsevier, v. 33, p. 479–485.

Yanites, B.J., Mitchell, N.A., Bregy, J.C., Carlson, G.A., Cataldo, K., Holahan, M., Johnston, G.H., Nelson, A., Valenza, J., and Wanker, M., 2018, Landslides control the spatial and temporal variation of channel width in southern Taiwan: Implications for landscape evolution and cascading hazards in steep, tectonically active landscapes: Earth Surface Processes and Landforms, v. 43, p. 1782–1797.

Yanites, B.J., and Tucker, G.E., 2010, Controls and limits on bedrock channel geometry: Journal of Geophysical Research, v. 115, p. 17 PP., doi:201010.1029/2009JF001601.

Yanites, B.J., Tucker, G.E., Mueller, K.J., Chen, Y.-G., Wilcox, T., Huang, S.-Y., and Shi, K.-W., 2010, Incision and channel morphology across active structures along the Peikang River, central Taiwan: Implications for the importance of channel width: Bulletin, v. 122, p. 1192–1208.

CHAPTER 5: CONCLUSION

This dissertation highlights the importance bedrock properties for river incision and landscape evolution. Each chapter ultimately concludes that basin scale processes depend on granular scale properties of the substrate. In chapter two I showed that the energy delivered to the bed is highly sensitive to centimeter scale topography of the bed surface. The non-planar bed surface altered the trajectory of sediment in such a way that increased the likelihood of extremely efficient sediment impacts. This work highlights the need for a probabilistic consideration of sediment motions for natural bedrock channels, which typically have non-planar bed topography. In chapter three, I showed that the morphology of several bedrock reaches in central Arizona is well described by the resistance of the bedrock to detachment processes of abrasion and plucking as well as the mobility of sediment in the channel. While the resistance to sediment motion may have had the strongest overall control on channel morphology (of the parameters considered in this dissertation), the correlation of morphology to the resistance to bedrock detachment was non trivial. This suggests that bedrock properties of the rock mass as well as the spacing of discontinuities on the channel surface play a significant role in the adjustment of channels to changing boundary conditions. In chapter four, I showed that the accumulation of micro-scale discontinuities caused by chemical weathering and bed load impacts varies for different rock types. Based on crystalline grain size, crystalline grain structure, and mineralogy of the bedrock material some rock types are more susceptible to chemical weathering and some are more susceptible to impact damage. The rock types more susceptible to chemical weathering were more damaged on downstream facing channel surfaces than upstream facing channel surfaces suggesting that as impact energy increases the strength of these bedrock surfaces also increases as fresher rock is exposed. The rock types that are more susceptible to impact fracturing were more damaged on the upstream facing channel

surfaces than downstream facing channel surfaces suggesting that as impact energy increases the strength of these bedrock surfaces decreases.

The findings in this dissertation imply that the efficiency of bedrock erosion depends on a complex interaction between granular properties of bedrock, climate driven chemical weathering, and the characteristic energy of bed load impacts, which could vary according to many factors such as bed surface topography or properties of impactors. The complex interaction between these factors is likely one of the underlying reasons that bedrock erodibility remains a 'black box'.

A key challenge in fluvial geomorphology is understanding the evolution of the topography of the channel bed surface, or channel roughness, through time. Channel bed roughness is a first order control on the local flow velocity, the energy of bed load impacts, and sediment transport dynamics of a stream, but is often assumed to have a typical value for bedrock streams (i.e. Manning's roughness coefficient) or neglected entirely in bedrock incision models. The work within this dissertation provides a path to develop models that account for the evolution of local bed topography that includes affects of bed roughness on abrasion rate as well as the influence of bedrock crystalline properties and the climate driven chemical weathering rate of the environment on the channel surface topography. Additional flume experiments could provide further information on the bed roughness dependent scaling of erosive energy across a range of bed shear stress. Laboratory impact experiments that measure the rate and length of microcracks for different rock types is a necessary step to calibrate the relationship between

crystalline grain size and impact damage. A simple method would be to vary the number of impacts and the energy per impact, and then examine microcracking of the surface with thin sections. Further studies such as these could establish links between channel bed roughness, river incision processes, and climate driven chemical weathering.

APPENDIX

This appendix includes two tables in support of chapter three. Table A.1 contains various rock mechanics properties as well as the mean and standard deviations for the distributions of uniaxial strength values and P-wave speed of core samples. Table A.2 contains the values for each sample. In our analyses, we characterize the strength of intact rock at depths greater than 5 cm to avoid biases in strength due to weathering, although we have not attempted to determine the degree of weathering beyond qualitative means. Tensile strength (UTS) is measured using the Brazilian splitting method on 45 mm diameter discs with a thickness of 20mm. Discs are placed on edge between platens and compressed uniaxially. The uniaxial compressive strength (UCS) was measured on core samples of 4.5 cm diameter and between 6 and 10 cm length. These tests measure the stress and strain during monotonic loading of the sample. All tests were performed under a constant strain rate of 0.00002 m/s. The strength of each sample was measured as the peak stress prior to failure. The young's modulus of each compressive strength test was estimated as the linear portion slope of the stress-strain relationship. Rock samples for these tests and others were collected from field sites either by prying blocks of bedrock from the riverbed or cut out using a gas powered 15cm barrel coring drill. Tests are performed at the University of Idaho on an MTS810 with Flex Test SE system.

Slake durability is a measurement of the resistance to degradation when subject to cycles of wetting and drying (Franklin and Chandra, 1972). The primary mechanism of degradation is related to swelling of the rock. Slaking is intensified in weaker rocks with more pore space percentage of clay minerals, a byproduct of weathering. In these slake durability tests, the broken samples from tensile strength tests were gathered for each layer and broken into ~1cm^3

aggregate. The aggregate was weighed, tumbled in water, dried, and re-weighed through 3 cycles. During tumbling, vibrations enhance water seepage into clays that then expand causing small particles slake off and fall through the mesh of the tumbling drum. The percent of mass retained is the slake durability index, which will indicate changes in erodibilty due to clay mineralization and wetting and drying.

The crystalline grain size, porosity, and density were measured on small samples (1 cm^3) representative of each rock type. The mean crystalline grain size was measured by placing a grid with nodes spacing of 0.5 mm spacing over images of thin sections. We measured the intermediate axis length of the grains that nodes landed on. From the distribution of grain sizes we report the mean grain size and standard deviation. Porosity was estimated as the difference in weight between oven dried samples and water saturated samples. Each sample was submerged in water for 24 hr and weighed. The sample was then oven dried for 24 hr and re-weighed. Density was measured from the mass of and volume displacement of small, roughly 1 cm^3 samples of each rock type.

Table A.1: Rock Property Statistical Summary

Table A.1: Rock Properties Statistics

rock type	Porosity %	Density (kg/m^3)	Slake Durability	UTS (Mpa)	std of UTS (Mpa)	UCS of (Mpa)	std of UCS (Mpa)	Young's Modulus (Mpa)	std of Young's Modulus (Mpa)	P-wave Velocity of Cores (m/s)	std of P-Wave Velocity of Cores	Crystalline Grain Size (mm)	ε_v	D_{16} (m)	D_{50} (m)
quartzite	0.33	2803	0.244	14.94	5.77	155.16	52.52	10815	3361	6212	288	0.07	9.31E+07		
granodiorite	0.23	2820	0.329	19.20	5.15	106.64	75.85	12520	2787	6085	160	1.98	1.93E+07	1	1
marble	1.37	2756	0.460	12.54	4.45	97.92	23.19	8948	960	5968	134	0.0111	2.00E+07		
greenstone	0.70	2917	0.869	10.6	4.47	70.75	39.87	11317	1162	5400	660	0.0889	4.33E+06	2	8.5
granite	0.54	2633	6.375	5.45	1.46	70.76	13.16	6945	1270	3090	468	2.162	5.74E+06	1	10
rhyolite	0.95	2732	0.911	9.72	4.02	82.46	36.11	9815	4148	3288	688	0.463	5.88E+06		
phyllite	0.27	2572	1.151	13.96	2.63	75.95	37.58	7532	3513	5015	389	0.0341	2.94E+06	2	32
basalt	1.09	2464	1.313	12.91	3.44	114.97	38.2	14754	3765	5113	209	0.0621	3.86E+06	1	43
vesicular basalt	1.41	2345	1.435	5.34	1.22	54.35	9.88	9022	2073	4496	354	0.0444	1.66E+06	5	30
cambrian sandstone	0.48	2701	0.253	10.41	4.73	166.06	107.87	16066	9496	6097	538	0.387	4.64E+06		
Pennsylvanian sandstone	1.44	2445	0.618	7.53	1.41	111.35	29.37	11236	5765	3834	341	0.067	3.58E+06		
Mississippian Sandstone	2.75	2417	1.871	9.84	6.56	91.03	34.67	9288	2679	4221	832	0.085	1.64E+06	20	110
Permian Sandstone	4.48	2372	1.824	6.67	1.73	51.61	19.28	6731	3258	4358	327	0.0338	6.11E+05	11	90
Miocene Sandstone	4.07	2417	8.258	3.59	0.7	62.02	3.33	6135	863	3168	28	0.13	9.46E+05	1	5
Volcaniclastic	3.24	2519	7.829	8.61	2.6	71.78	5	7065	1075	3565	243	0.394	4.56E+05	1	15
Dacite	3.12	2610	3.554	4.13	0.91	61.81	12.45	6961	410	3693	179.61	0.137	2.70E+06		

UTS= uniaxial tensile strength, UCS= uniaxial compressive strength

Table A.2: Uniaxial Strength Tests and P-Wave Speed of All Core Samples

Rock Type	Sample	UTS (Mpa)	UCS (Mpa)	Young's Modulus (Mpa)	P-wave Speed (m/s)	Time to Failure (s)	Thickness of the Core Sample (m)
Quartzite	QC1		121.99	11303	6130	103.70	0.089
Quartzite	QC2		127.77	7237	5974	74.07	0.046
Quartzite	QC3		215.71	13906	6533	81.08	0.049
Quartzite	QT1	3.98					
Quartzite	QT2	24.68					
Quartzite	QT3	7.90					
Quartzite	QT4	22.62					
Quartzite	QT5	16.25					
Quartzite	QT6	11.11					
Quartzite	QT7	16.67					
Quartzite	QT8	17.66					
Quartzite	QT9	15.10					
Quartzite	QT10	17.64					
Quartzite	QT11	14.02					
Quartzite	QT12	24.19					
Quartzite	QT13	7.75					
Quartzite	QT14	10.10					
Quartzite	QT15	12.89					
Quartzite	QT16	13.78					
Quartzite	QT17	17.73					
Granodiorite	GDC1		193.03	15036	6242	91.89	0.098
Granodiorite	GDC2		75.93	13000	6092	87.89	0.106
Granodiorite	GDC3		50.97	9525	5922	58.26	0.105
Granodiorite	GDT1	10.67					
Granodiorite	GDT2	13.77					
Granodiorite	GDT3	13.41					
Granodiorite	GDT4	17.45					
Granodiorite	GDT5	15.58					
Granodiorite	GDT6	15.78					
Granodiorite	GDT7	14.11					
Granodiorite	GDT8	13.67					
Granodiorite	GDT9	16.32					
Granodiorite	GDT10	25.52					
Granodiorite	GDT11	21.17					
Granodiorite	GDT12	25.69					
Granodiorite	GDT13	21.73					
Granodiorite	GDT14	18.68					
Granodiorite	GDT15	27.16					
Granodiorite	GDT16	21.32					

Granodiorite	GDT17	14.27					
Granodiorite	GDT18	25.98					
Granodiorite	GDT19	20.81					
Granodiorite	GDT20	26.05					
Granodiorite	GDT21	23.96					
Granite	GRC1		82.82	7546	2933	81.88	0.0792
Granite	GRC2		86.55	9903	3102	59.06	0.082
Granite	GRC3		48.03	6195	2822	54.65	0.085
Granite	GRC4		76.58	7102	4021	96.69	0.078
Granite	GRC5		76.72	6309	4021	83.68	0.074
Granite	GRC6		53.86	4615	2829	96.29	0.068
Granite	GRT1	4.90					
Granite	GRT2	5.52					
Granite	GRT3	4.22					
Granite	GRT4	4.67					
Granite	GRT5	3.33					
Granite	GRT6	3.41					
Granite	GRT7	5.84					
Granite	GRT8	2.59					
Granite	GRT9	5.89					
Granite	GRT10	5.46					
Granite	GRT11	6.93					
Granite	GRT12	6.67					
Granite	GRT13	5.62					
Granite	GRT14	4.93					
Granite	GRT15	4.83					
Granite	GRT16	5.00					
Granite	GRT17	7.26					
Granite	GRT18	4.73					
Granite	GRT19	9.15					
Granite	GRT20	6.68					
Granite	GRT21	7.29					
Granite	GRT22	5.59					
Granite	GRT23	4.84					
Marble	MC1		122.64	8961	6098	684.32	0.083
Marble	MC2		76.65	7982	5975	480.10	0.082
Marble	MC3		94.47	9901	5831	477.06	0.073
Marble	MT1	13.90					
Marble	MT2	16.76					
Marble	MT3	8.12					
Marble	MT4	11.18					
Marble	MT5	5.30					
Marble	MT6	19.61					
Marble	MT7	15.34					
Marble	MT8	7.34					

Marble	MT9	11.59					
Marble	MT10	20.11					
Marble	MT11	9.43					
Marble	MT12	14.46					
Marble	MT13	9.71					
Marble	MT14	12.68					
Greenstone	GSC1		74.19	12000	5605	89.29	0.088
Greenstone	GSC2		84.83	11977	5530	48.65	0.077
Greenstone	GSC3		78.76	9976	5753	87.89	0.084
Greenstone	GSC4		54.72	9444	5000	58.06	0.0997
Greenstone	GSC5		5.40	1413	4673	24.82	0.089
Greenstone	GSC6		25.09	3018	4760	66.26	0.0997
Greenstone	GSC7		37.40	6300	4346	57.66	0.0858
Greenstone	GSC8		103.94	10163	6154	101.70	0.0915
Greenstone	GSC9		125.96	14380	6037	97.50	0.091
Greenstone	GSC10		117.23	11994	6144	82.68	0.083
Greenstone	GST1	14.57					
Greenstone	GST2	12.35					
Greenstone	GST3	8.69					
Greenstone	GST4	17.59					
Greenstone	GST5	15.99					
Greenstone	GST6	10.53					
Greenstone	GST7	15.25					
Greenstone	GST8	14.20					
Greenstone	GST9	2.51					
Greenstone	GST10	10.07					
Greenstone	GST11	12.91					
Greenstone	GST12	8.91					
Greenstone	GST3	3.40					
Greenstone	GST14	8.10					
Greenstone	GST15	9.70					
Greenstone	GST16	4.92					
Rhyolite	RC1		45.94	661	4607	61.06	0.0945
Rhyolite	RC2		83.31	834	4673	63.26	0.094
Rhyolite	RC3		118.13	1454	4568	56.86	0.09
Rhyolite	RT1	8.85					
Rhyolite	RT2	14.53					
Rhyolite	RT3	10.64					
Rhyolite	RT4	4.85					
Phyllite	PHC		47.79	4700	5618	132.33	0.0555
Phyllite	PHC1		99.46	9092	5630	94.29	0.066
Phyllite	PHC2		129.80	9166	4679	81.48	0.066
Phyllite	PHC3		96.22	9108	4774	63.06	0.0665
Phyllite	PHC4		111.34	14000	4909	76.88	0.0532
Phyllite	PHC5		48.22	6157	4825	80.68	0.097

Phyllite	PHC6		48.29	5090	4707	86.08	0.0962
Phyllite	PHC7		26.53	2941	4974	66.06	0.0955
Phyllite	PHT1	16.42					
Phyllite	PHT2	15.55					
Phyllite	PHT3	11.20					
Phyllite	PHT4	17.45					
Phyllite	PHT5	14.53					
Phyllite	PHT6	8.96					
Phyllite	PHT7	18.21					
Phyllite	PHT8	11.51					
Phyllite	PHT9	13.36					
Phyllite	PHT10	11.50					
Phyllite	PHT11	14.93					
Phyllite	PHT12	13.69					
Phyllite	PHT3	13.38					
Phyllite	PHT4	12.76					
Phyllite	PHT5	12.28					
Phyllite	PHT16	17.68					
Basalt	BC1		133.56	17000	5000	108.71	0.0785
Basalt	BC2		115.25	16000	5625	116.11	0.09
Basalt	BC3		160.59	14060	5230	113.31	0.0912
Basalt	BC4		118.67	18447	5290	50.45	0.091
Basalt	BC5		168.77	19430	5306	74.67	0.103
Basalt	BC6		164.49	17602	5192	66.46	0.0973
Basalt	BC7		59.71	10943	5000	42.64	0.1025
Basalt	BC8		100.54	15997	4976	48.05	0.107
Basalt	BC9		89.53	13722	4679	244.12	0.094
Basalt	BC10		68.87	18000	5053	59.46	0.095
Basalt	BC11		127.68	15615	5112	59.66	0.102
Basalt	BC12		169.43	17086	5157	66.26	0.099
Basalt	BC13		80.77	6420	5000	97.50	0.063
Basalt	BC14		70.58	8480	5051	97.09	0.098
Basalt	BC15		96.33	12511	5025	82.48	0.1017
Basalt	BT1	10.05					
Basalt	BT2	16.43					
Basalt	BT3	18.52					
Basalt	BT4	16.61					
Basalt	BT5	10.15					
Basalt	BT6	8.99					
Basalt	BT7	6.36					
Basalt	BT8	15.39					
Basalt	BT9	11.56					
Basalt	BT10	15.71					
Basalt	BT11	14.81					
Basalt	BT12	12.74					

Basalt	BT13	13.76					
Basalt	BT14	10.32					
Basalt	BT15	12.02					
Basalt	BT16	9.18					
Basalt	BT17	13.04					
Basalt	BT18	17.43					
Basalt	BT19	16.63					
Basalt	BT20	19.73					
Basalt	BT21	9.79					
Basalt	BT22	10.31					
Basalt	BT23	9.77					
Basalt	BT24	13.27					
Basalt	BT25	14.12					
Basalt	BT26	9.08					
Vesicular Basalt	VBC1		64.74	10336	4761	46.45	0.09
Vesicular Basalt	VBC2		45.06	6632	4094	44.84	0.0948
Vesicular Basalt	VBC3		53.28	10098	4634	44.04	0.095
Vesicular Basalt	VBT1	7.96					
Vesicular Basalt	VBT2	6.13					
Vesicular Basalt	VBT3	4.36					
Vesicular Basalt	VBT4	4.22					
Vesicular Basalt	VBT5	5.88					
Vesicular Basalt	VBT6	5.50					
Vesicular Basalt	VBT7	4.37					
Vesicular Basalt	VBT8	5.31					
Vesicular Basalt	VBT9	4.39					
Cambrian Sandstone	CSC		331.03	26959	6605	132.33	0.107
Cambrian Sandstone	CSC1		318.44	27157	6442	115.11	0.1055
Cambrian Sandstone	CSC2		151.01	13462	6601	119.12	0.1015
Cambrian Sandstone	CSC3		65.39	6904	5412	124.29	0.0972
Cambrian Sandstone	CSC4		129.50	16714	5932	88.29	0.0923
Cambrian Sandstone	CSC5		32.53	5200	5556	83.68	0.092
Cambrian Sandstone	CST1	8.60					
Cambrian Sandstone	CST2	6.82					
Cambrian Sandstone	CST3	14.02					
Cambrian	CST4	8.98					

Sandstone							
Cambrian Sandstone	CST5	21.06					
Cambrian Sandstone	CST6	21.87					
Cambrian Sandstone	CST7	5.80					
Cambrian Sandstone	CST8	7.22					
Cambrian Sandstone	CST9	7.35					
Cambrian Sandstone	CST10	4.79					
Cambrian Sandstone	CST11	8.69					
Cambrian Sandstone	CST12	5.68					
Cambrian Sandstone	CST3	6.94					
Cambrian Sandstone	CST4	8.38					
Cambrian Sandstone	CST15	11.37					
Cambrian Sandstone	CST16	12.02					
Cambrian Sandstone	CST17	15.62					
Cambrian Sandstone	CST18	11.95					
Cambrian Sandstone	CST19	11.66					
Cambrian Sandstone	CST20	9.29					
Pennsylvanian sandstone	PNC1		63.21	5400	3809	108.51	0.055
Pennsylvanian sandstone	PNC2		97.56	8158	3333	108.91	0.0882
Pennsylvanian sandstone	PNC3		89.83	7699	3205	104.90	0.0826
Pennsylvanian sandstone	PNC4		88.71	6205	3823	101.50	0.0666
Pennsylvanian sandstone	PNC5		122.80	9916	4005	107.30	0.077
Pennsylvanian sandstone	PNC6		131.33	9271	4076	105.10	0.0644
Pennsylvanian	PNC7		145.81	15575	4099	113.11	0.106

sandstone							
Pennsylvanian sandstone	PNC8		139.04	15899	4108	86.08	0.101
Pennsylvanian sandstone	PNC9		129.78	23000	4051	90.69	0.0998
Pennsylvanian sandstone	PNT1	6.76					
Pennsylvanian sandstone	PNT2	7.34					
Pennsylvanian sandstone	PNT3	7.25					
Pennsylvanian sandstone	PNT4	9.57					
Pennsylvanian sandstone	PNT5	7.88					
Pennsylvanian sandstone	PNT6	7.55					
Pennsylvanian sandstone	PNT7	8.10					
Pennsylvanian sandstone	PNT8	8.56					
Pennsylvanian sandstone	PNT9	7.98					
Pennsylvanian sandstone	PNT10	5.78					
Pennsylvanian sandstone	PNT11	6.85					
Pennsylvanian sandstone	PNT12	4.52					
Pennsylvanian sandstone	PNT13	9.73					
Mississippian Sandstone	MSC1		97.55	11923	3667	64.06	0.099
Mississippian Sandstone	MSC2		93.10	9356	3302	75.87	0.0975
Mississippian Sandstone	MSC3		37.77	5800	3442	79.28	0.0852
Mississippian Sandstone	MSC4		100.80	8915	5062	84.88	0.082
Mississippian Sandstone	MSC5		73.72	7040	4925	77.68	0.065
Mississippian Sandstone	MSC6		143.32	12692	4929	76.67	0.07
Mississippian Sandstone	MST1	1.46					
Mississippian	MST2	4.31					

Sandstone							
Mississippian Sandstone	MST3	4.42					
Mississippian Sandstone	MST4	5.43					
Mississippian Sandstone	MST5	4.49					
Mississippian Sandstone	MST6	10.90					
Mississippian Sandstone	MST7	8.84					
Mississippian Sandstone	MST8	11.90					
Mississippian Sandstone	MST9	11.03					
Mississippian Sandstone	MST10	9.77					
Mississippian Sandstone	MST11	15.12					
Mississippian Sandstone	MST12	10.03					
Mississippian Sandstone	MST13	6.66					
Mississippian Sandstone	MST14	1.99					
Mississippian Sandstone	MST15	2.63					
Mississippian Sandstone	MST16	2.00					
Mississippian Sandstone	MST17	2.31					
Mississippian Sandstone	MST18	3.00					
Mississippian Sandstone	MST19	2.19					
Mississippian Sandstone	MST20	1.99					
Mississippian Sandstone	MST21	2.42					
Mississippian Sandstone	MST22	2.07					
Mississippian Sandstone	MST23	2.40					
Mississippian Sandstone	MST24	2.16					
Mississippian	MST25	2.38					

Sandstone							
Mississippian Sandstone	MST26	19.73					
Mississippian Sandstone	MST27	16.74					
Mississippian Sandstone	MST28	9.62					
Mississippian Sandstone	MST29	15.20					
Mississippian Sandstone	MST30	16.21					
Mississippian Sandstone	MST31	19.91					
Mississippian Sandstone	MST32	16.39					
Mississippian Sandstone	MST33	17.74					
Mississippian Sandstone	MST34	17.20					
Mississippian Sandstone	MST35	19.41					
Mississippian Sandstone	MST36	15.94					
Mississippian Sandstone	MST37	17.29					
Mississippian Sandstone	MST38	16.55					
Mississippian Sandstone	MST39	15.84					
Mississippian Sandstone	MST40	15.31					
Mississippian Sandstone	MST41	17.64					
Mississippian Sandstone	MST42	14.77					
Permian Sandstone	PMC1		46.11	7900	4500	97.90	0.1035
Permian Sandstone	PMC2		42.34	5232	4010	62.46	0.076
Permian Sandstone	PMC3		32.96	4400	3926	70.07	0.064
Permian Sandstone	PMC4		75.69	6975	4634	94.09	0.095
Permian Sandstone	PMC5		67.42	13000	4714	88.69	0.0993
Permian	PMC6		84.94	10150	4632	78.08	0.0948

Sandstone							
Permian Sandstone	PMC7		33.47	2178	4008	81.88	0.094
Permian Sandstone	PMC8		38.82	4931	4153	63.26	0.092
Permian Sandstone	PMC9		42.78	5808	4649	57.66	0.086
Permian Sandstone	PMT1	6.41					
Permian Sandstone	PMT2	7.56					
Permian Sandstone	PMT3	4.41					
Permian Sandstone	PMT4	5.83					
Permian Sandstone	PMT5	4.33					
Permian Sandstone	PMT6	4.71					
Permian Sandstone	PMT7	9.45					
Permian Sandstone	PMT8	9.36					
Permian Sandstone	PMT9	6.10					
Permian Sandstone	PMT10	7.52					
Permian Sandstone	PMT11	9.53					
Permian Sandstone	PMT12	5.30					
Permian Sandstone	PMT13	3.86					
Permian Sandstone	PMT14	9.66					
Permian Sandstone	PMT15	6.68					
Permian Sandstone	PMT16	7.59					
Permian Sandstone	PMT17	6.62					
Permian Sandstone	PMT18	4.60					
Permian Sandstone	PMT19	7.26					
Permian	PMT20	6.30					

Sandstone							
Permian Sandstone	PMT21	7.18					
Permian Sandstone	PMT22	5.99					
Permian Sandstone	PMT23	7.21					
Miocene Sandstone	MCC1		64.13	6551	3140	96.09	0.0925
Miocene Sandstone	MCC2		58.19	5142	3195	92.69	0.0778
Miocene Sandstone	MCC3		63.77	6710	3170	80.48	0.089
Miocene Sandstone	MCT1	3.21					
Miocene Sandstone	MCT2	3.66					
Miocene Sandstone	MCT3	3.52					
Miocene Sandstone	MCT4	3.45					
Miocene Sandstone	MCT5	2.87					
Miocene Sandstone	MCT6	3.73					
Miocene Sandstone	MCT7	2.82					
Miocene Sandstone	MCT8	4.51					
Miocene Sandstone	MCT9	4.66					
Miocene Sandstone	MCT10	3.25					
Miocene Sandstone	MCT11	3.10					
Miocene Sandstone	MCT12	4.53					
Miocene Sandstone	MCT13	3.05					
Miocene Sandstone	MCT14	4.59					
Miocene Sandstone	MCT15	3.12					
Miocene Sandstone	MCT16	3.79					
Miocene	MCT17	2.37					

Sandstone							
Miocene Sandstone	MCT18	4.46					
Volcaniclastic	VCC1		73.61	8468	3490	434.64	0.075
Volcaniclastic	VCC2		74.24	6590	3812	563.26	0.078
Volcaniclastic	VCC3		77.83	7880	3678	493.87	0.083
Volcaniclastic	VCC4		64.38	5466	3636	588.91	0.067
Volcaniclastic	VCC5		75.28	7943	3808	473.86	0.082
Volcaniclastic	VCC6		65.69	6215	3385	528.54	0.078
Volcaniclastic	VCC7		71.40	6890	3144	518.11	0.08
Volcaniclastic	VCT1	4.67					
Volcaniclastic	VCT2	5.23					
Volcaniclastic	VCT3	12.29					
Volcaniclastic	VCT4	11.35					
Volcaniclastic	VCT5	7.97					
Volcaniclastic	VCT6	9.81					
Volcaniclastic	VCT7	11.22					
Volcaniclastic	VCT8	3.54					
Volcaniclastic	VCT9	10.23					
Volcaniclastic	VCT10	6.94					
Volcaniclastic	VCT11	8.63					
Volcaniclastic	VCT12	6.76					
Volcaniclastic	VCT13	9.32					
Volcaniclastic	VCT14	6.73					
Volcaniclastic	VCT15	10.43					
Volcaniclastic	VCT16	5.11					
Volcaniclastic	VCT17	11.03					
Volcaniclastic	VCT18	9.26					
Volcaniclastic	VCT19	10.05					
Volcaniclastic	VCT20	11.71					
Dacite	DCC1		74.96	7395	3883	506.88	0.69
Dacite	DCC2		50.21	6579	3670	381.60	0.072
Dacite	DCC3		60.24	6911	3526	435.85	0.074
Dacite	DCT1	5.98					
Dacite	DCT2	3.39					
Dacite	DCT3	4.32					
Dacite	DCT4	4.88					
Dacite	DCT5	5.65					
Dacite	DCT6	3.25					
Dacite	DCT7	4.25					
Dacite	DCT8	4.76					
Dacite	DCT9	3.87					
Dacite	DCT10	4.62					
Dacite	DCT11	3.53					
Dacite	DCT12	3.91					

Dacite	DCT13	3.80					
Dacite	DCT14	2.78					
Dacite	DCT15	3.88					
Dacite	DCT16	4.98					
Dacite	DCT17	2.56					
Dacite	DCT18	3.92					
Rock Type	Sample	UTS (Mpa)	UCS (Mpa)	Young's Modulus (Mpa)	P-wave Speed (m/s)	Time to Failure (s)	Thickness of the Core Sample (m)